Advancements in Silver-Based Electrically Conductive Polymer Composites: Properties, Applications, and Performance

Zur Erlangung des akademischen Grades eines

DOKTORS DER INGENIEURWISSENSCHAFTEN

von der KIT-Fakultät für Chemieingenieurwesen und Verfahrenstechnik des Karlsruher Instituts für Technologie (KIT) genehmigte

DISSERTATION

von

(M.Sc.) Jonas Marten
aus Karlsruhe

Tag der mündlichen Prüfung: 17.12.2025

Erstgutachter: Prof. Dr. Norbert Willenbacher

Zweitgutachter: Prof. Dr. Patrick Théato

Preface

This publication-based dissertation consists of three peer-reviewed scientific journal articles. They include the main results of my experimental work at the Karlsruhe Institute of Technology (KIT), Institute of Mechanical Process Engineering and Mechanics in the group of Applied Mechanics during June 2021 until March 2025.

This thesis follows a brief introduction to the state of the art on electrically conductive polymer composites with applications in photovoltaics and smart electronic devices. The main part of this dissertation consists of the following publications:

• Iodine-Induced Microphase Separation Controls Flow Behavior and Electrical Conductivity of Silver-filled Polymer Composites

• High-throughput Production of Electrically Conductive Yarn (E-Yarn) for Smart Textiles

• Highly Conductive Coated Wires for Interconnection of Solar Cells with TECC-Wire Technology

The dissertation concludes with a brief summary, an outlook as well as a bibliography. The bibliography includes all references of the publications. Hereby, the publications are slightly changed. Some graphs and images are modified in size and color.

Acknowledgments

First and foremost, I want to thank my parents, Ulli and Christiane, for their constant support throughout my life. Your steady support and trust allowed me to explore, question, and keep moving forward through every stage of this work.

A big thank you to Linda, who was always there for me - especially during the final, intense months at the institute. Your support during that time meant a lot.

To all my university friends from the past ten years: thank you for being part of this journey. We studied together - and, sometimes, very intentionally didn't - and I truly wouldn't have made it through all the exams and theses without you.

I'm also grateful to my coworkers, especially Katarzyna, Felipe, Tillman, and Fabian, with whom I shared an office. Our many conversations about theories, experiments, and papers were incredibly helpful. And just having someone to talk to when nothing seemed to work made a big difference.

At the beginning of my PhD, Yiliang was a huge support. You helped me find direction when I needed it, and I really appreciated our honest and thoughtful conversations. Thank you.

A heartfelt thank you goes to Bernhard, who always had time for my technical questions - especially when it came to rheometry and rheology. Your advice helped me a lot. I also want to thank Karsten for his ongoing support with technical issues over the years.

Thank you, Felix, for always making excellent coffee - especially when I needed it most (which was often!).

I'd also like to thank all the students I had the chance to supervise over the years. Your work was an important part of making the experiments happen, and I appreciated your help and input.

Last but definitely not least, I want to sincerely thank Prof. Norbert Willenbacher for your support and mentorship over the past three and a half years. Thank you for taking the time to discuss results, theories, and next steps. I'm grateful for the freedom you gave me to shape my research independently - while still always being there when I needed help or guidance.

Abstract

The 21st century has thus far presented numerous challenges, including climate change, resource depletion, and transformative societal shifts driven by emerging technologies such as AI-based systems and smart electronic devices. These developments are accelerating progress across various industries, particularly in photovoltaics and electronics.

The increasing demand for affordable energy is fueling the global expansion of photovoltaic systems, bringing the limited availability of key resources such as silver, indium, and bismuth into focus. Currently, about 14 % of global silver production is used for manufacturing photovoltaic modules, with forecasts predicting a significant rise in production by 2040. At the same time, new solar cell technologies are being developed to achieve higher energy yields, but also impose greater demands on system components. Furthermore, the integration of smart technologies into everyday life is advancing rapidly. Smartphones, smartwatches, and fitness trackers are just the beginning of a new era of electrical devices. Electrically conductive materials are increasingly being used in textiles and clothing, enabling the seamless integration of sensors and actuators.

To meet the demands of rapid technological advancement, these innovations require materials that possess exceptional mechanical, chemical, and electrical properties while remaining cost-efficient and resource-effective. Given the diverse and stringent requirements across market segments, electrically conductive polymer composites are being developed for applications in both fields, ensuring they keep pace with evolving industry needs. In photovoltaics, they serve as electrically conductive adhesives for interconnecting temperature-sensitive solar cells, while in electronics, they are used for conductive coatings and the production of flexible sensors in smart clothing. Thanks to their versatile and precisely adjustable chemical and physical properties, these polymer-based formulations are widely used and continuously developed for numerous applications in these market sectors.

This study examines the use of iodine-induced microphase separation to enhance the electrical conductivity of silver-particle-filled polymer formulations while simultaneously reducing silver consumption, addressing the critical issue of resource conservation. Three iodine salts - 1-butyl-3-methylimidazolium iodide, potassium iodide, and sodium iodide - were directly mixed into thermoplastic polyurethane solutions containing varying concentrations of micron-sized silver particles. The resulting paste-like suspension suggested the formation of a percolating particle network in the wet state. In dry films, electrical conductivity improved significantly, from 10^{-5} S/cm without iodine to 500 S/cm at 12 vol% silver and 2,600 S/cm at 20 vol% silver, regardless of the iodine type. Thermogravimetric analysis and infrared spectroscopy confirmed that iodine removes surface lubricants from silver particles, enhancing particle interactions. Scanning electron microscopy further revealed iodine-induced microstructural heterogeneities on a 10 µm scale, forming conductive pathways that dramatically improve conductivity. These findings highlight the potential of iodine-modified silver-filled polymer solutions as a straightforward, cost-effective approach for high-performance conductive materials.

Furthermore, this dissertation presents a novel method for manufacturing electrically conductive Nylon yarn coated with a thermoplastic polymer layer, utilizing the previously described iodine-based formulation strategy. This yarn serves as a fundamental building block for integrating flexible wiring and smart functionalities into textiles. Leveraging the traditional wire coating process, this method is inherently scalable and efficient. To demonstrate feasibility, a laboratory-scale coating device was first developed and built, capable of continuously coating nylon yarn at a maximum speed of 2.8 m/min. Using this device, a nylon yarn was coated with layer (20 µm) consisting of a thermoplastic polyamide matrix containing 20 vol% silver flakes. The coated yarn exhibited a resistivity of approximately

7.5 Ω/cm, which remained stable even after multiple bending and washing cycles, simulating real-world textile usage. Furthermore, the yarn was used to fabricate a pressure sensor, demonstrating a sensitivity range of 1 - 20 kPa, a sensitivity of 10^{-3} kPa^{-1}, and a response time of 224 ms. These results confirm the potential of this versatile manufacturing process for smart textile applications, leveraging existing industrial-scale coating equipment to enable rapid market integration.

Moreover, this dissertation presents an in-depth investigation of TECC-Wire (Thermoplastic and Electrically Conductive Coated Wire), a promising interconnection technology for temperature-sensitive solar cells. TECC-Wire consists of round copper wires coated with a thermoplastic polymer layer filled with electrically conductive particles. This study introduces a novel wire coating formulation based on a polyamide-type wire enamel (Voltatex® 8609 ECO) filled with 12 vol% silver, achieving a conductivity of 480 S/cm. To assess performance, the rheological properties, along with the polymer and particle content of the formulation, were first optimized for the wire coating process, aiming to achieve a smooth, high-quality coating free of defects on a laboratory scale at relatively low process speeds of up to 6.9 m/min. Subsequently, initial trials were conducted using the wire enamel on industrial-scale wire-coating machines at speeds of up to 60 m/min. Afterwards, single half-cut M6 heterojunction (SHJ) solar cells were interconnected using these wires in a laboratory-scale stringing machine. Peel tests confirmed strong adhesion, with a peel force exceeding 1.5 N/mm. Electroluminescence (EL) imaging and current-voltage (IV) measurements demonstrated module efficiency, while damp heat (DH) tests evaluated long-term stability. The TECC-Wire achieved a fill factor (FF) of 81.25 ± 0.12 %, comparable to standard soldering techniques. Additionally, IEC-standard DH tests revealed a power loss of less than 5 % after 1,000 hours at +85 °C and 85 % relative humidity. These promising results support further development of TECC-Wire as a low-temperature, solder-free, cost-effective, and robust interconnection technology for high-throughput solar module production.

Zusammenfassung

Die Herausforderungen des 21. Jahrhunderts, darunter der Klimawandel, Ressourcenverknappung und gesellschaftlicher Wandel durch das Aufkommen neuer Technologien wie auf künstlicher Intelligenz basierter Systeme und intelligente elektronische Geräte, treiben die technische Entwicklung in verschiedenen Marktbranchen enorm voran, insbesondere in der Photovoltaik und Elektronik.

Die verstärkte Nachfrage nach kostengünstiger Energie fördert den globalen Ausbau von Photovoltaikanlagen, wodurch die begrenzte Verfügbarkeit bestimmter Ressourcen wie Silber, Indium und Bismut zunehmend in den Fokus rückt. Derzeit entfallen etwa 14 % der globalen Silberproduktion auf die Herstellung von Photovoltaikmodulen, und Prognosen gehen von einem starken Produktionsanstieg bis 2040 aus. Gleichzeitig werden neue Solarzellentechnologien entwickelt, die eine höhere Energieausbeute ermöglichen, jedoch auch höhere Anforderungen an die Systemkomponenten stellen. Zudem schreitet die Integration intelligenter Technologien in den Alltag rasant voran. Smartphones, Smartwatches und Fitnessarmbänder sind erst der Anfang. Elektrisch leitfähige Materialien finden zunehmend Einsatz in Textilien und Kleidung, wodurch Sensoren und Aktoren nahtlos integriert werden können. Diese Innovationen erfordern Werkstoffe mit herausragenden mechanischen, chemischen und elektrischen Eigenschaften, die gleichzeitig kosteneffizient und ressourcenschonend sein müssen.

Aufgrund der vielseitigen und anspruchsvollen Anforderungen in beiden Marktsegmenten finden elektrisch leitfähige Polymerformulierungen unterschiedliche Anwendungen: In der Photovoltaik werden sie als elektrisch leitfähige Klebstoffe zum Verschalten von Solarzellen angewendet, während sie in der Elektronik als leitfähige Beschichtungen und für die Herstellung flexibler Sensoren in intelligenten Kleidungsstücken Verwendung finden. Aufgrund ihrer vielseitigen sowie gezielt anpassbaren chemischen und physikalischen Eigenschaften werden diese polymerbasierten Formulierungen in zahlreichen zukunftsweisenden Anwendungen in diesen Marktsegmenten breit eingesetzt und weiterentwickelt.

In der vorliegenden Arbeit wird der Einsatz von jodinduzierter Mikrophasenseparation zur Steigerung der elektrischen Leitfähigkeit in mit Silberpartikeln gefüllter Polymerformulierungen bei gleichzeitiger Reduktion des Silberverbrauchs untersucht, um bei dem wegweisenden Punkt des Ressourcensparens anzusetzen. Zu diesem Zweck wurden drei Jodsalze – 1-Butyl-3-methylimidazoliumiodid, Kaliumiodid und Natriumiodid – zusammen mit Silbermikropartikeln in einer thermoplastischen Polyurethanlösung mit unterschiedlichen Konzentrationen dispergiert. Die resultierenden pastenartigen Suspensionen wiesen auf die Bildung eines perkolierenden Partikelnetzwerks im nassen Zustand hin. In trockenen Filmen wurde eine signifikante Steigerung der elektrischen Leitfähigkeit beobachtet: von 10^{-5} S/cm ohne Jod auf 500 S/cm bei 12 Vol.-% Silber und 2600 S/cm bei 20 Vol.-% Silber, unabhängig vom verwendeten Jodsalz. Die Ergebnisse thermogravimetrischer Analysen und Infrarotspektroskopie bestätigten, dass Jod die Fettsäuren von der Oberfläche der Silberpartikel entfernt und so die Partikelwechselwirkungen verändert. Zudem wurde mittels Rasterelektronenmikroskopie entdeckt, dass durch die Zugabe von verschiedenen Jodsalzen die Partikelmikrostruktur verändert wird. Die zunehmende Heterogenität, die sich in der Bildung von Agglomeraten im Langenbereich von 10 µm äußert, führt zu einer erhöhten Anzahl an elektrisch leitfähigen Pfaden durch die Polymermatrix. Dies ist wahrscheinlich der Grund für die starke Erhöhung der elektrischen Leitfähigkeit. Diese Ergebnisse betonen das Potenzial von jodmodifizierten, silbergefüllten Polymerlösungen als eine unkomplizierte und kosteneffektive Methode zur Herstellung leistungsfähiger, leitfähiger und ressourcenschonender Materialien.

Darüber hinaus wird eine neuartige Methode zur Herstellung elektrisch leitfähig beschichteten Nylongarns präsentiert. Das Garn kann anschließend als Grundbaustein zur Integration flexibler Verdrahtung und intelligenter Funktionen in Textilien dienen. Das hier angewendete Verfahren basiert auf dem klassischen Drahtbeschichtungsprozess und ist daher skalierbar. Im Rahmen einer Machbarkeitsstudie wurde zunächst eine Beschichtungsanlage im Labormaßstab entwickelt, die eine reproduzierbare Garnbeschichtung bei einer Geschwindigkeit von etwa 2,8 m/min ermöglicht. Mit diesem Gerät wurde ein Nylongarn mit einer 20 µm dicken thermoplastischen Beschichtung, bestehend aus einer Polyamidmatrix, die 20 Vol.-% Silberpartikeln enthält hergestellt. Die elektrische Leitfähigkeit wurde durch die Zugabe einer Jodkomponente, gemäß dem zuvor beschriebenen Phänomen der Mikrophasenseparation, verbessert. Das beschichtete Garn wies einen spezifischen elektrischen Widerstand von ca. 7,5 Ω/cm auf, der selbst nach mehrfacher Biegung und Reinigung stabil bleibt, wodurch reale Anwendungsbedingungen simuliert wurden. Zudem wurde das beschichtete Garn in einen Drucksensor integriert, der einen Messbereich von 1 – 20 kPa, eine Empfindlichkeit von 10^{-3} kPa^{-1} und eine Reaktionszeit von 224 ms aufwies. Diese Ergebnisse bestätigen das Potenzial dieses Herstellungsprozesses für intelligente Textilanwendungen. Da außerdem potenziell industrielle Beschichtungstechnologien genutzt werden können, wäre eine relativ schnelle Markteinführung möglich.

Zudem wird in dieser Dissertation eine umfassende Untersuchung von TECC-Wire (Thermoplastic and Electrically Conductive Coated Wire), einer vielversprechenden Verbindungstechnologie für temperatursensitive Solarzellen präsentiert. TECC-Wire sind runde Kupferdrähte, die mit einer elektrisch leitfähigen thermoplastischen Polymerschicht ummantelt sind. Im Rahmen dieser Studie wird eine solche Drahtbeschichtung mit hoher elektrischer Leitfähigkeit entwickelt. Basierend auf einem Polyamid-Drahtlack (Voltatex® 8609 ECO) gefüllt mit 12 Vol-% Silber, inklusive der Jodkomponente 1-Butyl-3-methylimidazoliumiodid wurde eine elektrische Leitfähigkeit von 480 S/cm erreicht. Zunächst wurden die rheologischen Eigenschaften sowie der Polymer- und Partikelgehalt der Formulierung für den Drahtbeschichtungsprozess optimiert, mit dem Ziel, eine glatte, hochwertige Beschichtung ohne Defekte im Labormaßstab bei vergleichsweise niedrigen Prozessgeschwindigkeiten von bis zu 6,9 m/min zu erreichen. Anschließend wurden erste Versuche auf industriellen Drahtbeschichtungsanlagen bei Geschwindigkeiten von bis zu 60 m/min durchgeführt. Zur Leistungsbewertung wurden einzelne halbierte M6-Heterojunction-(SHJ)-Solarzellen mit diesen Drähten in einer Laborstringer verschaltet. Schältests zeigten eine hohe Haftfestigkeit der ummantelten Drähte auf den Solarzellen mit einer Schälkraft von über 1,5 N/mm. Elektrolumineszenz-(EL)-Bilder und Strom-Spannungs-(IV)-Messungen bestätigten eine, mit herkömmlichen Lötverfahren vergleichbaren, Moduleffizienz, während mit Hilfe von Feuchte-Wärme (DH)-Tests die Langzeitstabilität untersucht wurde. Die kontaktierten Zellen erreichten einen Füllfaktor (FF) von 81,25 ± 0,12. Zudem ergaben DH-Tests nach IEC-Standard einen Leistungsverlust von weniger als 5 % nach 1.000 Stunden bei +85 °C und 85 % relativer Luftfeuchtigkeit. Diese vielversprechenden Ergebnisse beflügeln die Weiterentwicklung von TECC-Wire als eine lötfreie, kostengünstige und robuste Verbindungstechnologie für die Hochgeschwindigkeitsproduktion von Solarmodulen.

Notation

Abbreviation

Ag	Silver
AgI	Silver iodide
AI	Artificial intelligence
Au	Gold
Bi	Bismuth
CB	Carbon black
CNT	Carbon nano tubes
Cu	Copper
DH	Damp heat
DMSO	Dimethyl sulfoxide
ECA	Electrically conductive adhesive
EDX	Energy-dispersive X-ray spectroscopy
EL	Electroluminescence
F	Front side
I_2	Iodine
IEC	International electrotechnical commission
IL	1-butyl-3-methylimidazolium iodide
In	Indium
IoT	Internet of Things
IR	Infrared
ITO	Indium tin oxide
IV	Current-voltage
KBr	Potassium bromide
KI	Potassium iodide
mpp	maximum power point
NaI	Sodium iodide
Ni	Nickel
NP	Nano-particle
NW	Nano-wire
OC	Open circuit voltage
PA	Polyamide
PAN	Polyacrylonitrile
PC	Polycarbonate
PCE	Power conversion efficiency

PDMS	Polydimethylsiloxan
PERC	Passivated emitter and rear cell
PET	Polyethylenterephtalat
PV	Photovoltaic
R	Rear side
SC	Short circuit current
SEM	Scanning electron microscopy
SHJ	Silicon heterojunction cell
Si	Silicon
SnPb	Tin-Lead
TC	Thermal cycling
TCO	Transparent conductive oxide
TECC-wire	Thermoplastic and electrically conductive coated wire
TGA	Thermal Gravimetric Analysis
TopCon	The tunnel oxide passivated contact
TPTA	Terephthalaldehyde
TPU	Thermoplastic polyurethane
XPS	X-ray photoelectron spectroscopy

Latin symbols

A	Facing area of the two electrodes	[m^2]
c	Speed of light	[m/s]
C	Capacitance	[F]
C_0	Capacitance in the beginning	[F]
d_{nozzle}	Coating nozzle diameter	[µm]
d_{probes}	Distance of the voltage probes	[cm]
d_{wire}	Copper wire diameter	[µm]
E	Absorbed energy	[J]
FF	Fill factor	[-]
h	Planck's constant	[J/S]
I_{mmp}	Current at mmp	[A]
I_{SC}	Short circuit Current	[A]
n_{iodide}	Amount of iodide	[mmol]
P_{mpp}	Maximum Power output	[W_p]
Q_3	Cumulative percent volume	[%]
R	Electrical resistance	[Ω]
$t_{coating}$	Thickness of the coating	[cm]

V_{Ag}	Silver volume	[cm^3]
V_{mpp}	Voltage at mpp	[V]
V_{OC}	Open Circuit voltage	[V]
w	Yarn coating thickness	[µm]
$w_{coating}$	Width of the coating	[cm]

Greek symbols

δ	Distance of two electrodes of a Capacitor	[m]
ε_0	Permittivity of the medium	[F/M]
ε_r	Relative permittivity	[-]
η	Dynamic viscosity	[Pa·s]
κ	Electrical conductivity	[S/cm]
λ	Wavelength of the light	[m]
σ_y	Yield stress	[Pa]
φ	Volume fraction	[-]
σ	Shear stress	[Pa]

Table of Contents

Chapter 1 General introduction

The 21st century is characterized by a multitude of challenges, including climate change, diminishing resources, and profound societal shifts driven by emerging technologies such as AI-based systems and smart electronic devices. The opportunities and challenges that arise from these developments have accelerated advancements across several key industries, notably the photovoltaic and electronics sectors.

The demand for affordable energy is driving the rapid expansion of photovoltaic installations, which in turn is highlighting the limits of our finite resources. For example, the current annual production of photovoltaic modules consumes approximately 14 % of the world's silver supply - a proportion that is set to increase as demand grows. In addition, the push for more efficient photovoltaic technologies is raising performance standards and increasing the demands on the components used in these systems. As electrically conductive adhesives for interconnecting temperature-sensitive solar cell designs, these materials must meet the photovoltaic industry's stringent requirements for adhesion, flexibility, electrical conductivity, and long-term stability, while also being cost-effective and minimally resource-intensive for high-volume production.

At the same time, the invention of devices such as smartphones has radically changed everyday life. In just a few decades, society has moved from an analog to a digital era, with individuals constantly connected through a global network. This remarkable progress has spurred the development of innovative smart applications and a deeper integration of advanced electronic devices into our daily lives. Consequently, the materials utilized for these applications are becoming increasingly sophisticated, necessitating a combination of flexibility, durability, stretchability, low toxicity, sensitivity to various stimuli, and chemical stability, while concurrently maintaining reliable electrical conductivity. Moreover, when these materials are integrated directly into textiles, they must be compatible with large-scale manufacturing processes.

Therefore, electrically conductive polymer composites are expected to exhibit a wide range of properties, addressing the multifaceted challenges of the modern era. As a result, these materials have become key drivers of innovation in the fields of photovoltaics and electronics. This thesis explores microstructural phenomena to minimize the consumption of valuable silver while simultaneously proposing applications based on these findings in both the electronics and photovoltaic sectors.

First, a theoretical background on electrically conductive adhesives is presented, detailing the typical properties of various polymer types. Additionally, the manufacturing process of electrically conductive polymers and their common applications are explored. The text further discusses how these materials are used in the production of different types of smart, flexible sensors. Moreover, an introduction to photovoltaic (PV) modules is provided, covering the photovoltaic effect - the fundamental physical principle behind PV modules - along with the interconnection processes that transform individual solar cells into a functional PV module. In this context, electrically conductive adhesives are examined as a method for interconnecting solar cells, including an explanation of the TECC-Wire interconnection technique.

Afterwards, the key results of this dissertation are presented which are based on three publications. First, iodine-induced microphase separation was explored as a strategy to enhance the electrical conductivity of silver-particle-filled polymer formulations while simultaneously reducing silver consumption, addressing the critical challenge of resource conservation. Three iodine salts -1-butyl-3-methylimidazolium iodide, potassium iodide, and sodium iodide - were directly mixed into

thermoplastic polyurethane solutions containing varying concentrations of micron-sized silver particles. The formulations were analyzed by comparing their viscosity and yield stress. Additionally, the direct influence of the iodine compounds on the silver particles was examined using thermogravimetric analysis and infrared spectroscopy. Finally, solvent-free, silver-filled polymer composites were investigated in terms of electrical conductivity and microstructure using scanning electron microscopy.

Furthermore, a novel manufacturing method for electrically conductive coated Nylon yarn is introduced, serving as a fundamental building block for integrating electrical wiring and smart capabilities into textiles. First, a laboratory-scale coating machine was developed, inspired by the commercial wire coating processes. Next, a thermoplastic coating material was formulated, incorporating silver particles and the iodide compound 1-butyl-3-methylimidazolium iodide. By varying the silver content and iodine concentration, the electrical conductivity was fine-tuned, while adjustments to viscosity and solid content, along with coating trials, helped identify optimal parameters for achieving a high-quality coating. Additionally, bending and washing tests were conducted to simulate real-world textile applications. Finally, as a proof of concept, the coated yarn was used to fabricate a simple pressure sensor in collaboration with a research team from the School of Mechatronic Engineering and Automation in Shanghai, led by Guangjie Yuan.

In addition, this thesis presents an in-depth investigation of TECC-Wire (Thermoplastic and Electrically Conductive Coated Wire), a promising interconnection technology for temperature sensitive solar cells. TECC wire consists of round copper wires coated with a thermoplastic polymer layer embedded with electrically conductive particles. A technology developed and patented by Solyco GmbH, based in Berlin. This study presents a novel wire coating formulation based on a polyamide-type wire enamel (Voltatex® 8609 ECO) filled with silver particles. First, the electrical conductivity of the solvent-free polymer coating was optimized to achieve high conductivity while minimizing the use of silver. This was achieved by incorporating different concentrations of the ionic liquid 1-butyl-3-methylimidazolium iodide. Next, the viscosity of the solvent-containing formulation was adjusted to meet the requirements of the wire coating process to ensure a high-quality coating. Finally, interconnection experiments were performed on single half-cut M6 heterojunction solar cells, evaluating the interconnection quality by peel tests, electroluminescence imaging, current-voltage measurements and damp-heat tests.

Chapter 2 State of the art

2.1 Electrically conductive polymer composites

2.1.1 Introduction

Whether used as a solder replacement, for electrically conductive wiring, die attachment, or in the manufacturing of flexible electronics and smart devices, electrically conductive polymer composites are gaining attention due to their versatility [1–5]. By tailoring properties such as melting temperature, wettability, and mechanical strength over a broad range, these composites are opening up new opportunities in diverse and challenging fields - from the production of photovoltaic modules to the integration of smart functionalities into clothing and everyday devices [5–7]. This section provides a brief introduction to the base materials and physical principles that describe electrically conductive polymer composites. Section 2.1.2 offers an overview of the various types of polymers and microstructures, including those employed in this dissertation. Section 2.1.3 discusses the mechanism by which incorporating electrically conductive particles into a polymer matrix results in a conductive composite, and section 2.1.4 introduces the different types of filler materials used for incorporating electrical conductivity into these composites.

2.1.2 Polymers

Polymers are large molecules composed of numerous repeating units, called monomers, that are interconnected by covalent bonds [8]. The properties of a polymer are influenced not only by the chemical nature of the monomers but also by the architecture, which is established during the polymerization process [8]. Polymers can adopt various architectures, including linear macromolecules, comb-like structures, or randomly branched arrangements, as illustrated in Figure 1.

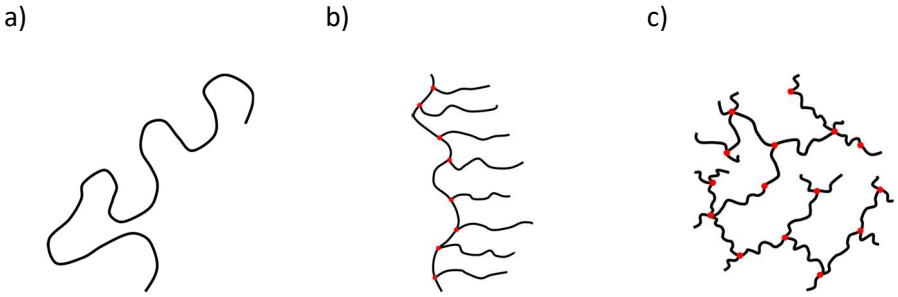

Figure 1 Polymer chain architectures: a) Linear, b) Comb, and c) Randomly branched [9].

When a large number of polymer chains are arranged in a three-dimensional matrix, different structural configurations arise depending on the chemical composition of the monomers. For instance, linear, amorphous, or partially crystalline structures can form, where chains are randomly entangled and held together by physical forces as can be seen in Figure 2 a) and b). These thermoplastic polymers possess the ability to transition repeatedly between solid and liquid states through heating and cooling, a critical property that is crucial for numerous applications [9]. Polyamide (PA), Polycarbonate (PC), or thermoplastic Polyurethane (TPU) belong to this group of polymers and are for example widely used in processes like injection molding. In such processes, the polymer is heated to re-plasticize it. Subsequently, the molten polymer is injected under high pressure into a mold, where it is cooled and solidifies into the desired shape [9–12]. Furthermore, these materials can also be used as an hot-melt adhesive. Applied as a polymer melt to substrates, they solidify upon cooling and form a mechanically stable bond. Typical applications include electronics, automotive, aerospace and coating applications

[13–15]. Another type of polymers are physical cross-linked elastomers (Figure 2c) which consist of a soft amorphous segment connected via rigid crystalline block. TPU is a widely used example for this class of polymers. These materials can also be processed via injection molding and are commonly used as hot-melt adhesives [16, 17].

Another type of polymer structure forms when monomers and polymer chains chemically react with each other to create a highly elastic, irreversible network of covalently bonded chains. Such reactions are triggered by functional groups, such as the oxirane ring in epoxy reactions or free radical and anionic chain polymerizations in acrylic-based polymers [18]. The reaction kinetics are influenced by temperature, pressure, and the concentration of functional groups. These factors also play a crucial role in determining the cross-linking density, which directly impacts the strength and toughness of the polymer network [18].

Figure 2 shows the differences between a polymer matrix with d) a low cross-linking density and e) a high cross-linking density. In contrast to thermoplastic polymers, these polymers are irreversibly bonded. That means, once the monomers and polymers have reacted, the polymer cannot be re-liquefied. Polymers of this type are extensively used as adhesives in the photovoltaic (PV) and electronic industry and in medical application [1, 19–21].

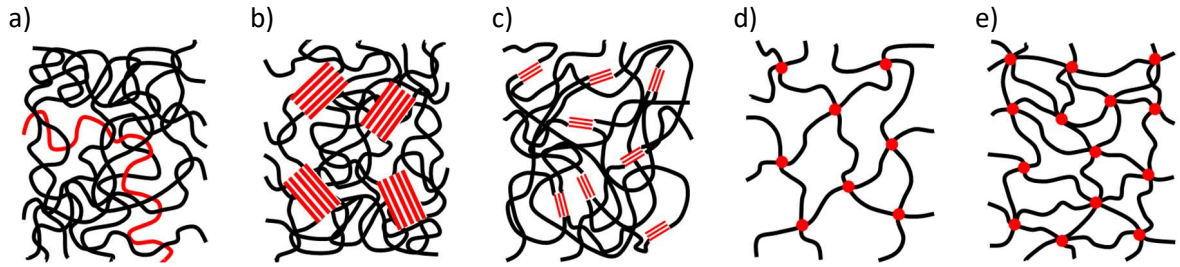

Figure 2 Different types of polymer structures: a) linear amorphous thermoplastic polymer, b) partially crystalline (red areas) thermoplastic polymer, c) physically cross-linked elastomer, and covalently cross-linked polymers with d) low and e) high cross-link density.

This dissertation focuses exclusively on two groups of thermoplastic polymers:

Polyamide (PA)

Polyamide (PA) is produced through the polycondensation of a diamine and a dicarboxylic acid monomer, as shown in Figure 3. A typical example is the reaction of adipic acid and hexamethylenediamine to form nylon-type polymers [18]. Polyamides are among the most important technical thermoplastics, offering excellent mechanical properties, high toughness, thermal stability, and chemical resistance [18–20]. These properties can be further tailored to specific applications through careful selection of raw materials and manufacturing parameters. Polyamides find applications in machine and vehicle construction, electronics, construction, packaging, and the textile industry [9, 22, 23]. As for example the widely used Nylon yarn [24].

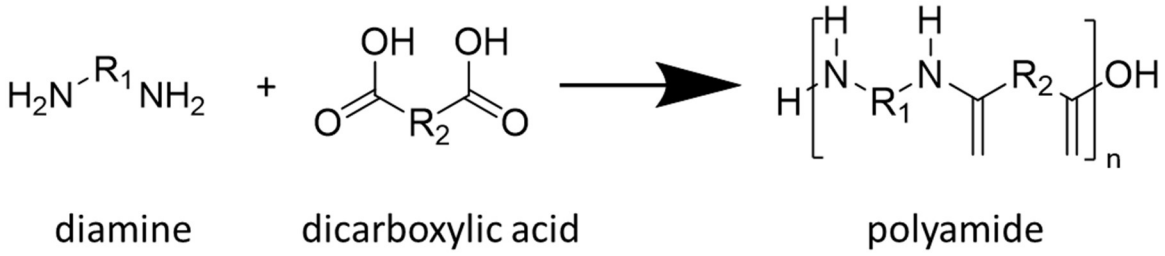

Figure 3 Polycondensation reaction of a diamine and a dicarboxylic acid to form a polyamide [18].

Thermoplastic Polyurethane (TPU)

Thermoplastic polyurethane (TPU) is synthesized via the polyaddition of isocyanates with alcohols, as illustrated in Figure 4 [18]. TPU's versatility lies in its tunable copolymer chemistry, enabling the production of soft rubbers, rigid plastics, or soft-hard hybrids. It exhibits excellent abrasion resistance, flexibility at low temperatures, and good biocompatibility [25–29]. TPU is widely used in additive manufacturing (e.g., 3D printing), the automotive sector, and the production of thin films, sheets, and textile coatings [30, 31].

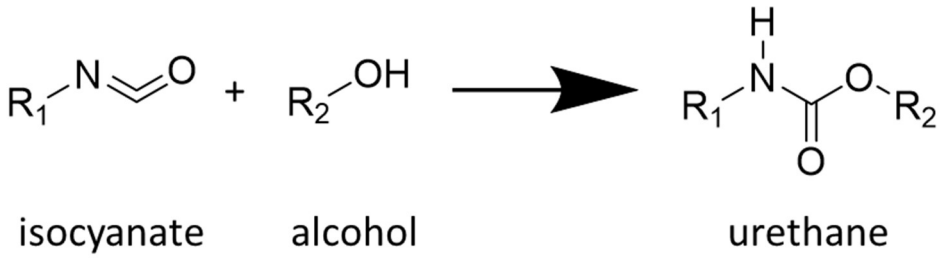

Figure 4 Polyaddition of an isocyanate and an alcohol to form a polyurethane [18].

2.1.3 Percolation threshold

Electrically conductive polymer composites primarily consist of two components: a polymer matrix and an electrically conductive filler material [18]. Epoxy resins are commonly used as the polymer matrix, particularly in electrically conductive adhesives (ECA) [32–34]. Thermoplastic polymers, such as thermoplastic polyurethane (TPU) or polyamide (PA), are also employed for applications like flexible sensors [2]. Silver (Ag) and gold (Au) are commonly used as electrically conductive filler materials, typically in the form of flake- or sphere-shaped micron-sized particles [6, 18, 35]. Polymers have very low intrinsic electrical conductivity, approximately 10^{-15} S/cm [18]. Achieving high conductivity requires surpassing the percolation threshold - the minimum particle concentration needed to form a continuous particle network capable of conducting electricity through the insulating polymer matrix [18]. For example, by using Ag as a filler, conductivity values between 100 and 10,000 S/cm can be attained [2, 6, 36].

Figure 5 a) illustrates the relationship between particle volume fraction and the electrical conductivity of an adhesive filled with conductive particles. At very low volume fractions (typically below 20 vol%) [18], particle-particle contacts are minimal, and conductivity remains close to the intrinsic value of the polymer (10^{-15} S/cm). As the particle volume fraction increases and the percolation threshold is reached, conductivity rises sharply due to the formation of continuous conductive particle paths. Beyond this threshold, further increases in particle concentration result in only slight improvements in conductivity. However, excessive particle loading negatively affects the mechanical properties of the composite and

significantly raises costs [37]. Thus, optimizing the particle volume fraction is essential when designing new formulations.

Figure 5 b) illustrates the structure of a particle-filled adhesive below the percolation threshold, where no continuous conductive paths are formed. In contrast, Figure 5 c) presents a schematic of a particle-filled adhesive above the percolation threshold, featuring a network of conductive particles (white dashed line) capable of transmitting electrons through the insulating polymer matrix. The percolation threshold particle concentration depends on various factors, including particle size [15], size distribution [16], shape, alignment [38], and adhesive thickness [39]. Flake-shaped particles with diameters below 20 µm are commonly used, as their higher surface-to-volume ratio reduces the percolation threshold significantly [40].

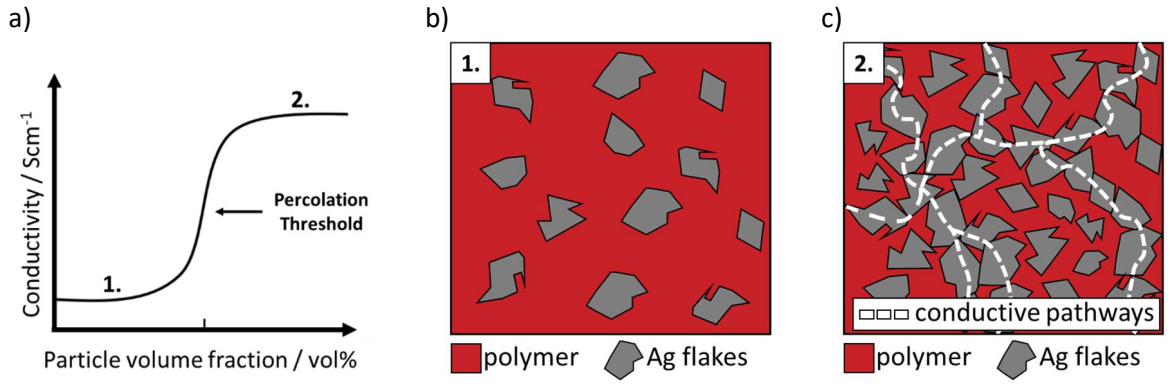

Figure 5 a) electrical conductivity ($S \cdot cm^{-1}$) as a function of particle volume fraction in an adhesive filled with electrically conductive particles. Schematic representation of a particle-filled polymer composite b) below the percolation threshold and c) above the percolation threshold, with the white dashed lines indicating particle-particle contacts facilitating electron transmission through the polymer matrix.

2.1.4 Filler materials

Silver (Ag) particles are the most common filler material for ECAs due to their high electrical conductivity, ease of processing, and good malleability [41]. Among cost-effective metals such as Ag, copper (Cu), and nickel (Ni), silver stands out as the only one that forms an electrically conductive oxide, providing superior aging stability [41]. To enhance the aging properties of other metals like Cu, a thin layer of silver can be applied to the surface of Cu particles [41, 42]. This way it is possible to reduce the total amount of silver and simultaneously obtain similar electrical conductivities and aging behavior [43]. To reduce the total metal mass even further silver-coated polymer or glass particles can be used as well [6, 44]. Since the density of polymer and glass are lower (1 – 3 g/cm^3) in comparison to Cu and Ag (8 – 11 g/cm^3) the mass needed to overcome the percolation threshold – which is dependent on the total occupied particle volume in a polymer matrix – is much lower that for pure metal particles. However, it is imported to note that the electrical conductivity is reduced in those systems as well [6]. To further enhance conductivity and aging properties, Cu and Ag nanoparticles can be incorporated into formulations filled with Ag and Cu microparticles. These nanoparticles promote sintering between the microparticles at relatively low temperatures (below 200 °C), reducing contact resistance and minimizing the free metal surface area between particles, thereby significantly improving aging stability [45]. Even pure Cu particle based pastes can reach a certain aging stability using this approach [46].

Furthermore, carbon-based materials such as carbon black (CB) and carbon nanotubes (CNT) can be used as alternatives to metal particles, although their electrical conductivity is typically at least one order of magnitude lower than that of metal-filled ones [47, 48]. However, given that carbon is one of the

most abundant elements on Earth, it presents an appealing alternative for industries requiring large quantities of conductive materials, such as the PV sector [49].

2.2 Application in wearable electronics

2.2.1 Introduction

The Internet of Things (IoT) is envisioned as a world interconnected by sensors, enhancing various aspects of human life [50, 51]. In this context, smart wearables have emerged as a significant extension of the well-established smartphone, finding applications across multiple end-user sectors such as lifestyle computing, healthcare, sports, and personal safety [52–54]. Equipped with sensors, these wearables can monitor both the environment and the user, while integrated actuators enable them to interact, respond, and adapt to different conditions [55]. Popular products such as smartwatches, wristbands, and earwear have already gained widespread adoption, with over 200 million devices shipped in 2023 [56]. To further enhance the integration of smart capabilities, electrically conductive polymer composites are being developed. These materials can be embedded into everyday tools and even textiles, often with the goal of converting motion into electrical signals or vice versa. Among the most commonly used sensor technologies in smart wearables are piezoelectric, resistive, and capacitive sensors. Each type offers distinct advantages and limitations, as summarized in Table 1.

Table 1 Properties of different sensor techniques [57].

Category	Advantages	Disadvantages
Piezoelectric sensor	• Self-powered • Simple structure • Fast response time	• Unable to static sensing • Drift over time • Lower reliability
Resistive sensor	• Low-cost • Simple fabrication • Well-researched	• Affected by hysteresis effect • Sensitive to temperature and humidity
Capacitive sensor	• Simple structure • Temperature independent • Low power consumption • Low-pressure detection limit • Fast dynamic response	• Low sensitivity • Susceptible to environmental interference

This dissertation focuses on capacitive sensors, which are further discussed in section 2.2.2. Additionally, section 2.2.3. presents various manufacturing processes and strategies for integrating electrical conductivity - and thus, smart functionality - into textiles.

2.2.2 Flexible capacitive pressure sensor

A flexible capacitive pressure sensor consists of two flexible electrodes that sandwich a dielectric layer as depicted in Figure 6. The capacitance of the device can be calculated according to equation *(1)*, where ε_0 describes the permittivity of the medium, and ε_r the relative permittivity of the dielectric material of the capacitor. δ is the distance between and A the facing area of the two electrodes. These devices can detect external pressure stimuli by changes in the device's capacitance. For example, if pressure is applied by an external force, the distance (δ) between the two electrodes changes, and hence according to equation *(1)* the Capacitance (C) as well.

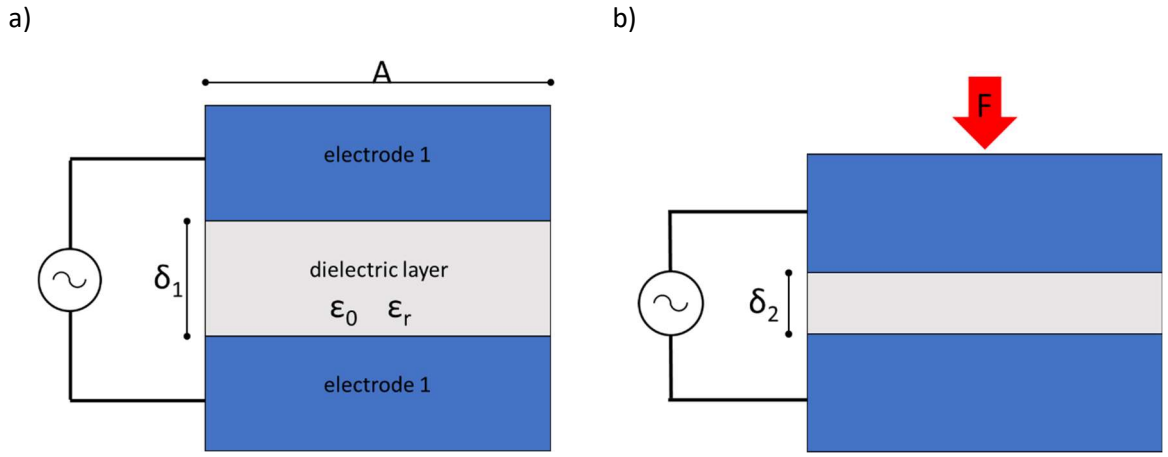

Figure 6 Scheme of a flexible capacitive sensor: a) before and b) during the application of pressure by an external force ($\delta_2 < \delta_1$).

$$C = \frac{\varepsilon_0 \varepsilon_r A}{\delta} \quad (1)$$

A wide range of materials is used in this field to enhance key device characteristics such as high sensitivity, fast response time, and good cycle stability [58]. The dielectric layer must be non-conductive and can be composed of polymers like polydimethylsiloxane (PDMS), thermoplastic polyurethane (TPU), and polyethylene terephthalate (PET) [3, 59, 60]. To improve initial capacitance and capacitance variation, composites with a high dielectric constant are commonly utilized [60]. Additionally, various shapes and porous structures, such as micro pyramids, needle-like formations, and highly porous architectures, are being explored to further enhance device sensitivity [57, 58]. For flexible electrodes, a variety of materials and manufacturing strategies are available, depending on the desired level of integration. Examples include plane comb structures, structured electrodes, textile-based dielectric layers, and single-yarn structures [3, 61]. However, in principle, they all function as illustrated in Figure 6. The next section will discuss the integration of electrical conductivity across different levels of integration.

2.2.3 Manufacturing methods of wearable electronics

Wearable electronics usually, consist of sensing and actuating capability like the capacitive pressure sensor (Figure 6), which consists of a combination of electrically conductive and non-conductive materials as presented in section 2.2.2, often integrated into textiles. Textiles are hierarchical materials which are made of yarn or threads which are made of fiber. Fiber is defined as a thin, flexible material with high aspect ratio, with diameters between 10 and 50 µm and a length between 15 and 150 mm [5]. These dimensions match the dimension of common natural fiber like cotton and wool [5]. This fiber, natural or synthetic, is spun to yarn, which can subsequently be used to manufacture fabrics by weaving or knitting [5]. This hierarchical structure enables the integration of sufficient electrical conductivity and hence the possibility of creating smart capabilities on different length scales. This section will present a few application methods on different hierarchical levels.

Fiber

Electrically conductive fibers can be intrinsically conductive or made conductive through coating with electrically conductive materials. Carbon fiber, a common intrinsically conductive material, is derived from polyacrylonitrile (PAN) through a pyrolysis process [62]. It is widely used in smart applications, such as strain sensors (resistive sensors) and for monitoring damage or temperature changes in materials

like cementitious composites [63–65]. In these applications, variations in the composite material can be detected by tracking changes in the electrical resistivity of the fiber network, which is influenced by factors such as temperature, moisture, or mechanical deformation. Beyond traditional carbon fiber manufacturing based on PAN, fibers can also be produced using carbon nanotubes (CNTs), which enhance strength as well as electrical and thermal conductivity [66]. Another reported approach involves coating nylon fibers with an intrinsically conductive polymer, allowing the fiber to retain its original mechanical properties while gaining electrical conductivity [64].

Yarn and Thread

Intrinsically conductive fibers, such as carbon fiber, can be spun into yarn or threads (thinner yarn) [67, 68]. Additionally, thin metal threads with diameters ranging from 10 to 60 µm can be knitted into non-conductive yarn [67, 68], or non-conductive yarn can be coated with electrically conductive materials through various processes. Techniques such as yarn dip-coating in solutions filled with metal nanowires [69–71], spinning CNT-spray-coated cotton fibers [72], or applying electrically conductive polymer coatings [73] enable the formation of electrically conductive pathways through the yarn surface. One of the key advantages of conductive yarn is its compatibility with conventional sewing and weaving equipment, making it easy to process for a wide range of applications [72, 74]. Depending on the use case, conductive yarn can serve as a simple electrical connector [73, 74], a chemical sensor [70], a strain or pressure sensor [70, 71, 75], an artificial muscle [73], or even a thermostat [71], demonstrating its versatility in numerous applications.

Textile

Instead of manufacturing electrically conductive fibers or yarns that are sewn into textiles, an alternative approach involves directly applying a polymer-based ink, paste, or filament filled with electrically conductive particles onto the fabric. This can be achieved through dispensing, screen printing, or extrusion techniques. Such a method enables various applications, including flexible wiring, pressure and strain sensors for data gloves, and electrocardiograph systems [2, 3, 76–78].

2.3 Applications in photovoltaics

2.3.1 Introduction

Photovoltaics (PV) currently offers the lowest levelized cost of electricity worldwide. As the global economy shifts toward sustainability and near-total reliance on renewable energy sources, PV module production is projected to reach between 1 and 3 terawatts by 2040 [77]. Although PV costs have dramatically fallen over the past 60 years - from over 100 USD/Wp to approximately 0.1 USD/Wp [78] - the dependency on rare materials such as indium, bismuth, and especially silver could jeopardize these production targets. As of today, the PV industry already requires 10 % of the annual silver production [79]. Consequently, research is increasingly focused on developing more efficient and cost-effective solar cell technologies and interconnection methods that either enhance yield or reduce reliance on scarce materials [80, 81]. Section 2.3.2 introduces the fundamental functionality of solar cells and outlines the most common solar cell technologies in use today. Section 2.3.3 describes the construction of PV modules, while Section 2.3.4 explores the role of electrically conductive adhesives (ECAs) in interconnecting solar cells. Finally, Section 2.3.5 presents the TECC-Wire interconnection method - an adhesive-based solar cell interconnection technique that has been extensively investigated in this dissertation.

2.3.2 Functionality of a Solar-Cell

Crystalline silicon (Si) solar cells are the most commonly produced type of photovoltaic devices. These cells function as flat p/n semiconductor diodes that convert light into electrical current via the photoelectric effect, as described by equation (2) [82].

$$\boldsymbol{E = \frac{hc}{\lambda}} \tag{2}$$

Where E is the absorbed energy, *h* is Planck's constant, c is the speed of light, and λ is the wavelength of the incident light.

When light with energy E is absorbed by the semiconductor, it generates electron-hole pairs - electrons (negative charge carriers) and holes (positive charge carriers). If this process occurs within the space charge region, located at the interface between the n-type and p-type layers (n/p-junction), the built-in electric field, formed by ionized dopants, directs electrons toward the n-type layer and holes toward the p-type layer. This directed movement of charge carriers leads to the generation of electrical current. To facilitate charge collection, silver (Ag) metal lines, also called fingers, and busbars are applied to the top surface. On the rear side, either Ag lines and busbars or a full aluminum (Al) layer is used (depending on the technology) for charge collection and interconnection purposes, which will be explained in detail in the next chapter [82]. Figure 7 provides an illustration of a solar cell and depicts electron-hole pair formation at the p/n junction. Recombination is a critical factor that must be considered. If charge carriers are not successfully separated and extracted, they may recombine either within the bulk of the wafer - typically at defect sites - or at interfaces, such as dangling bonds which lowers the efficiency of the solar cell. The underlying physical mechanisms are discussed in reference [83].

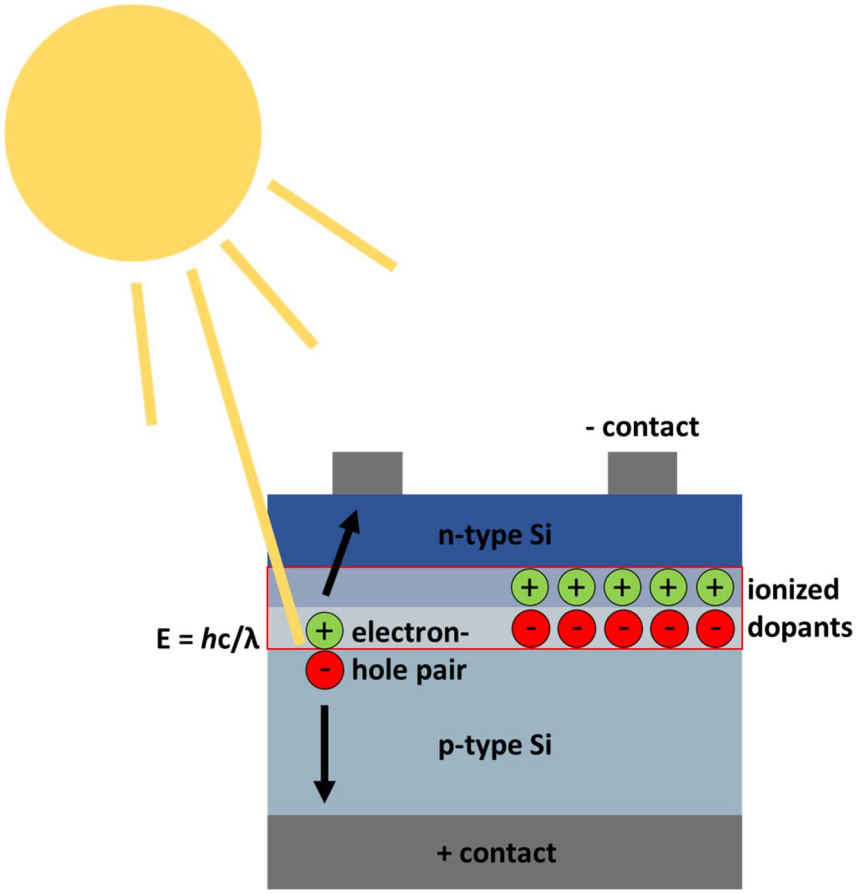

Figure 7 P-type crystalline Si solar-cell at the p/n-junction.

Over the past decades, various solar cell technologies have been extensively researched and introduced to the market. The following section highlights three significant developments in solar cell technology. However, it is important to note that many other technologies are being explored, but covering them all would exceed the scope of this dissertation.

Passivated emitter and rear cell (PERC)

The passivated emitter and rear cell (PERC) is currently the leading technology in industrial solar cell production, holding a 64 % market share in 2023 [80]. Figure 8a) illustrates the cross-sectional structure of a PERC cell. This solar cell consists of several critical layers and components. At its core is a p-doped crystalline silicon wafer, overlaid with an n-doped emitter layer, forming the essential p-n junction for photovoltaic energy conversion. To enhance light absorption and reduce reflection, the top surface is coated with a blue or black passivation and anti-reflection layer. Additionally, a local back surface field and passivation layer are integrated to minimize recombination losses at the contacts, further improving efficiency [84, 85]. However, due to its limited power conversion efficiency (PCE) of approximately 24 % [80], more advanced cell concepts are rapidly gaining market share, particularly the tunnel oxide passivated contact (TopCon) solar cell.

Tunnel oxide passivated contact solar cell (TopCon)

This technology, which held a 29 % market share in 2023, is expected to grow to 53 % over the next decade, with an anticipated efficiency of around 26 % [80]. A TopCon cell consists of a n-type silicon substrate with a p-doped emitter on the front side [86, 87]. To minimize surface recombination rate, an Al_2O_3 passivating layer is applied [86, 88], while a front-side anti-reflection coating enhances light absorption. At the rear, an ultrathin tunneling layer of SiO_2 acts as an electron transport layer [89]. A thin, heavily n-doped poly-Si layer at the back forms an Ohmic contact, enabling photogenerated

electrons to tunnel efficiently through the SiO_2 layer [89]. Figure 8b) depicts the cross-sectional structure of a TopCon cell.

Silicon heterojunction cell (SHJ)

The silicon heterojunction (SHJ) cell is another highly efficient solar cell technology, expected to expand its market share from 5 % in 2023 to approximately 19 % over the next decade [80]. SHJ cells are projected to achieve mass production efficiencies of 26.6 % to 27.2 %, surpassing the performance of both PERC and TopCon technologies [80]. An SHJ cell consists of an n-type crystalline silicon wafer, typically 140 to 160 µm thick, sandwiched between an intrinsic and a p- or n-type amorphous hydrogenated silicon layer (<1 µm). The amorphous silicon layer effectively minimizes charge carrier recombination, ensuring efficient charge collection [83, 90]. Additionally, a transparent conductive oxide (TCO), commonly indium tin oxide (ITO), covers the doped layers, facilitating lateral charge transport to the metallization fingers [83]. Although more efficient, SHJ cells are more expensive to produce than PERC or TopCon cells, primarily due to their temperature sensitivity. Since SHJ cells cannot withstand temperatures above 200 °C, the conventional Ag metallization process, which requires approximately 800 °C, is not viable. As a result, specialized low-temperature metallization pastes have been developed. However, these pastes have lower electrical conductivity, requiring a larger finger cross-section to compensate, which further increases production costs [91].

Furthermore, all three cell types (PERC, TopCon, and SHJ) can be designed with a bifacial structure, allowing sunlight absorption from both the front and rear sides of the cell. This feature enhances overall efficiency and energy yield [92, 93]. Here just for the SHJ-cell a bifacial configuration is depicted (Figure 8c).

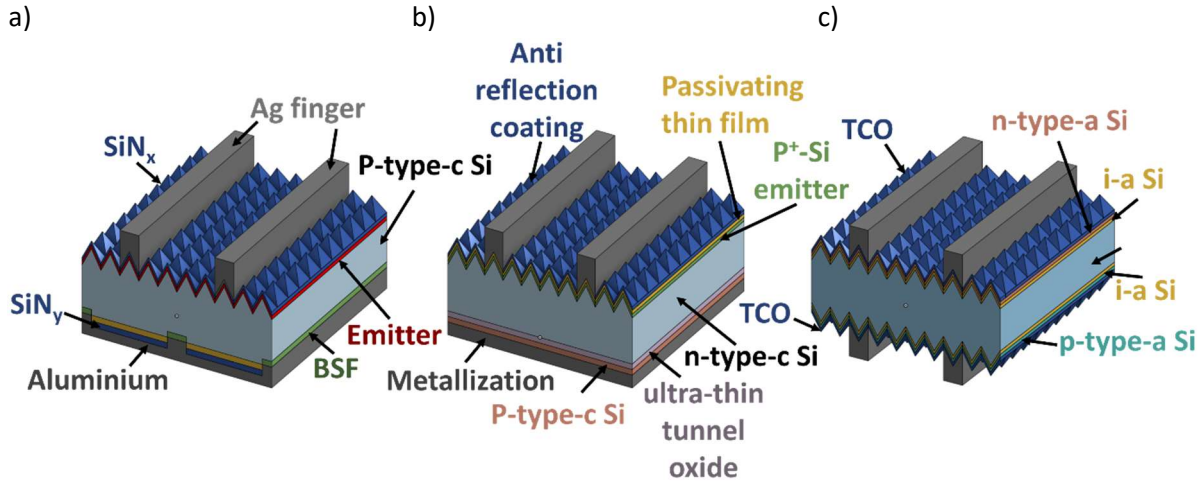

Figure 8 Different solar cell technologies: a) PERC [94] b) TopCon-Cell [95], c) SHJ Cell [92].

2.3.3 Module Design

In a photovoltaic (PV) module, multiple individual cells are electrically connected to enhance power output, while also providing protection to the electrical circuits from environmental factors and ensuring structural integrity. To boost the power output, solar cells are typically interconnected using thin silver coated copper wires (ribbons). The interconnection process typically involves soldering the ribbons with tin-lead-based solder (SnPb) at temperatures between 220 °C and 260 °C to the front-busbars of one cell and the rear side of the next cell. The machines responsible for this process are called stringers, which are optimized for high-speed interconnection, achieving an interconnection rate of approximately two seconds per cell [32]. This process forms a row of interconnected cells, known as a string. These strings are then linked together to assemble the complete module. Today, the standard number of wire

connections between each cell is four or five. However, certain technologies, particularly those used in silicon heterojunction (SHJ) cells, employ even more - up to 15 much thinner round wires. This approach, known as Multi-Wire technology, reduces shading, enhances efficiency, and decreases the amount of silver (Ag) required for metallization [96, 97]. These benefits are primarily attributed to the round shape, which allows more sunlight to be reflected at angles that eventually reach the solar cell surface. Additionally, using a greater number of thinner wires reduces the series resistance, thereby enhancing overall efficiency [96]. Depending on the module's size, cell count, and technology, its power output typically ranges from 300 to 500 watts [80, 82]. In addition to the cells and wiring, the module must be protected from environmental factors. Thus, the structure is typically encapsulated in ethylene vinyl acetate (EVA), which undergoes cross-linking during a lamination process at around 150 °C. This process forms a bond with the front glass. The front glass usually has a low iron oxide concentration to maximize transparency. The rear side of the module is typically sealed with glass, but polymer foils such as polyvinyl fluoride (PVF) and polyethylene terephthalate (PET) are also commonly used. To ensure structural integrity, the module is mounted in an aluminum frame [82]. The structure of such a PV module is depicted in Figure 9.

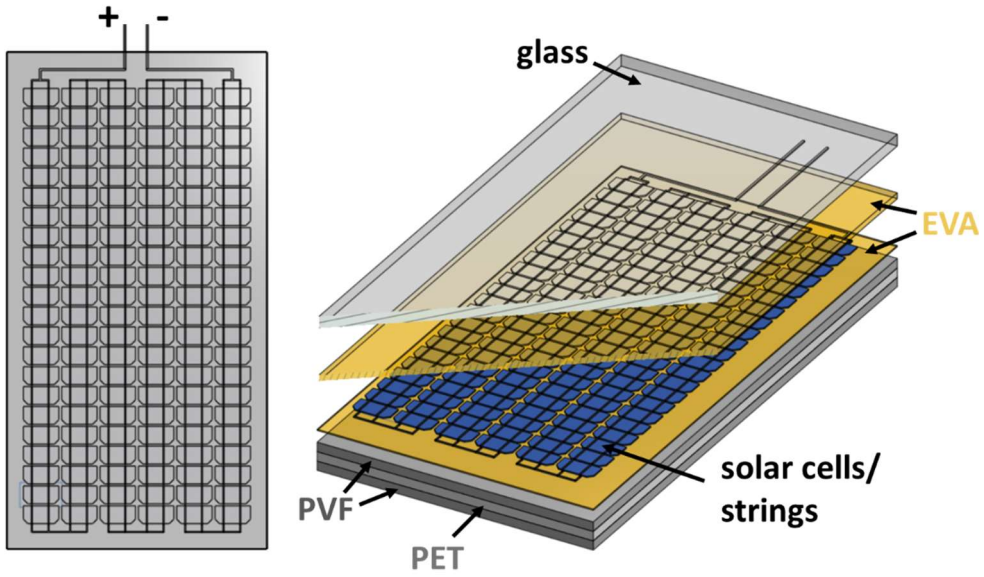

Figure 9 Conventional structure of a PV module [82].

2.3.4 Electrically conductive adhesives in photovoltaics

As described in section 2.1, electrically conductive adhesives (ECAs) consist of a polymer-based adhesive filled with electrically conductive particles, primarily silver (Ag), to surpass the percolation threshold [18]. ECAs can serve as an alternative to solder for interconnecting solar cells (PERC, TopCon, SHJ, etc.) to modules, as detailed in section 2.3.3 [33, 98, 99]. One key advantage of ECAs is their significantly lower processing temperature (<200 °C) compared to conventional SnPb-solder interconnections (220 - 260 °C). Additionally, they do not require lead or flux, which drastically reduces toxicity. ECAs also offer greater flexibility than solder, mitigating thermomechanical stress within the module [34, 100]. Mass-production stringers for ECAs are already available on the market, such as those offered by Teamtechnik GmbH [33].

However, a major drawback of ECAs is their high silver content. Commercially available ECAs for solar cells typically contain around 80 wt% Ag, making them more expensive than traditional soldering [100]. As a result, SHJ cells are currently the only cell technology available on the market where ECAs

are under consideration, given their requirement for process temperatures below 200 °C. Even in this case, ECAs must compete with low-temperature solder materials based on indium (In) or bismuth (Bi), which also have melting points below 200°C [101]. To make ECAs more competitive, silver consumption must be reduced. This can be achieved by applying adhesive in dot patterns rather than continuous lines for cell-ribbon interconnection [34]. Additionally, Ag-coated copper particles offer a promising alternative, though, to our knowledge, they are not yet commercially available at scale [32]. All commercially available ECAs used in PV modules today are either epoxy- or acrylic-based and undergo cross-linking during interconnection, as described in section 2.1.2 [21, 32]. This process involves monomers forming covalent bonds to create a continuous, sample-spanning network, making it irreversible.

2.3.5 Smart-Wire

Another approach, already commercialized by the Swiss company Meyer Burger, is the so-called Smart-Wire interconnection [102]. This method uses an adhesive foil that incorporates 18 thin copper wires. These copper wires are coated with an indium or bismuth-based solder, making it a low-temperature interconnection method applied at temperatures below 150°C. Therefore, it can be considered both an adhesive and a solder-based interconnection technique. Initially, good adhesion between the cells and the wire is ensured by the adhesive foil, while a mechanically stable electrical contact between the fingers and the wire is provided by the low-temperature solder alloy [102].

2.3.6 TECC-Wire

TECC-Wire technology is a relatively new adhesive-based interconnection method that is still under development. TECC stands for Thermoplastic and Electrically Conductive Coated Wire [103]. The name itself highlights the key difference from other adhesive-based interconnection methods, which typically rely on cross-linking epoxy or acrylic adhesives. Instead, TECC uses a thermoplastic material that, when heated above its melting temperature, transitions into a sticky, molten state. Upon cooling, the material solidifies again, making it a hotmelt adhesive [17]. This process is fully reversible, as described in section 2.1.2., and this reversibility is the most crucial characteristic of the TECC-Wire interconnection method. Unlike traditional methods where electrically conductive adhesives (ECA) are applied via screen printing just before the wire is placed during the stringing process [33], TECC-Wires are pre-coated with adhesive in a separate step. The precursor for this coating is a wire enamel containing a thermoplastic polymer, a solvent, and electrically conductive material. This formulation allows it to be applied using conventional wire-coating machines, which are typically used for producing thin wires for magnet coils. These machines are well-suited for high-volume production, meeting the demands of the photovoltaic (PV) industry [104]. In this process, a thin layer of electrically conductive thermoplastic adhesive is applied to the wire. The key advantage of TECC-Wire technology is that it eliminates the need for additional adhesive or solder during the stringing (cell interconnection) process. The coated wire can be placed directly onto the solar cell. By applying heat and pressure, a mechanically robust and electrically conductive interconnection is formed. Since the thermoplastic adhesive is pre-applied exactly where needed - on the wire - this approach is highly efficient, easy to handle, and results in a cleaner process. A two-cell TECC-interconnection including an image of the cross-section of the interfaces between cell adhesive and wire is displayed in Figure 10.

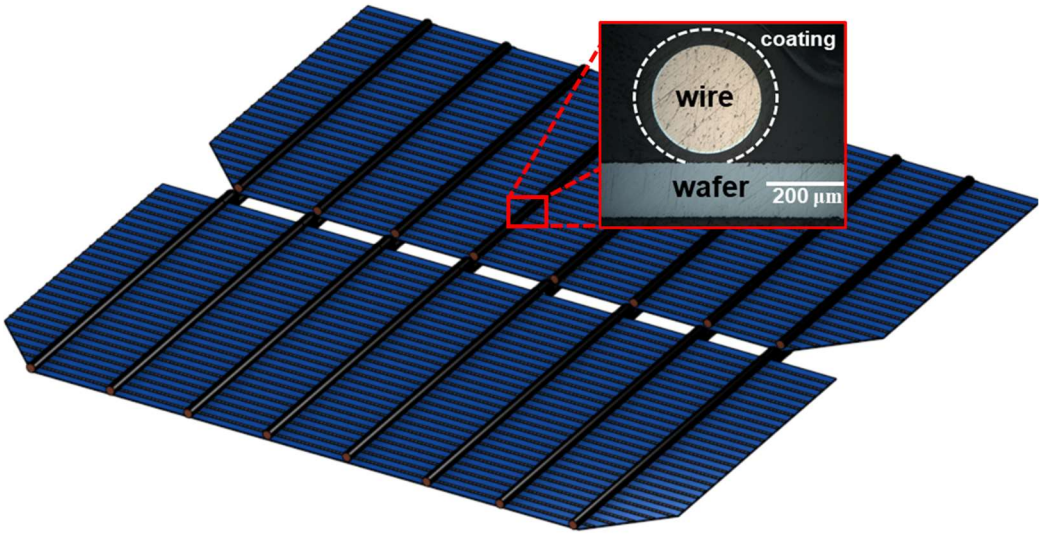

Figure 10 Schematic of two solar cells interconnected by TECC-wires, with a cross-sectional view illustrating the interfaces between the wire, coating/adhesive, and wafer.

Chapter 3 Motivation and manuscript outline

The previous chapters explored electrically conductive polymer composites, highlighting their potential applications in wearable smart electronics and their role as electrically conductive adhesives for interconnecting solar cells in PV modules. As both fields evolve rapidly, so do the material requirements. This thesis investigates formulation strategies to minimize the use of rare materials while proposing innovative applications in both domains.

A key feature of these composites is the formation of a percolating network of conductive particles, typically silver, within the polymer matrix. For large scale applications, especially in the photovoltaic sector, it is critical to minimize the use of these valuable and scarce materials, thus lowering the percolation threshold. Existing literature suggests several strategies to optimize electrical conductivity while reducing silver particle consumption. Factors such as particle shape, size distribution [18] and surface properties [105] play an important role. By systematically adjusting these parameters, conductivity can be increased while silver content can be reduced. In addition, the incorporation of specific chemical compounds - such as iodine salts [35], organic acids [105] and aldehydes [106]- or the introduction of immiscible liquids into the bulk phase [107] has been shown to improve conductivity. However, these modifications not only improve electrical performance, but also affect the rheological behavior and processability of the formulations. Chapter 4 therefore focuses on the effect of iodine salts on Ag-filled adhesives, which have been widely used to improve the conductivity of these polymer composites [35, 108–110]. It examines how different iodine components affect not only the electrical conductivity, but also the particle microstructure and rheological properties of the Ag-filled adhesives, essential parameters for typical application methods such as dispensing or screen printing [2, 110].

In Chapter 5 and 6, the formulation strategy explored in Chapter 4 is utilized to develop innovative material platforms, advancing the development of smart textiles and interconnection methods for PV modules.

The rapid emergence of smart technologies has created a demand for robust, flexible, and electrically conductive materials that integrate seamlessly into everyday life. This need is particularly evident in textiles and clothing, where electrically conductive yarns can serve as a basic component for embedded electrical connectors and sensors. These yarns can be woven alongside conventional fibers and yarn, enabling the fabrication of smart textiles without compromising the mechanical properties of traditional textiles. As discussed in Chapter 2 section 2.2, various methods for producing electrically conductive yarns have been explored in the literature [69–71]. Chapter 5 of this thesis introduces a novel, high-throughput approach for producing electrically conductive yarn, inspired by wire coating techniques commonly used for magnetic coils [104]. This method applies an Ag-based polymer coating - developed using the production strategy outlined in Chapter 4 - onto standard nylon yarn, forming a conductive layer. To validate this approach, a basic capacitive sensor was fabricated, demonstrating the feasibility and effectiveness of the proposed technique.

Electrically conductive adhesives present a promising alternative to low-temperature solders such as indium and bismuth, offering processing flexibility that makes them particularly attractive for photovoltaic applications. As detailed in Chapter 2, section 2.3.6, TECC-Wire represents an innovative adhesive-based technology. Unlike conventional epoxy-based adhesives, TECC-Wire employs a thermoplastic electrically conductive wire coating [103, 112, 113]. However, due to its novelty, research on its material properties and performance remains limited, leaving several critical aspects unexplored. A key research gap is the lack of data on TECC-Wire's electrical conductivity, with few studies detailing the materials used or their conductive performance [103, 112, 113]. To address this topic, Chapter 6

introduces a highly electrically conductive, silver-based thermoplastic polyamide adhesive wire coating. This formulation leverages the iodine-induced Ag-particle structure formation discussed in Chapter 4. Notably, the new adhesive is compatible with conventional high-throughput wire coating machinery, making it a practical solution for the growing demands of the solar industry. Furthermore, it establishes a versatile material platform for future research, including investigations into alternative conductive fillers such as silver-coated glass and copper particles.

Chapter 4 Iodine-induced microphase separation

Full title: *Iodine-Induced Microphase Separation Controls Flow Behavior and Electrical Conductivity of Silver-filled Polymer Composites*

Authors: *Jonas Marten, Jennifer S. Urallar, Thao M. Duong, Patrick Théato, Norbert Willenbacher*

Status: *published* [114]

Bibliographic data: *Applied Materials and Interfaces;*
DOI: https://doi.org/10.1021/acsami.5c09040

Abstract

Silver-filled electrically conductive polymer composites play a crucial role in various fields of electronics, such as die-attach, chip packaging, solar cell interconnection, and soft printed electronics. This study explores the use of iodine-induced microphase separation of silver particles to achieve high electrical conductivity in the corresponding polymer composites at low particle loading thereby preserving this precious resource. Three iodine salts: 1-butyl-3-methylimidazolium iodide, potassium iodide, and sodium iodide were directly mixed into thermoplastic polyurethane solutions with varying contents of micron-sized silver particles. This resulted in a paste-like suspension texture, indicating the formation of a percolating particle network already in the wet state. The electrical conductivity of the corresponding dry films improved from 10^{-5} S/cm without added iodine to 500 or 2,600 S/cm at 12 or 20 vol% silver, respectively, irrespective of the iodine type. Thermogravimetric analysis and infrared spectroscopy confirmed that iodine removes lubricants from the silver particle surfaces, facilitating stronger particle attraction. Accordingly, scanning electron microscopy revealed iodine-induced microstructural heterogeneities. These findings highlight the potential of iodine-modified, silver-filled polymer solutions as a straight forward, cost-efficient approach to producing high-performance conductive materials for electronic applications.

4.1 Introduction

Electrically conductive polymer composites are used as adhesives in the interconnection of temperature-sensitive solar cells to form photovoltaic (PV) modules [6, 115], in conventional chip attachment [4] and in new soft electronic applications [2, 116], including electronic textiles and portable devices [117]. They are processed as solvent-based drying or reactive, curing pastes in screen-printing [2, 118], jetting [119], dispensing [120] or direct ink writing operations [121]. Recently, electrically conductive polymer filaments have been introduced suitable for material extrusion-based additive manufacturing [3]. Compared to solder-interconnections, these composites present several advantages including lower processing temperatures, larger deformability, lower thermomechanical fatigue, applicability on non-solderable substrates, and lower toxicity [1, 101, 122]. Moreover, the properties of electrically conductive polymer composites can be fine-tuned with respect to their electrical, thermal, mechanical, or physical characteristics (e.g. wetting and flow) to meet the specific requirements of different applications and manufacturing processes. Thereby, they offer not just electrically conductive and mechanically stable solder replacement but also the integration of sensing capabilities, as for example in flexible pressure sensors [1, 123, 124]. However, despite these advantages over solder, the electrical conductivity of polymer composites – typically ranging from 100 to 10,000 S/cm [1, 2, 6] – is still at least one order of magnitude lower than that of commercial solder, which has an electrical conductivity of approximately 66,000 S/cm [101].

For most applications that demand higher conductivity, silver (Ag) is commonly used as the conductive filler material and typically, electrically conductive adhesives (ECA) are filled with at least 20-30 vol% micron-sized Ag-particles in order to reach the percolation threshold – the minimum particle concentration required to form a sample spanning particle network providing electrical conductivity [18]. It should be noted, however, that the percolation threshold depends on the shape and size of the dispersed particles and may be substantially reduced by using more anisotropic particles [18].

In recent years, copper particles have been explored as a highly conductive, but cheaper alternative to Ag particles, particularly for cost-sensitive applications such as solar cells and PV modules. Copper particles are, however, prone to oxidation at ambient temperature and moisture conditions, and are therefore not suitable for many applications [122]. Therefore, it is important to advance Ag-based materials to achieve higher electrical conductivity and simultaneously reduce Ag consumption.

Capillary suspensions are ternary systems including a particulate solid phase and two immiscible fluids [125]. When small amounts of a second fluid, immiscible with the bulk fluid (e.g., the polymer matrix of an electrically conductive composite), are introduced, strong capillary forces drive the self-assembly of a particle network at a low percolation threshold [107], thus enabling high thermal or electrical conductivity at a low content of conductive particles [2, 3, 107].

Another approach to improve the electrical conductivity of an Ag-filled polymeric composite is the removal of organic surface layers, so-called lubricants, often fatty acids, that form silver carboxylates on the Ag particle surfaces [105]. These lubricants are required for agglomerate breakup and uniform dispersion of the Ag particles in an organic matrix, but the insulating layer also lowers the electrical conductivity of the materials [126].

The removal of lubricants can be facilitated, e.g., utilizing a short-term annealing method in which the Ag particles are stored at high temperature (600-800 °C) to decompose the fatty acids and silver carboxylates [127]. Moreover, a chemical treatment of the Ag particle with short-chain organic acids [105], aldehydes [106] or diethylene glycol butyl ether [128] can be used to remove the non-conductive

insulating lubricant layer from the Ag particle surface, thus improving the conductivity of Ag-polymer composites as well. Notably, this treatment increases the viscosity of the Ag-filled composites in the low shear rate regime (< 0.1 s^{-1})[105], indicating the formation of a percolating particle network [129] which may be attributed to the reduced steric stabilization due to the removal of the lubricant layer.

Another approach uses halide compounds like potassium iodide (KI) or sodium iodide (NaI) to remove the fatty acids and silver carboxylates from the Ag particle surfaces to drastically improve the electrical conductivity of corresponding composites [35, 108–110]. It was shown that the iodine ion can replace the silver carboxylates on the Ag particle surface, forming silver iodide (AgI) which is smaller and more conductive than the lubricants and thus enhances the electron tunneling between neighboring particles [35]. Additionally, the AgI formed on the Ag particle surface can be transformed back to Ag by a UV light treatment increasing the electrical conductivity of the composite even further [35, 109].

Although these treatments benefit the conductivity, they all include an extra Ag particle treatment that is time-consuming, involves high temperature [127] or a lot of solvent and an additional drying step [35, 105, 108, 109]. This makes the process difficult to scale-up. Additionally, to our knowledge, the effect that iodine treatments might have on structure formation, and hence flow behavior of Ag-filled polymeric composites has not been investigated in depth, so far, but is a key aspect for widely used application methods such as screen printing, jetting, or dispensing.

Consequently, this study aims to enhance the electrical conductivity of Ag-filled polymer composites by incorporating various iodine compounds directly into a thermoplastic polyurethane (TPU)-based, Ag-filled model system.

This approach eliminates the need for additional particle treatment steps, facilitating scalability for large-scale production. Furthermore, the influence of iodine compounds on the flow behavior of the paste and the microstructure of the dry Ag/polymer composite is investigated. A deeper understanding of these parameters is crucial for further improving such materials with respect to their processing, application, and end-use properties.

TPU was selected as a versatile polymeric model system, and three different iodine salts were utilized in this study: KI, NaI, and 1-butyl-3-methylimidazolium iodide (IL), a liquid iodine-based salt previously used to prepare capillary suspensions [2, 3, 107]. The effect of adding these salts on viscosity, yield stress and electrical conductivity of wet pastes, as well as on the microstructure and electrical conductivity of the corresponding dry films was investigated systematically.

4.2 Experimental section

4.2.1 Materials

The thermoplastic polyurethane (TPU) Elastollan Hotbond AH 530 (ρ_{TPU} = 1.15 g/cm^3) was obtained from BASF SE (Ludwigshafen, Germany). The solvent dimethyl sulfoxide (DMSO) (99.5 %) (ρ_{DMSO} = 1.1 g/cm^3), ethanol (99.5 %) ($\rho_{ethanol}$ = 0.789 g/cm^3) and the iodine salts: 1-butyl-3-methylimidazolium iodide (IL) (ρ_{IL} = 1.48 g/cm^3), potassium iodide (KI) (ρ_{KI} = 3.12 g/cm^3) and sodium iodide (NaI) (ρ_{NaI} = 3.67 g/cm^3), were supplied by Carl Roth GmbH (Karlsruhe, Germany). The plate-shaped silver (Ag) particles (Ag Flake Powder FA-S-12) (ρ_{Ag} = 10.49 g/cm^3) were purchased from DOWA Electronic Materials (Tokyo, Japan). The particle size distribution is displayed in Figure 30 of the SI ($d_{50,3}$ = 2.5 µm).

4.2.2 Iodine treatment of the silver particles

A specific amount of Ag particles was suspended in ethanol (100 mL) using a glass beaker and a magnetic stirrer to gently agitate the particles. Subsequently, solutions of IL, KI, and NaI were added to achieve an iodine concentration normalized to the Ag volume (2.00 $mmol_{Iodine}/cm^3_{Ag}$). The suspensions were continuously agitated for 3 hours to ensure thorough mixing. Afterwards, the particles were washed several times with pure ethanol. Finally, the particles were dried at room temperature.

4.2.3 Preparation of the base polymer solution

A 25 wt% solution of TPU in DMSO was prepared as the base solution for all samples. TPU and DMSO were accurately weighed in the correct ratio using a precision balance ME204TE/00 (Mettler-Toledo GmbH, Gießen, Germany). The components were then transferred to a plastic container and placed on a KM 2 small shaker (Edmund Bühler GmbH, Bodelshausen, Germany) where they were mixed thoroughly until the TPU was completely dissolved in the DMSO. This process took approximately 12 hours.

4.2.4 Preparation of the silver-filled polymer solution

A 24.1 vol% solution of TPU in DMSO was prepared as the base solution for all samples. TPU and DMSO were accurately weighed in the correct ratio using a precision balance ME204TE/00 (Mettler-Toledo GmbH, Gießen, Germany). The components were then transferred to a plastic container and placed on a KM 2 small shaker (Edmund Bühler GmbH, Bodelshausen, Germany) where they were mixed thoroughly at room temperature and a rotational speed of 200 min^{-1} until the TPU was completely dissolved in the DMSO. This process took approximately 12 hours.

4.2.5 Rheological characterization of the polymer solution

All experiments were conducted at 20 °C using a stress-controlled rotational rheometer (Physica MCR 501, Anton Paar GmbH, Germany).

The viscosity was determined using a concentric cylinder geometry (inner diameter d = 10 mm, gap width w = 0.843 mm). Each sample was pre-sheared at a constant shear rate of 100 s^{-1} for 30 seconds, followed by a 30-second resting phase to equilibrate the system. Viscosity measurements were then conducted within a shear stress range of 1 Pa < σ < 10,000 Pa.
The yield stress σ_y was determined using a vane-and cup fixture (d = 10 mm) within a shear stress range of 0.5 < σ < 10,000 Pa. Deformation was plotted against the shear stress and using the tangent intersection method [130].

Stress-controlled amplitude sweeps were performed using a plate-plate geometry (d = 25 mm) with a gap size of 1 mm at a frequency of 10 rad/s in a shear stress amplitude range of 1 Pa < σ_0 < 1,000 Pa.

Frequency sweeps were performed using a plate-plate geometry (d = 25 mm) with a gap size of 1 mm, covering the frequency range from 0.1 to 100 rad/s. The measurements were performed at a stress amplitude sufficiently small to provide a linear material response (σ_0 = 1 – 2 Pa).

4.2.6 Infrared spectroscopy (IR)

Infrared (IR) measurements in the Attenuated Total Reflection (ATR) configuration were conducted on Ag particles using a Golden Gate ATR cell with a diamond crystal (Specac LTD, Orpington, UK) mounted in a Tensor II spectrometer (Bruker Optics, Ettlingen, Germany) equipped with a deuterated triglycine sulfate (DTGS) detector. Spectra were recorded over the range of 400 – 4000 cm^{-1} with 64 scans and a spectral resolution of 2 cm^{-1}.

4.2.7 Thermogravimetric analysis (TGA)

Thermal Gravimetric Analysis (TGA) was carried out under oxygen atmosphere using a TGA 7 (PerkinElmer LAS GmbH, Rodgau, Germany) covering the temperature range up to 450 °C at a heating rate of 10 K/min and a sample size of approximately 25 mg.

4.2.8 Differential scanning calorimetry (DSC)

Differential scanning calorimetry (DSC) measurements were performed using a 214 Polyma DSC device (NETZSCH, Selb, Germany). Approximately 10 mg of each sample was accurately weighed and sealed in an aluminum pan with a closed lid. An empty aluminum pan was used as the reference. The heating rate was set to 10 K/min. The thermal program consisted of two heating and one cooling cycle in between, conducted over a temperature range of 40 to 450 °C.

4.2.9 Ultraviolet-visible (UV-Vis) spectroscopy

Ultraviolet-visible (UV-Vis) spectroscopy measurements of the samples were carried out using a PerkinElmer LAMBDA 650 spectrophotometer equipped with a Praying Mantis diffuse reflectance accessory (Harrick). Spectra were recorded in diffuse reflectance mode over the wavelength range of 200 – 800 nm. A horizontal mirror was used as the reference standard to represent 100% reflectance.

4.2.10 Electrical conductivity

The Ag-filled polymer solution samples were first re-mixed in the SpeedMixer at 1,700 rpm for 90 seconds. Subsequently, the pastes were transferred into a mold (width = 4.87 mm, depth = 2.08mm, length = 89.1 mm). The electrical resistance of the solvent-based samples was determined using a four-point probe (RLC 200, Grundig, Germany). From the measured electrical resistance *R* and geometrical data, the electrical conductivity was calculated as:

$$\kappa = \frac{d_{probes}}{R \times w_{coating} \times t_{coating}} \tag{3}$$

with d_{probes} the distance of the voltage probes (12.35 mm), $w_{coating}$ the width and $t_{coating}$ the thickness of the mold for the solvent-based system or the coating for the dry systems.

The dry samples were prepared as follows. The Ag-filled polymer solution samples were first re-mixed in the SpeedMixer at 1,700 rpm for 90 seconds as well. Glass slides (76x52x1 mm, Paul Marienfeld GmbH & Co. KG, Lauda-Königshofen, Germany) were divided into three longitudinal sections using four heat-resistant adhesive strips (Like Sun GmbH, Essen, Germany). Four strips were applied parallel to the long side of the slide, followed by a second layer of adhesive strips placed directly on top. An additional strip was applied along each short edge. Prior to applying the polymer solution, the glass slide surface was cleaned with ethanol and dried. The polymer solution was then placed on each of the three sections with a spatula and spread evenly using another glass slide to achieve a smooth layer. The prepared slides were immediately placed on a hot plate at 130 °C for 5 minutes to evaporate the solvent. Once dried, the adhesive strips were carefully removed, and the geometry (length l, thickness t, width w) of every specimen was determined precisely using an outside micrometer screw with precision of 0.001 mm. To ensure representative geometrical data, the thickness and width of each stripe were measured at three different positions.

Afterward, the electrical conductivity was determined as previously described. Dry Polymer films containing no-iodine underwent an additional heat treatment after the procedure mentioned above for one hour at 240 °C to improve the conductivity.

The percolation threshold φ_c for systems with and without iodine was determined by fitting a power-law equation to the conductivity versus Ag volume fraction data, as described below [131]:

$$\kappa = \kappa_0(\varphi - \varphi_c)^s \quad (4)$$

Here, κ represents the electrical conductivity of the composite, φ is the volume fraction of Ag particles, φ_c is the percolation threshold volume fraction, s is the critical exponent, and κ_0 is a prefactor.

4.2.11 Light microscopy observation

An optical microscope (Keyence VHX-6000, Keyence Corporation, Japan) was utilized to visualize optical changes of the Ag-filled polymer solutions, due to the added iodine salts.

4.2.12 Scanning electron microscopy (SEM)

The Ag particles and the morphology of the cross-section of the Ag-filled adhesives were imaged using scanning electron microscopy (SEM) (S-4500; Hitachi High-Technologies Europe GmbH, Krefeld, Germany).

4.2.13 Adhesive preparation for SEM

A small piece of the dried Ag-filled adhesive was placed in a silicone mold, which was then filled with epoxy resin (ERL-4221D, Serva, Heidelberg, Germany) and cured in an oven at 75 °C for 12 hours. Once fully cured, the resin was removed from the mold. The samples were then ground and polished using the EcoMet 30 grinding machine (Buehler-ITW Test & Measurement GmbH, Leinfelden-Echterdingen, Germany).

4.3 Results and discussion

4.3.1 Influence of iodine on the silver particles

While the influence of various halide compounds - such as pure KI, KBr, and iodine - on Ag particle surfaces has been explored previously [35, 108, 132], we replicate some of these experiments to gain a clear understanding of how all the iodine compounds used here (IL, KI, NaI) affect the Ag particle surface before progressing to Ag-filled polymer solutions and corresponding ECAs obtained after solvent removal. Figure 11 presents scanning electron microscope (SEM) images of Ag particles following iodine treatment. The particles shown in Figure 11a) serve as the reference, having been washed solely with ethanol. The reference particles display a smooth surface, whereas those treated with iodine compounds IL, KI, and NaI exhibit a rough, textured surface, in line with previous observations for Ag particles treated with KI and KBr [35]. Potential changes in chemical surface composition, however, are below the detection limit of energy-dispersive X-ray spectroscopy (EDX).

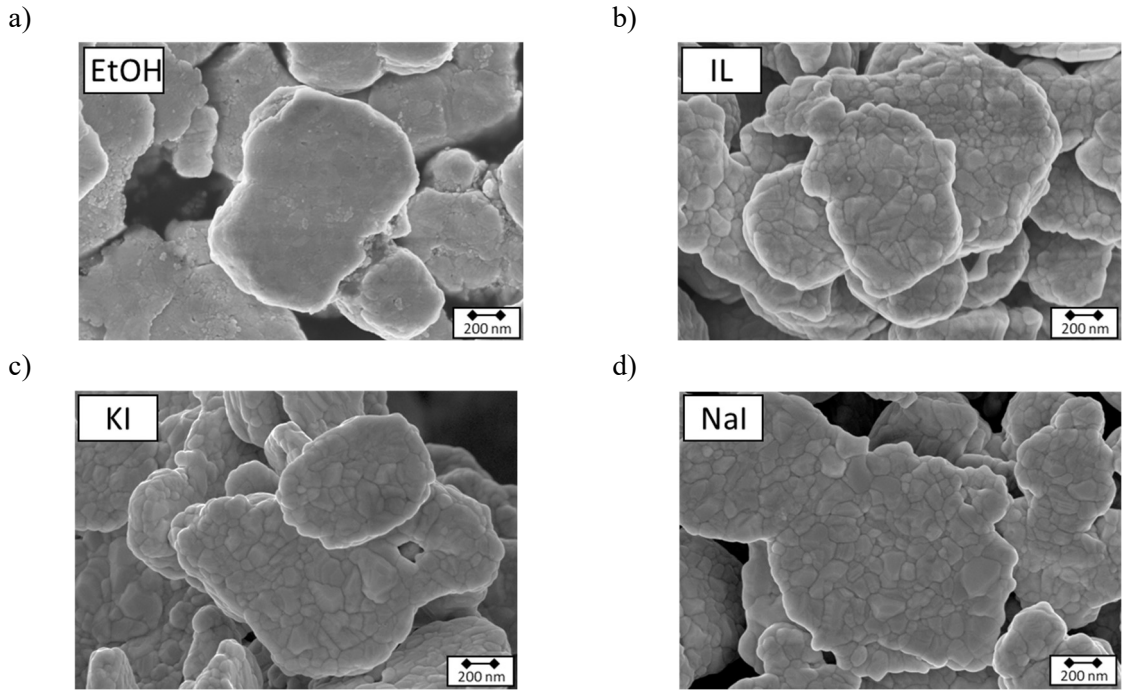

Figure 11 SEM images of Ag particles: a) control sample of particles washed with ethanol, and particles washed with ethanol containing b) IL, c) KI, and d) NaI.

Further insights into the change in particle surface due to iodine treatment are provided by thermogravimetric analysis (TGA), differential scanning calorimetry (DSC) and infrared spectroscopy (IR). TGA results in Figure 12a) reveal that particles treated with IL, KI, and NaI lose approximately 0.85 wt% of their total mass, with the major weight loss occurring between 250 and 350 °C. In contrast, particles washed only with ethanol lose approximately 0.98 wt%. One major loss of approximately 0.6 wt% was observed between 150 and 230 °C, followed by an additional loss of approximately 0.34 wt% between 230 and 300 °C. The TGA results for all particles are shown in Table 4 of the supporting information (SI).

To further validate the TGA results, DSC measurements were conducted for all samples, with the corresponding data shown in Figure 43 and Figure 44 of the SI. Untreated particles exhibited an exothermic peak between 120 °C and 200 °C, followed by an endothermic peak between 240 °C and 250 °C. In contrast, particles treated with IL, KI, and NaI showed only a single endothermic peak around 300 °C. No thermal events were observed in a second heating cycle for any of the samples. The initial weight loss and the exothermic peak observed for the untreated particles are likely associated with the decomposition of organic lubricants such as stearic and isostearic acids, which typically degrade between 200 °C and 300 °C [105]. Although the specific components used in the Ag coating process remain unknown, the results are consistent with previous reports [133]. Furthermore, the weight loss observed in TGA and the endothermic peak detected by DSC at approximately 245 °C for untreated particles might correspond to the decomposition of silver oxide, although silver oxide has been reported to decompose between 280 °C and 340 °C [35, 133, 134]. It is also possible that the observed reaction is due to residual lubricants. However, since the exact composition of the Ag particle coating is unknown, the precise cause cannot be determined unequivocally.

The weight loss and endothermic peak observed around 300 °C in the IL-, KI-, and NaI-treated samples likely correspond to the thermal decomposition of residual silver oxide, as this temperature falls within the reported decomposition range of 280 °C to 340 °C [35, 133, 134]. No exothermic peaks at lower temperatures were observed for the iodine treated particles. These findings suggest that, for iodine-

treated particles, surface-bound carboxylate groups are likely removed by the salts, as proposed in earlier studies [35, 108, 132].

IR spectroscopy results (Figure 12b) offer additional insights. All particles exhibit a similar spectrum in the wavenumber range between 700 and 1800 cm^{-1}. Untreated particles, however, display a prominent band between 1380 and 1420 cm^{-1}, which can be attributed to the symmetric stretching vibration of carboxylates [108, 135]. This band is absent in the spectra of iodine-treated particles, supporting the hypothesis that iodine displaces fatty acids from particle surfaces. These findings are consistent with previous studies using Raman and X-ray photoelectron spectroscopy (XPS) to show that iodine ions replace fatty acids on Ag particle surfaces when treated with various iodine salts, including KI [35, 108].

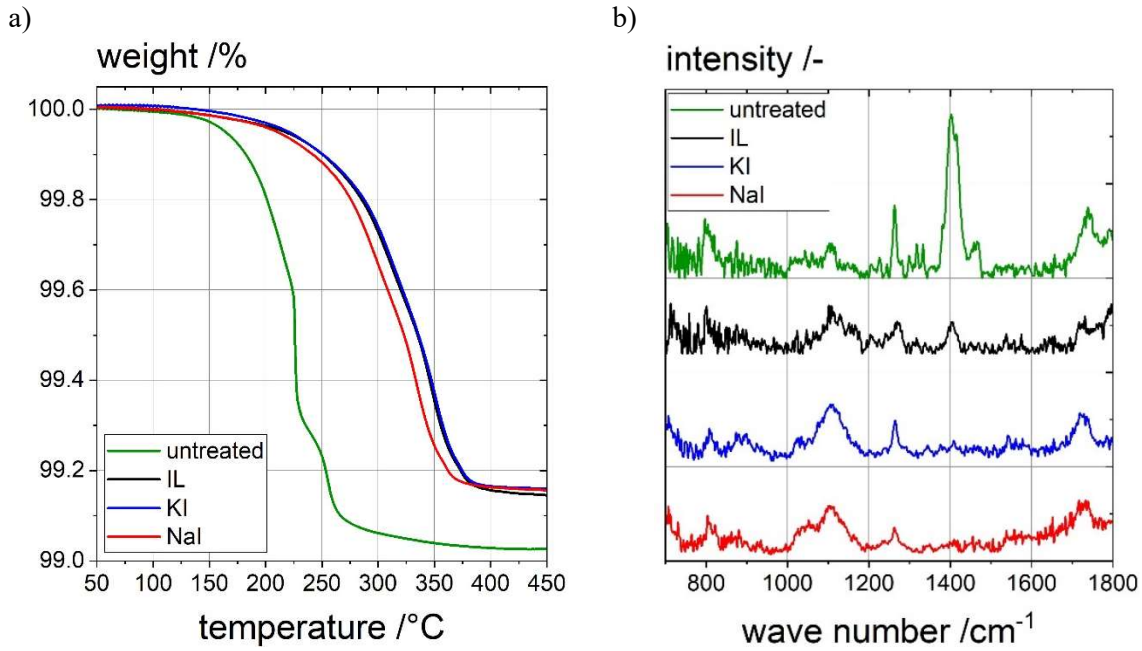

Figure 12 a) TGA and b) IR spectroscopy of silver particles washed with pure ethanol (green) and ethanol containing IL (black), KI (blue), and NaI (red) at a concentration of 2.0 $mmol_{Iodine}/cm^3_{Ag}$

Interestingly, IL - a liquid salt at room temperature - has been previously used as a secondary liquid in Ag particle-based capillary suspensions to lower the percolation threshold and enhance both the electrical and thermal conductivity of epoxy-based adhesives[2, 107, 132]. Although it was clearly demonstrated that IL forms capillary bridges between Ag particles, the ECAs exhibited a color change from shiny silver to a grey-brown tone. This color shift suggests that the iodine ions in the IL may have reacted with the Ag surface, forming AgI. The color shift is similarly evident when comparing the untreated and iodine-treated Ag powders shown in Figure 45 of the SI. Furthermore, the color change of the particles was analyzed using ultraviolet-visible (UV-Vis) spectroscopy, with the results presented in Figure 46 of the SI. A clear change in the UV-Vis spectrum was observed between untreated and iodine-treated particles, consistent with findings reported in the literature [35]. Overall, the results suggest that IL, KI, and NaI can effectively replace the silver carboxylate on the surface of Ag particles, leading to the formation of AgI. The substitution mechanism of carboxylates by iodine anions, illustrated in Figure 13 has also been proposed in previous studies [6, 35].

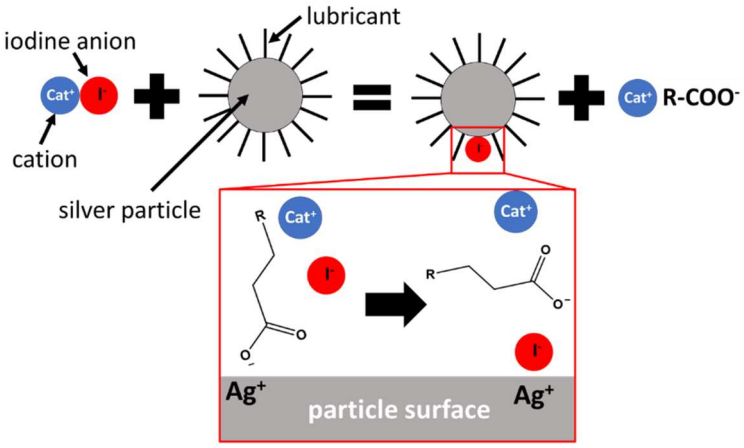

Figure 13 The mechanism of substituting silver carboxylates (lubricants) with iodine anions on the surface of Ag particles [6]. Reproduced from reference [6]. Available under a CC-BY 4.0 license. Copyright 2025 Marten et. al.

4.3.2 Influence of iodine on the rheology of Ag-filled polymer solutions

After establishing that all three iodine salts alter the Ag particle surface, we now examine the effect of adding these iodine salts directly to Ag-filled solutions TPU in the organic solvent dimethyl sulfoxide (DMSO). Figure 14a) shows the yield stress for this polymer solution containing 5.7 vol% Ag as a function of iodine concentration. Here, the salt concentration is always given normalized to the volume of Ag present in the TPU/DMSO solution as described in the experimental section. At salt concentrations up to 0.167 $mmol_{Iodine}/cm^3_{Ag}$, these solutions freely flow and do not exhibit a yield stress. Exceeding a critical concentration, however, results in a strong change in texture, showing up in a yield stress of about 10 – 15 Pa at a salt concentration of 0.333 $mmol_{Iodine}/cm^3_{Ag}$. The yield stress further increases with increasing iodine concentration and at the highest concentration of 3.1 $mmol_{Iodine}/cm^3_{Ag}$, yield stress values in the range of 40 to 50 Pa are found.
Figure 14b) shows the electrical conductivity of the same formulations. At low iodine concentrations (< 0.111 $mmol_{Iodine}/cm^3_{Ag}$), the electrical conductivity in all three cases remains around or below 10^{-5} S/cm. As the iodine concentration increases, a sharp rise in conductivity is observed, eventually approaching plateau values of approximately 50, 27 and 37 S/cm for IL, KI and NaI at 3.1 $mmol_{Iodine}/cm^3_{Ag}$, respectively. Interestingly, both yield stress and electrical conductivity exhibit similar trends: a steep increase in the range of 0.0 to 0.5 $mmol_{Iodine}/cm^3_{Ag}$, followed by a gradual leveling off toward a plateau at higher iodine concentrations. However, electrical conductivity starts increasing at slightly lower concentrations (0.111-0.167 $mmol_{Iodine}/cm^3_{Ag}$) than the yield stress (0.222-0.333 $mmol_{Iodine}/cm^3_{Ag}$). This difference might be explained by the higher sensitivity of the electrical conductivity measurement.

Nevertheless, a strong correlation between yield stress and electrical conductivity can be observed. Figure 48 of the SI shows an almost linear correlation between yield stress and electrical conductivity for the three salts. Additionally, since both yield stress and electrical conductivity appear to plateau - showing no significant change between iodine concentrations of 2.0 and 3.1 $mmol_{Iodine}/cm^3_{Ag}$ - it can be inferred that, beyond a certain iodine concentration, the system's properties remain stable in terms of electrical conductivity and yield stress. This observation holds true, at least within the concentration range studied here.

Previous studies have established a correlation between iodine concentration, the removal of lubricants from the Ag particle surface, and the resulting improvement in electrical conductivity [35, 108]. This enhancement in conductivity was attributed to the smaller cell constant of AgI (6.495 Å) [136] compared

to that of long-chain fatty acids such as stearic acid (27 Å) [137], which facilitates more efficient electron tunneling between Ag particles [35]. As shown in Figure 14a) and b), replacing fatty acids with iodine also induces structural changes in the formulation. This is likely due to the role of fatty acid-based lubricants in improving the dispersibility of Ag particles in organic composites [105]. Their removal likely initiates agglomeration of AG particles, causing microstructural changes that increase the yield stress. The similarities between changes in yield stress and electrical conductivity also suggest that these microstructural changes increase the conductivity as well. Once all surface-bound lubricants are removed, further increases in iodine concentration have no additional effect on structure or electrical conductivity and thus both yield stress and electrical conductivity seem to plateau eventually. It is worth noting that the highest normalized iodine concentration used in this study (3.1 $mmol_{Iodine}/cm^3_{Ag}$) is more than an order of magnitude higher than those reported in the literature (0.021–0.105 $mmol_{Iodine}/cm^3_{Ag}$) [35, 132]. This was done to investigate whether excessive iodine levels could negatively impact conductivity - however, no such degrading effect was observed up to this concentration.

The texture transformation by adding iodine to the TPU/DMSO solution can be seen by visual inspection, as shown in Figure 14c). For each salt, the Ag-filled solutions exhibit fluid-like behavior when no or only small concentrations of salt are added, above a critical salt concentration a paste-like texture is observed. Additionally, the color shifts subtly, changing from a grey-silver to a brownish tone, similar to the particles shown in Figure 45.

Previously it was reported that the percolation threshold could be shifted to lower particle loading and the conductivity could be increased in silver-filled epoxy and TPU composites by adding IL. This was attributed to the formation of a capillary suspension network [3, 107]. However, in the present case, IL as well as KI, NaI are dissolved directly in DMSO, and these solutions are fully miscible with the TPU/DMSO system (Figure 47). Thus, capillary bridges cannot form and therefore, a different mechanism must be responsible for the observed changes in flow behavior and electrical conductivity of the wet paste.

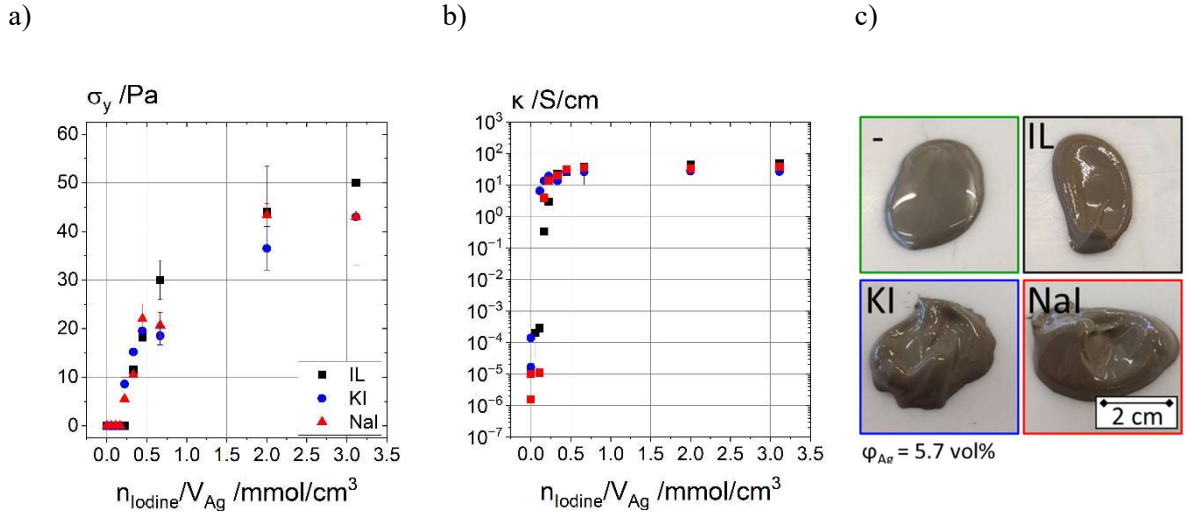

Figure 14 a) The yield stress σ_y and b) the electrical conductivity κ plotted against the normalized iodine concentration for polymer solutions containing 5.7 vol% Ag and different concentrations of IL (black squares), KI (blue circles), NaI (red triangles). c) Images of the polymer solutions containing no iodine (green) and a normalized iodine concentration of 2.0 $mmol_{Iodine}/cm^3_{Ag}$ of IL (black), KI (blue) and NaI (red), respectively.

Figure 49 further illustrates how yield stress varies with Ag concentration at a fixed iodine concentration of 2.0 $mmol_{Iodine}/cm^3_{Ag}$, demonstrating that all iodine salts produce a similar increase in yield stress, and that even at an Ag particle fraction as low as 3.2 vol% adding iodine alters texture and flow substantially. Furthermore,

Figure 51, Figure 52 and Figure 52 display the amplitude and frequency sweeps of the systems with a normalized iodine concentration of 2.0 $mmol_{Iodine}/cm^3_{Ag}$ for the different iodine compounds. Further confirming the change in texture, the yield stress values deduced from the onset of non-linear response in the amplitude sweeps are in fair agreement with the yield stress values obtained from shear stress ramps.

Examining the flow curves of the Ag-filled TPU/DMSO solutions in Figure 15 provides additional insights. The pure TPU/DMSO solution exhibits Newtonian behavior, with a viscosity of approximately 4.6 Pa·s. Adding 3.2 vol% Ag particles increases the viscosity to around 9.5 Pa·s, and the suspension still exhibits almost Newtonian flow behavior as expected for stable suspensions of non-Brownian, flake-shaped particles, when attractive forces among particles can be neglected [138]. The behavior changes significantly when iodine salt is added. The suspensions with 2.0 $mmol_{Iodine}/cm^3_{Ag}$ added salt clearly exhibit strong shear-thinning behavior with maximum viscosities of 52.1, 27.6, and 22.9 Pa·s at a shear rate of approximately 2 s^{-1} for IL, KI, and NaI, respectively.

The fact that a yield stress and strong shear-thinning behavior occur upon adding iodine salts clearly indicates the formation of a percolating particle network within the TPU/DMSO solution which is further supported by the increase in electrical conductivity. Such behavior was reported earlier [3, 107] and must be due to strong attractive particle interactions. In earlier work this was attributed to capillary forces, here we must assume that prevailing van der Waals forces control the network formation, since the added iodine salt solutions are fully miscible with the bulk polymer component. Attractive van der Waals interactions among particles start to dominate when the organic surface layer is partly removed, as discussed above (Figure 13). Accordingly, after removal of the organic lubricants from the particle surface, the particles start agglomerating which changes the microstructure evident in the texture (yield stress) and electrical conductivity changes (Figure 14).

At higher shear rates (Figure 15), this microstructure breaks down, leading to a decrease in viscosity, ultimately leveling at a high shear limiting value solely determined by the particle volume fraction and shape, but higher than that of the suspension's continuous phase [139]. Notably, the viscosities of iodine salt-containing suspensions are lower than that of the pure TPU/DMSO solution. This reduction is due to the addition of iodine compounds as DMSO solutions, as described in the experimental section, which slightly dilutes the TPU/DMSO solution and alters the solvent quality resulting in a lower viscosity of 2 to 2.5 Pa·s for the continuous phase. This effect is less pronounced for IL than for KI and NaI, since the added IL-DMSO solution is higher concentrated (19.86 $vol\%_{IL}$) than the KI- (3.77 $vol\%_{KI}$) and NaI-DMSO solutions (3.22 $vol\%_{NaI}$). The TPU/DMSO solution containing an equivalent amount of Iodine/DMSO solution, but without Ag particles, is also plotted to demonstrate that the reduction in viscosity is solely attributed to dilution. Since these mixtures continue to exhibit Newtonian behavior, it can be inferred that iodine compounds do not influence the microstructure of the pure TPU/DMSO solution. The relative high shear viscosity of the Ag-filled systems, i.e. the viscosity of the filled system divided by the viscosity of the TPU solution, is the same irrespective of the type of the added salt and falls in a typical range for suspensions of non-Brownian anisotropic particles, indicating that the particles are well-dispersed and there is no specific interaction among iodine salts and the TPU/DMSO solution.

Previously, adding short-chain organic acids to Ag-filled ECAs has been shown to alter viscosity [105]. The impact of iodine salts on yield stress formation and textural changes, however, is demonstrated here for the first time. Thus, when iodine compounds are incorporated into an Ag-filled formulation, it is important to consider that the rheological characteristics may change from predominantly viscous to viscoelastic, paste- or gel-like behavior.

This phenomenon presents a cost-effective and straightforward approach not only to slow down sedimentation and enhance the shelf-life of such formulations, but also to adjust the flow behavior according to the demands of different processing or application methods. The results of a sedimentation experiment are displayed in Figure 53 of the SI. A distinct difference in sedimentation between the iodine and non-iodine containing systems is clearly visible. While sedimentation is obvious for the system without iodine, the samples containing iodine appeared stable even after 24 days of storage, regardless of the specific compound.

Furthermore, it is expected that the structural changes observed in the wet system may propagate in the dry films. This will be discussed in the subsequent chapters.

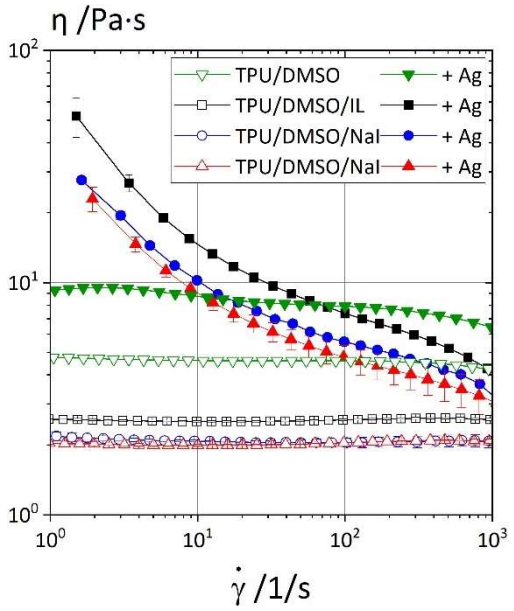

Figure 15 The viscosity η plotted against the shear rate $\dot{\gamma}$, for the pure TPU/DMSO solution (green inverted open triangles), TPU/DMSO solution containing 3.2 vol% Ag (green inverted triangles), and TPU/DMSO solutions additionally containing an iodine concentration normalized to the volume of added silver of 2.0 $mmol_{Iodine}/cm^3_{Ag}$: IL (black squares), KI (blue circles), and NaI (red triangles). Note, for the samples with added iodine salt, all viscosity data shown here correspond to shear stresses $\sigma > \sigma_y$. Additionally, the viscosities of TPU/DMSO solutions containing the same iodine concentration (2.0 $mmol_{Iodine}/cm^3_{Ag}$) but without silver particles are plotted for IL (black open squares), KI (blue open circles), and NaI (red open triangles), respectively.

4.3.3 Influence of iodine on the electrical conductivity

We now discuss the effect of iodine salts on the electrical conductivity in the dry composite films. Figure 16 presents the electrical conductivities of Ag-TPU composite films after solvent removal. The films contain 20 vol% Ag particles and conductivity is shown as a function of salt concentration normalized to the volume of added Ag for three different iodine salts. The films were made from the solutions for which the yield stress and electrical conductivity data are shown in Figure 14. The Ag particle volume fraction increases from 5.7 vol% before solvent removal to 20 vol% in the dry film.

Conductivity data across the three iodine salts reveal similar trends as salt concentration increases, categorized into three distinct regimes.

In the first regime, with low or no iodine salt, conductivity is minimal, around 10^{-5} S/cm. Notably, due to the linear scale of the plot, normalized iodine concentrations as low as $5.0 \cdot 10^{-5}$ $mmol_{Iodine}/cm^3_{Ag}$ and low electrical conductivities (10^{-5} S/cm) appear indistinguishable from zero. In the second regime, intermediate normalized iodine concentrations yield maximum conductivities of approximately 2,650, 2,600, and 2,800 S/cm for IL, KI, and NaI, respectively at a normalized concentration of approximately 0.056 $mmol_{Iodine}/cm^3_{Ag}$. The third regime, with normalized iodine concentrations between 0.2 and 3.1 $mmol_{Iodine}/cm^3_{Ag}$ exhibits a pronounced decrease of conductivity reaching values between 450 and 650 S/cm at the highest normalized iodine concentration of 3.1 $mmol_{Iodine}/cm^3_{Ag}$.

Comparing the electrical conductivity data (Figure 14b) of the wet Ag-filled TPU/DMSO solutions with the conductivity data for the dry films reveals that in the latter case electrical conductivity peaks at 0.056 $mmol_{Iodine}/cm^3_{Ag}$, while for the wet, solvent-based systems conductivity increases until it finally levels off at a normalized iodine concentration of about 0.5 $mmol_{Iodine}/cm^3_{Ag}$. This may be explained by differences in the total iodine concentration between the TPU/DMSO solutions and the corresponding dry films. The TPU/DMSO solution contains approximately 70 vol% solvent, which significantly reduces its total iodine concentration at a given iodine-to-silver ratio compared to the solvent-free composites. Consequently, the likelihood of iodine anions encountering the Ag particle surface to replace the lubricants is lower. As a result, the effect of iodine addition becomes noticeable at higher iodine-silver ratios in the solution.

Another interesting aspect observed here is that conductivity peaks and then declines at higher normalized iodine concentrations. This trend was not seen when investigating the solvent-based system in Figure 14b) where electrical conductivity reaches a plateau with increasing iodine concentration, nor in prior studies showing a monotonic increase in composite conductivity when Ag particles were treated with increasing amounts of KI ranging from 0.021 to 0.105 $mmol_{Iodine}/cm^3_{Ag}$ [35, 132]. Here (Figure 16), the conductivity maximum occurs at around 0.056 $mmol_{Iodine}/cm^3_{Ag}$. The normalized iodine concentration at which conductivity begins to decline is presumably affected by the total surface area of Ag particles, which depends on their size distribution and shape. As a result, this decline may have been masked in these previous studies but would likely become evident if normalized iodine concentration had been increased further.

However, similar behavior to that observed here has also been observed in other studies. For instance, Ag particles treated with various ratios of terephthalaldehyde (TPTA) to replace fatty acids on the Ag particle surface and iodine (I_2) to reduce silver oxide showed maximum conductivity when the balance between silver oxide reduction and fatty acid replacement was optimal[108]. Another study proposed that KI treatment of Ag particles leads to AgI/Ag nano particle formation on the micro particle surface, which can reduce the formation of silver oxides and hence increases the conductivity of ECAs after curing. However, an excessive AgI/Ag nano particle formation, as seen with high iodine concentration-treatment led to a reduction in conductivity again [140].

Similar trends were also observed in a study using IL as a secondary liquid in capillary suspensions to increase the thermal conductivity of cured Ag/epoxy composites, as well as the yield stress of the uncured precursors. In this study the increase in conductivity was attributed to the structural transition from uniformly distributed Ag particles in the polymer matrix to the formation of a percolating Ag particle network due to capillary forces induced by adding trace amounts of IL as secondary liquid [107].

While assuming the formation of a particle network driven by capillary forces may explain the effect of IL added to Ag/epoxy composites, it does not account for the distinct changes in yield stress, electrical conductivity, or viscosity of the TPU/DMSO solutions used here (Figure 14 and Figure 15) and the change in conductivity of the corresponding dry films (Figure 16). All salts used in this study are fully miscible with the polymer solution, as demonstrated in Figure 47 of the SI. Consequently, capillary forces that might otherwise influence rheological behavior do not arise in this solvent-based system. In the resulting dry films, IL might remain in the liquid state between Ag particles, whereas NaI and KI – which are solids at room temperature - do not. However, since all three iodine-containing compounds produce similar results, the observed changes in rheology and electrical conductivity are likely driven by a different mechanism that alters the microstructure, i.e. particle aggregation and network formation, in the wet paste and dry film, respectively.

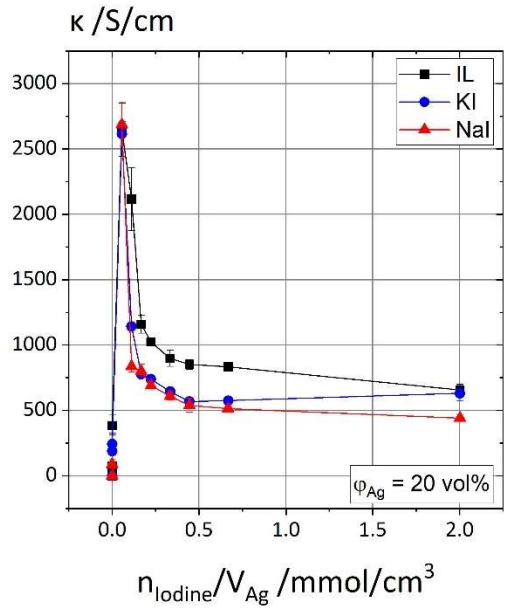

Figure 16 a) The electrical conductivity κ (S/cm) of dry Ag/TPU composite films containing 20 vol% Ag, plotted against normalized iodine salt concentration n_{Iodine}/V_{Ag} (mmol/cm^3): IL (black squares), KI (blue circles) and NaI (red triangles). b) The electrical conductivity κ (S/cm) of dry films with a normalized iodine concentration of 0.056 $mmol_{Iodine}/cm^3_{Ag}$ and different Ag volume fractions.

Figure 54 in the SI further demonstrates that dry TPU samples containing 20 vol% Ag and 0.056 $mmol_{Iodine}/cm^3_{Ag}$ retained their electrical conductivity after being stored at 60 °C for approximately one month. Consistent with this observation, literature reports also indicate that adding IL does not negatively impact electrical conductivity, even after six months of storage at ambient conditions or under damp-heat testing at 85 °C and 85 % relative humidity [2, 6].

Figure 17 further illustrates the influence of different iodine compounds on electrical conductivity. Here, the conductivity of samples with an iodine concentration of 0.056 $mmol_{Iodine}/cm^3_{Ag}$ (regime 2) is plotted as a function of the Ag volume fraction. For comparison, data for iodine-free samples (shown in green) are also included. Power-law fits[131], indicate that the addition of iodine reduces the percolation threshold φ_c from approximately 24.0 vol% in regime 1 to about 5.0 vol% in regime 2, in agreement with previous studies on IL-based conductive composite formulations [2]. This indicates that even at low Ag loadings (as low as 6 vol%), all iodine salts significantly enhance the electrical conductivity of the Ag/TPU composite films.

This enhancement is likely not solely correlated to the reduced contact resistance between Ag particles by the removal of fatty acids, the reduction of silver oxide, or the formation of Ag nanoparticles, as previously reported [35, 108, 140]. However, a significant contributing factor appears to be the development of a percolated silver particle network, as indicated by the observed changes in rheological behavior and electrical conductivity in the solvent-based systems (Figure 14) and the drastically lower percolation threshold of the samples containing iodine in Figure 17. Additionally, no systematic dependence on the specific iodine compound used was observed.

These results underscore the type-independent, efficient improvement in the conductivity of polymer composites with low silver content through the addition of iodine compounds. The correlation between rheological behavior, microstructure, and electrical conductivity observed in the wet, solvent-based system, further motivates a direct analysis of the solvent-free composite microstructure to provide further insights regarding the reason for the conductivity increase.

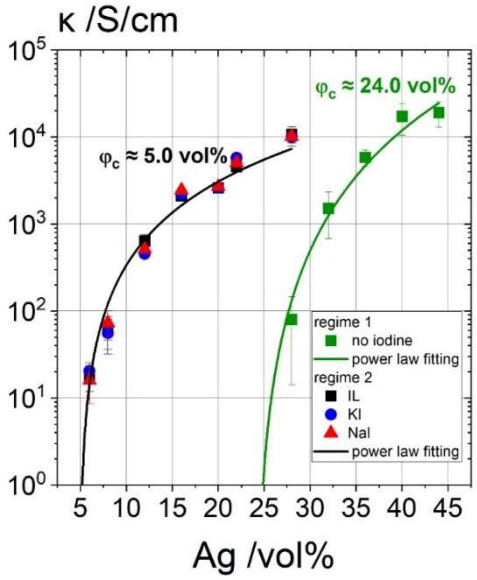

Figure 17 The electrical conductivity κ of dry films with no iodine (green, regime1) and a normalized iodine concentration of 0.056 $mmol_{Iodine}/cm^3_{Ag}$ (regime 2) plotted against the Ag volume fraction. The black and green line are power law fits to determine the percolation threshold [131].

4.3.4 Influence of iodine on the microstructure

Iodine ions from salts such as IL, KI, and NaI can remove silver carboxylates (lubricants) from Ag particles (Figure 12) and can form AgI on Ag particle surfaces [35, 108]. They can also induce a yield stress (Figure 14a), improve the electrical conductivity (Figure 14b), increase the viscosity and induce strong shear-thinning (Figure 15) when Ag particles are suspended in TPU/DMSO solutions. They can furthermore significantly enhance the electrical conductivity and drastically lower the percolation threshold of dry Ag/polymer composites (Figure 17). Next, the effect of added iodine salts on the microstructure of the dry Ag/TPU composites will be discussed.

Figure 18a) shows SEM images of cross-sections of Ag-filled (20 vol%) TPU films for different normalized IL concentrations. These images correspond to the three electrical conductivity regimes discussed above (Figure 16):

Regime 1 **- No iodine**: Particles are uniformly distributed throughout the sample, with few particle-to-particle contacts, resulting in low bulk conductivity.

Regime 2 - Intermediate normalized iodine concentration: Electrical conductivity is high, and the sample appears heterogeneous on the microscopic level. Areas with locally high Ag concentration and Ag-free regions are observed, indicating partial aggregation.

Regime 3 - High normalized IL concentration: Conductivity decreases again, with even more pronounced heterogeneity. Large Ag agglomerates and Ag-free regions are visible, suggesting increased aggregation.

A similar behavior has been reported for systems where IL was used as a secondary fluid in capillary suspensions [107]. Nevertheless, we propose an alternative mechanism to explain the structural transitions, as the rheological behavior of Ag-filled TPU/DMSO solutions and the decrease in the percolation threshold clearly indicate that the presence of iodine salts alters the particle microstructure even if the salts are solid at room temperature or miscible with the precursor for the dry Ag/TPU composites. Without added iodine, the lubricant layer ensures uniform particle distribution with no or only few direct particle contacts, resulting in low conductivity (Figure 18, left), since the particle volume fraction is below the percolation threshold of approximately 24.0 vol% as presented in Figure 17.

According to the mechanism shown in Figure 13, added iodine salts can remove lubricants from the Ag particle surface [35, 108], i.e. silver carboxylates are partly replaced with iodine ions. This reduces the steric repulsion among particles as well as the compatibility between the Ag particles and the organic matrix, thus lowering their dispersibility in the TPU/DMSO solution.

Accordingly, van der Waals attraction between the particles prevails, leading to particle aggregation and the formation of a percolating particle network (schematically depicted in Figure 18b, middle), which significantly increases conductivity. However, as normalized iodine concentration increases further, additional carboxylate replacement leads to the formation of large Ag agglomerates, reducing the number of conductive pathways and lowering bulk conductivity again (Figure 18b, right).

Image analysis using the commercial open source software ImageJ [141] was conducted to more precisely investigate the dry film microstructure associated with the three regimes. The analysis approach is described in the SI and Figure 55 and Figure 56 of the SI show the analysis results. These findings align well with the proposed microstructure schematically shown in Figure 18b). A clear transition is observed: from Ag particle regions with minimal interconnection (regime 1), to a highly interconnected, sample-spanning Ag particle network (regime 2), and finally to a less interconnected one (regime 3).

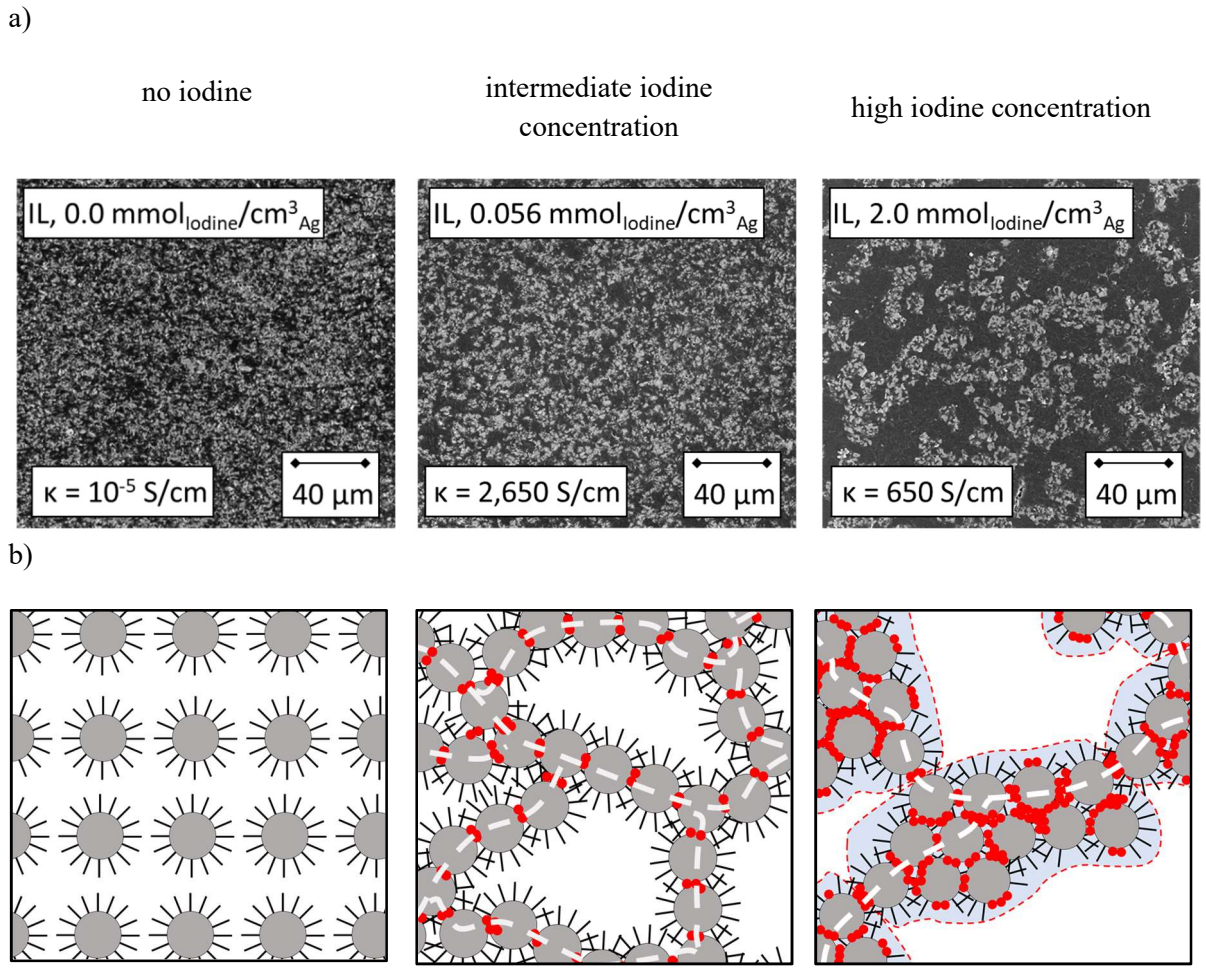

Figure 18 a) SEM images of cross-sections of dry Ag/TPU films containing 20 vol% Ag and varying normalized concentrations of IL. b) The suggested changes in microstructure that iodine ions (red dot) induce in Ag-filled polymer composites[6]. Reproduced from reference [6]. Available under a CC-BY 4.0 license. Copyright 2025 Marten et. al.

In the dry IL system capillary forces may additionally promote particle aggregation and network formation [107]. For the KI and NaI systems this is, however, not possible, since the added KI or NaI are solid at room temperature. Furthermore, all three types of iodine compounds are miscible with the solvent-based system and therefore the formation of capillary bridges is impossible.

Figure 19 illustrates the structural changes in a polymer composite filled with 20 vol% Ag and varying normalized concentrations of KI and NaI. Samples with an intermediate normalized iodine concentration of 0.056 mmol$_{Iodine}$/cm$^3_{Ag}$ (Figure 19, left column) show a partially aggregated structure featuring multiple conductive pathways, for both added iodine salts similar as for added IL (see Figure 18). This structural configuration seems to be decisive for the high electrical conductivity. In contrast, formulations with a high normalized iodine concentration of 2.0 mmol$_{Iodine}$/cm$^3_{Ag}$ (Figure 19, right column) exhibit stronger particle aggregation and phase separation probably resulting in fewer conductive pathways throughout the sample, and hence a lower electrical conductivity, similar for all added iodine salts. Since KI and NaI do not remain as liquids within the dry polymer composite they cannot induce capillary forces, the structural changes in the composite are likely due to the removal of lubricating agents, which in turn alters the dispersibility of the particles as described in Figure 13.

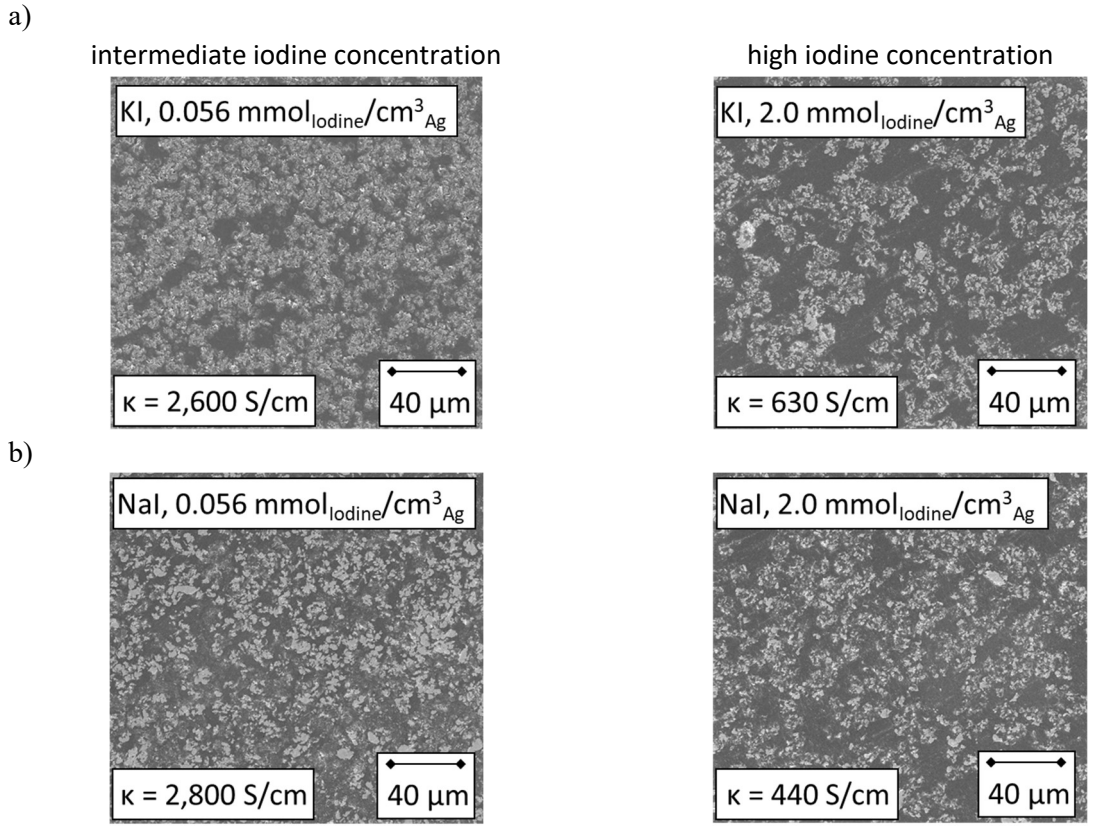

Figure 19. SEM images of cross-sections of dry Ag/TPU composite films containing 20 vol% Ag as well as a) KI, and b) NaI with n = 0.056 mmol$_{Iodine}$/cm^3 (left column) and n = 2.0 mmol$_{Iodine}$/cm$^3_{Ag}$ (right column).

In addition to the known effects of iodine treatment - such as the removal of insulating lubricant layers, reduction of silver oxides, UV-induced formation of Ag nanoparticles, and enhanced oxidation stability through the creation of Ag/AgI nanoparticles on the Ag surface [35, 108, 140] - these results offer new insights into the fundamental impact of iodine salts on structure formation in Ag-filled TPU/DMSO solutions as well as corresponding dry composite films. The related effects on flow behavior of the solutions are relevant for shelf life, processing and application behavior, and the impact on the electrical conductivity of dry composite films is decisive for their application behavior.

4.4 Conclusion

This study provides an in-depth investigation into the effects of iodine salts on the microstructure and functional properties of dry Ag-filled polymer films, as well as the flow behavior of the corresponding precursor suspensions of Ag particles in TPU/DMSO solutions, while also proposing a streamlined production approach for these materials.

Iodine salts such as IL, NaI, and KI were added to Ag-filled polymer composites using a 24.1 vol% solution of the thermoplastic adhesive TPU Elastollan Hotbond AH 530 in DMSO. The amount of Ag particles and the added iodine salt was varied systematically. We evaluated the yield stress, viscosity and electrical conductivity of the Ag-filled TPU/DMSO solutions, as well as the electrical conductivity and microstructure of the corresponding dry films after solvent removal. SEM imaging, TGA, DSC and IR spectroscopy were employed to analyze the impact of IL, KI, and NaI on the surface morphology and chemical composition of individual Ag particles.

In line with literature data on similar systems [35], TGA, DSC and IR spectroscopy confirmed that a treatment of Ag particles with IL, KI, and NaI effectively removed lubricants from the particle surface.

The addition of IL, KI, and NaI to the Ag-filled TPU/DMSO solutions resulted in substantial change in flow characteristics from pre-dominantly viscous to strongly viscoelastic with a gel-like or pasty texture, showing up as a yield stress σ_y and a pronounced shear-thinning behavior at stresses $\sigma > \sigma_y$. This change in flow characteristics occurred irrespective of the type of added iodine salt and no significant, systematic variation with respect to the chemical composition of the salt was found. The observed change in rheological behavior clearly indicates the formation of a percolating particle network within the respective TPU/DMSO solutions, and is attributed to prevailing attractive van der Waals interactions among particles when the organic surface layer is partly removed. The formation of capillary suspensions as proposed earlier for Ag-filled TPU solutions with IL added as aqueous solution [2, 107] can be excluded, since KI, NaI, and IL are added as solutions in DMSO here, and these solutions are fully miscible with the TPU/DMSO solution. The change in texture due to adding a small amount of iodine salt presents a cost-effective and straightforward approach not only to slow down sedimentation and enhancing the shelf-life of such formulations, but also to adapting their flow behavior over a wide range according to the demands of different processing or application methods.

The electrical conductivity of the dry Ag/TPU composite films obtained from the suspensions discussed above also showed a strong dependency on normalized iodine concentration, and again no systematic variation with the type of added salt (IL, KI, or NaI). Three distinct regimes were found: Low normalized iodine concentration resulted in low conductivity (~10^{-5} S/cm), at intermediate normalized iodine concentrations a strong peak in electrical conductivity occurred with conductivities of around 2,700 S/cm for 0.056 $mmol_{Iodine}/cm^3_{Ag}$, finally intermediate conductivities of around 550 S/cm, were found at high normalized iodine concentrations for films including 20 vol% of Ag particles. No loss in electrical conductivity was observed after one month of storage at 60°C.

SEM images of cross-sections of Ag/TPU composites containing 20 vol% Ag and varying IL, KI, and NaI concentrations, corresponding to the three regimes discussed above, reveal that all iodine compounds promote particle aggregation and formation of microheterogeneities. At intermediate normalized iodine concentrations, the aggregates are relatively small. However, at high normalized iodine concentrations, stronger aggregation reduces conductivity due to the lower number of conductive paths. Image analysis revealed that regime 2 exhibits a more interconnected microstructure compared to regimes 1 and 3, which likely accounts for its higher electrical conductivity.

Further enhancement of electrical conductivity toward values typical of conventional solder materials may be achieved by increasing the silver particle loading and employing particles with bi- or trimodal size distributions [142]. Additionally, incorporating silver nanoparticles can promote partial sintering within the silver particle network, further reducing contact resistivity [142, 143].

These findings extend prior studies that employed IL as a secondary liquid in capillary suspensions [107]. Although IL which is liquid at ambient conditions may form capillary bridges between Ag particles, it is more likely that the observed microstructural changes observed here are primarily due to lubricant removal by IL, as similar effects are seen with KI and NaI - solid salts that cannot form capillary bridges.

The results presented here reveal new insights into the essential role of iodine salts in Ag-filled TPU/DMSO solutions as well as dry Ag/polymer composite films made from them. Specifically, iodine salts have a strong effect on microstructure and particle network formation, enabling the control the flow

behavior of Ag-filled polymer solutions as well as the electrical conductivity of corresponding dry films in a controlled manner. Moreover, this study demonstrates that pre-treatment of Ag particles with iodine is not necessary [35, 108, 140]; iodine compounds can be added directly into solution based formulations. This direct addition simplifies production and processing of Ag filled polymer films, reducing time, material usage, and overall cost.

Furthermore, the findings indicate that the mechanism is not limited to specific polymers, solvents, or applications. It can be applied across various fields, including adhesives for solar cell interconnections, the production of electrically conductive nylon yarn, or die attach and flexible electronics [2, 6, 124]. However, considerations regarding cost and environmental impact are essential, as iodine compounds are toxic to aquatic life and require special disposal procedures. Nonetheless, the reduction in silver consumption by 15 -20 % enabled by the addition of the iodine compounds also offers environmental and economic benefits. These trade-offs must be evaluated individually for each use case.

In conclusion, this study offers valuable insights into the use of iodine salts to control microstructure and electrical performance of dry Ag-filled polymer films, but also their wet-route processing properties facilitating advanced applications of Ag-filled polymer materials.

4.5 Acknowledgement

I sincerely thank all the students and coworkers who supported me in my work and contributed to conducting experiments in the laboratory, especially Katharina Kuppinger for conducting TGA measurements. Your dedication and hard work have been pivotal to the success of our projects, and I deeply appreciate your invaluable contributions.

Chapter 5 Electrically conductive yarn for Smart Textiles

Full title: *High-throughput Production of Electrically Conductive Yarn (E-Yarn) for Smart Textiles*

Authors: *Jonas Marten, Nathalie Gaukel, Yunkai Hu, Yiliang Wang, Guangjie Yuan, Norbert Willenbacher*

Status: *published* [124]

Bibliographic data: *Advanced Electronic Materials*, *11*(7), 2400700;
DOI: https://doi.org/10.1002/aelm.202400700

Abstract
Electrically conductive yarn is essential for developing smart textiles, combining advanced functionalities with the desirable mechanical properties of traditional yarn. This study introduces an innovative method for manufacturing Nylon yarn coated with an electrically conductive, thermoplastic polymer layer. The method is based on the classical wire coating process, thus enabling for rapid scale-up. The feasibility of the new approach was demonstrated coating a Nylon yarn 250 µm in diameter with a 20 µm thermoplastic coating layer consisting of a polyamide (Platamid M1276 F, melting temperature 110-120 °C) matrix including 20 vol% silver flakes (d_{50} = 2.5 µm). The resultant resistivity of the coated yarn was about 7.5 Ω/cm, and essentially kept constant even after multiple bending and washing cycles simulating typical stresses during textile utilization. Additionally, the yarn was used to fabricate a pressure sensor, demonstrating a pressure sensitivity range of 1 to 20 kPa, a sensitivity of 10^{-3} kPa^{-1}, and a response time of 224 ms. This study showcases a versatile manufacturing process for electrically conductive yarn suitable for smart textile applications. It emphasizes the potential for integrating these yarns into functional textile systems and highlights the feasibility of using existing industrial-scale coating equipment, thus facilitating rapid market integration.

5.1 Introduction

Smart textiles represent an emerging frontier with immense potential across various domains of next-generation wearable electronics. These versatile materials find utility as pressure sensors for human motion [72], artificial muscles for soft robotics [144], electromagnetic interference shields [145], and serve broader functions as electrical sensors, actuators, supercapacitors, energy harvesters, or displays [2, 146, 147]. Deployment methods include screen-printing or direct ink writing of conductive pastes, and the use of 3D printable electrically conductive filaments directly onto the fabrics [2, 111]. However, a smoother integration of conductivity into the traditional fabric manufacturing process can be realized by directly applying the electrically conductive material to the fiber or yarn. Additionally, this approach ensures that the fabric retains its original mechanical properties, such as elasticity and flexibility [148]. The most common way of manufacturing electrically conductive fabric involves weaving, knitting, or sewing metal wires in addition to conventional yarn [5, 74], while alternative approaches entail applying metal films via techniques like sputtering, electrodeless plating, or screen-printing directly on the yarn [149–151]. Moreover, methods such as dip-coating, spray-coating, or drop-coating enable the application of thin layers of conductive materials like silver (Ag) nano-wires or single-walled carbon nanotubes (CNT) to yarn surfaces, offering an relatively easy to handle process with the ability to adapt to specific product requirements by varying the conductive materials [71, 152, 153].

Although, these methods supply electrically conductive yarn with suitable properties for manufacturing e-textiles, one key factor is overlooked frequently: a high-throughput manufacturing process that can effectively meet the demands of the textile industry. A process that enables to use different kind of raw materials regarding costs and properties, that is easy to handle, energy efficient, and provides flexibility to adapt quickly to a dynamic textile market. To fill this gap, we have developed a versatile alternative to the conventional coating techniques mentioned above, using a polymer solution-based coating process similar to the insulation coating of thin copper wires for use in electromagnetic coils [154]. The similarity to this already well-established coating technique enables a quick scale-up with the possibility of a high-throughput, energy efficient yarn production at an output of up to 800 m/min based on well-established coating equipment. The inks utilized here are formulated akin to those employed in wire coating processes, comprising a polymeric composite dissolved in a compatible solvent, filled with electrically conductive particles. The selected components (solvent, polymer, filler) provide the basis for a modular system that enables different functional layers to be applied to a variety of different yarns or filaments in a stable, efficient and fast-working process and offers the possibility of making rapid changes to the formulation without the need to develop new application methods. To demonstrate the strategy, a polyamide-based coating filled with silver particles was used to apply thin electrically conductive coating layers to a Nylon yarn using a customized laboratory-scale coating machine. Washing and bending tests were employed to demonstrate the durability of the yarn with its electrically conductive coating when exposed to stresses typically occurring during utilization. Subsequently, the conductive yarn was used to manufacture a deformable capacitive pressure sensor. The obtained sensor signal was evaluated with respect to its sensitivity, linearity, characteristic response time and cyclic stability. Finally, the feasibility of the electrically conductive coated yarn for smart textile applications is discussed.

5.2 Experimental Section

5.2.1 Formulation of the silver-filled polymer solution

First, a polymer base solution, consisting of 15 wt% of the polyamide copolymer Platamid M1276 F (Arkema Specialty Polyamides, Colombes Cedex, France) dissolved in ethanol (Carl Roth, Karlsruhe, Germany), was prepared. The Platamid granules were filled together with the ethanol in a flask and stirred in a water bath at 64 °C until the granules were completely dissolved. Then, the temperature was

lowered to 35 °C to store the polymer solution until the silver-filled formulation was prepared. This temperature level was chosen to avoid precipitation and to minimize the evaporation of ethanol in the process, which could alter polymer concentration of the base solution and thus affect its coating properties. When polymer solutions with lower polymer concentrations (13 and 12 wt%) were utilized, the amount of ethanol that was added to the base solution was adjusted accordingly. Next, the plate-shaped silver particles (Ag Flake Powder Fa-S-12, DOWA Electronic Materials CO., LTD., Tokyo, Japan) with an average particle size of approximately 2.5 µm were added. The size distribution and scanning electron microscopy (SEM) images of the Ag particles are displayed in Figure 30. The amount of Ag added corresponds to 12, 15 and 20 vol% of the total nonvolatile components of the coating inks. A typical sample size was approximately 10 g. In order to facilitate a uniform particle distribution, the Ag particles were suspended in the polymer solution using a noncontact planetary mixer (SpeedMixer™ DAC 150.1FVZ, Hauschild GmbH, Hamm, Germany). The mixing process involved a three-step mixing and cooling cycle, each lasting 2 minutes at 2,000 rpm. Subsequently, the ionic liquid (IL) 1-Butyl-3-Methyl-imidazoliumiodide (Carl Roth, Karlsruhe, Germany) was added in varying quantities as conductivity-enhancing agent. To facilitate precise dosing, a 25 wt% solution of the IL was prepared using the organic solvent dimethyl sulphoxide (DMSO) ≥ 99.5 % (Carl Roth, Karlsruhe, Germany). Finally, the IL-DMSO mixture was added to the suspension of Ag particles in the polymer solution and mixed for an additional 1.5 minutes at 1,700 rpm.

5.2.2 Yarn-coating process

For the coating of the Nylon yarn, the laboratory scale coating device described in Figure 20 is used. The temperature of the oven is set to 280 °C and the coating speed to 2.8 m/min. In total, a maximum of five coating layers were applied to the Nylon yarn. A table with the selection of the guiding and coating nozzle diameters is shown in Table 5 of the supplementary information. For the coating process approximately 10 g of the silver filled polymer solution was prepared and continuously injected with a syringe into the reservoir of the coating device.

5.2.3 Rheological characterization of the polymer solution

The viscosity of the polymer solutions was determined at 35 °C. The measurements were conducted using a stress-controlled rotational rheometer (Physica, MCR 501, Anton Paar GmBH, Germany) equipped with a concentric cylinder geometry (inner diameter d = 27 mm, gap width w = 1.13 mm) and the viscosity η was determined in the shear rate range $1\ s^{-1} < \dot{\gamma} < 100\ s^{-1}$.

5.2.4 Electrical conductivity measurement

In order to determine the electrical conductivity of the dry Ag-filled polymer composite, the coating inks were applied to glass slides in thin layers, followed by a solvent evaporation step on a heating plate at 100 °C for 5 minutes in order to remove all the volatile components. Samples consisting of two layers meeting a total coating thickness of approximately 70 µm were prepared, and the films were cut into strips with a length of 4 cm and a width of 0.5 cm in order to determine electrical conductivity. The actual geometry (length l, thickness t, width w) of each sample was determined precisely using an outside micrometer. The electrical resistance was determined using a four-point probe (RLC 200, Grundig, Germany). From the electrical and geometrical data, the electrical conductivity was calculated according to equation (3).

5.2.5 Resistance measurement of the yarn

To measure the resistance of the coated yarn, the electrical resistance per unit length was determined. For this purpose, a 6 cm long piece of yarn was clamped between two electrodes using a customized 3D-printed yarn holder. These electrodes were connected to a Fluke 287 True-RMS Electronics Logging Multimeter (Fluke, Everett, USA), in order to measure the resistance of the yarn section (see supplementary information, Figure 60).

5.2.6 Bending test

The bending tests were conducted using a tensile testing machine (TA.XT.plus Texture Analyser, Winopal GmbH, Elze, Germany). The experimental setup is illustrated in Figure 61 of the supplementary information. Six yarn samples were clamped in parallel into a holder and attached to the upper holder of the device. The yarn was then deflected from a vertical to a horizontal direction over a roller with a diameter of 45 mm and clamped into another holder, which could be moved back and forth along two rails and was loaded with a 225 g weight at the rear. Due to the weight, the yarn was always kept in a tensioned state. The yarn samples were then cyclically moved up and down at a speed of 17 mm/s at the upper holder, with the yarn being moved along by the movable rail and bent over the roller. Resistance measurements, as described in the section *Resistance Measurement of the Yarn* were conducted and evaluated before the test and after 300, 1,200 and 3,600 repeating bending cycles.

5.2.7 Washing test

For the washing test, six approximately 12 cm long coated yarn pieces were placed in a cotton bag and washed in a household washing machine (Express Edition Serie 4, Robert Bosch Hausgeräte GmbH, Munich, Germany) at 40 °C for 50 minutes and spun at 1200 revolutions per minute. Afterwards, the yarn was air-dried. Before the first washing cycle and after each subsequent trial, the resistance of the yarn pieces was measured and evaluated as described in the section 5.2.6.

5.2.8 Light microscopy observation

To investigate the surface quality of the coated yarn, an optical microscope (Keyence VHX-6000, Keyence Corporation, Japan) was utilized.

5.2.9 SEM observation

The Ag particles and the morphology of the coating layers on the yarn were imaged using scanning electron microscopy (SEM) (S-4500; Hitachi High-Technologies Europe GmbH, Krefeld, Germany).

5.2.10 Sensor manufacturing

The pressure sensor was fabricated using two yarns (length: 60 mm) as the electrodes and PDMS films (Sylgard 184, Dow Corning Corp., Midland, USA) (thickness: 300 µm; size: 20 mm × 20 mm) as substrates. A PDMS resin (thickness: 10 µm) was applied to the PDMS substrate as an adhesive layer, and fixed the yarns on the substrate. The first patterned substrate was coated with 120 µm thick Ecoflex (00-10, Smooth-On Inc., Macungie, U.S.A.), and the second substrate was subsequently pressed orthogonally on top of it. After that, it was cured at 80 °C for 30 mins, and the capacitive sensor was formed, as shown in Figure 25a). In addition, a yarn sensor array was prepared using ten filaments (length: 100 mm) as the electrodes and PDMS films (thickness: 300 µm; size: 55 mm × 55 mm) as substrates. The preparation process was similar as before, and a 5×5 array was formed, as shown in Figure 27.

5.2.11 Sensor performance tests

A customized test platform was used to analyze the performances of the sensors, based on a pressure sensor (ULC-2 N, Interface Inc., Scottsdale, America) and z-axis displacement lifting platform. An LCR Meter (E4980AL, Keysight Technologies, Santa Rosa, America) was used to measure the electrical properties of the sensors, particularly the load-dependent change in capacitance $\Delta C/C_0$.

5.3 Results and discussion

5.3.1 Coating process

To manufacture coated yarn, a laboratory scale coating machine was customized. Figure 20 illustrates the process of applying a single coating layer to the yarn using this machine at a maximum speed of

6.9 m/min. The machine consists of several key components, as displayed in Figure 20a): (1.) a freely rotating spool loaded with the bare yarn, (2.) a coating nozzle for the precise application of the silver-filled polymer solution, (3.) an oven used to dry the wet-coated yarn, (4.) a cooling station where the silver-filled polymeric coating is cooled down and (5.) a spool directly connected to a motor winds the coated yarn. Figure 20b) shows a magnification of the wet-coating application segment. It consists of a guiding nozzle marginally larger than the yarn, guiding its path. A reservoir, filled with the silver-filled polymer solution using a syringe and a coating nozzle that controls the thickness of the wet coating applied to the yarn. Figure 20c) shows a commercially available coating nozzle commonly employed in conventional wire coating processes. These nozzles feature variable core drilling diameters, typically ranging from 100 to 800 µm for this specific type. Figure 20d) schematically shows the wet-coating application of a polymer solution filled with silver particles onto the yarn within the coating nozzle, followed by a drying step to remove the solvents, as sketched in Figure 20e). The result is a thin solid polymer layer filled with an electrically conductive silver particle network. The coating thickness after a single application ranges between 2 and 7µm, depending on the dry content of the polymer solution. By repeating these coating steps using guiding and coating nozzles with appropriately increasing diameter, several coating layers can be applied on top of each other, enabling the precise adjustment of the coating thickness. Even composition gradients can be tailored using different polymer solutions, e.g., with different fillers, in subsequent coating steps. In the wire coating industry several nozzles with slightly increasing diameters are connected enabling a quick layer buildup[154]. An industrial coating machine is described in more detail in Figure 57 of the supplementary information.

To formulate composite polymer solutions that yield good coating properties and high electrical conductivity, we first investigated the electrical properties of the dry coating layer after solvent evaporation (Figure 21). Next, the solvent content and consequently the viscosity of the silver-filled polymer solutions were adjusted (Figure 22), and finally coating trials were performed.

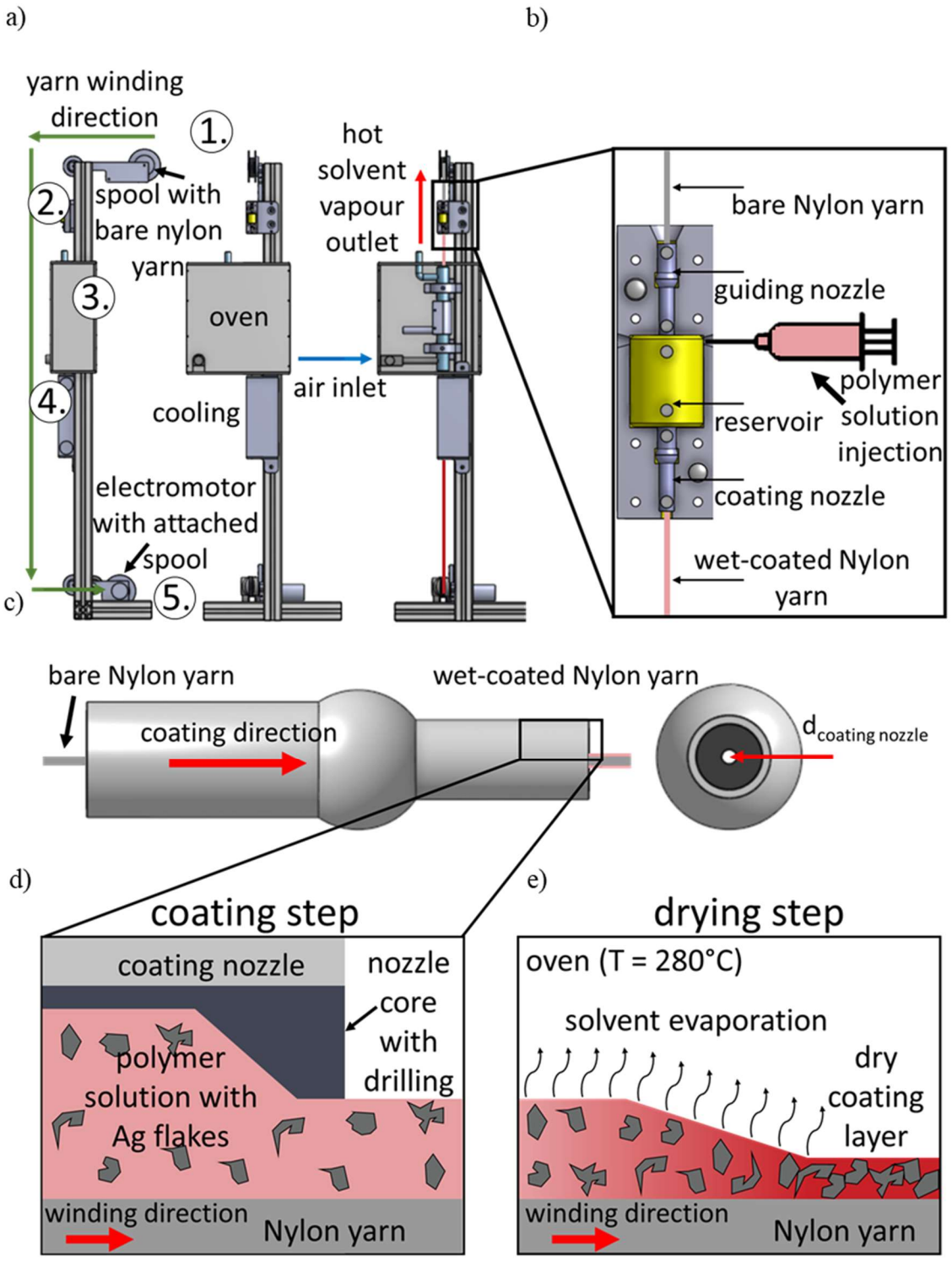

Figure 20. Description of the yarn coating process. a) A self-constructed, continuously operating laboratory-scale coating device capable of achieving a maximum coating speed of 6.9 m/min. The device includes the following key components: (1.) freely rotating spool for the bare yarn, (2.) coating nozzle, (3.) drying oven, (4.) cooling station, and (5.) winder and spool for the coated yarn. The green arrows indicate the coating direction. b) A magnification of the wet-coating application segment. c) A coating nozzle commonly employed in conventional wire coating processes. d) Wet-coating application with a polymer solution filled with silver particles onto the yarn. e) A subsequent drying step to remove the solvents.

5.3.2 Electrical characterization of the coating material

The dry coating layer (Figure 20e) is a composite material including a mixture of polyamide and the ionic liquid (IL) 1-Butyl-3-Methyl-imidazolium iodide, filled with silver particles. At the low filling level desired here, a uniform distribution of the silver particles in the polymer matrix would result in low conductivity. Thus, the IL is added to promote the formation of a percolating particle network during the drying process. The IL partially removes the isolating fatty acids from the silver flakes and causes a microphase separation, which induces the formation of an electrically conductive network and hence increases the electrical conductivity of the resulting coating [2, 3, 6, 35]. Accordingly, the electrical conductivity of the composite depends on the volume fraction of the added silver as well as on the volume ratio of IL to Ag. Corresponding conductivity data are shown in Figure 21. The electrical conductivity of coatings with a constant Ag fraction of 20 vol% but increasing IL concentration is shown in Figure 21a). Conductivity drastically increases at VIL/VAg ratios between 0.02 and 0.04 reaching κ values around 1,000 S/cm, and a further slight increase in conductivity is observed at higher IL content. An excessive IL concentration, however, can result in the formation of large Ag agglomerations, as evidenced in Figure 58 of the supplementary information. This can lead to nozzle blockage during the coating process and results in an uneven coating. Thus, for subsequent investigations, the formulation with a VIL/VAg ratio of 0.04 was chosen. This ratio yielded a commendable conductivity of approximately 812 S/cm at 20 vol% Ag content, while avoiding the formation of large agglomerates. igure 21b) shows the conductivity of the dry coating layers as function of silver content, maintaining a constant ratio of VIL/VAg = 0.04. At silver fractions of 12, 16, and 20 vol%, the measured conductivities were approximately 498, 689, and 812 S/cm, respectively. These findings highlight the IL's effectiveness in promoting the formation of a percolating silver particle network, even at low Ag fractions within the dry coating. Typically, the percolation threshold, i.e. the filler concentration at which formation of a continuous, sample spanning particle network and hence a significant conductivity sets in, for similar silver particle-filled polymer films falls between 20 and 30 vol% [18]. Additionally, when compared to results for Ag nano-wire (NW) coated yarn with maximum conductivities of approximately 81 S/cm [75] and 300 S/cm [153], the conductivity achieved here is notably high. However, it is important to note that these measurements specifically concern the coating itself, not a coated piece of yarn. Nevertheless, the results show that it is possible to adjust the conductivity of the coating within a feasible range by varying the IL and Ag concentration. For the next steps in the manufacturing process yarn was coated with a thermoplastic, polyamide-based layer including 20 vol% Ag and a ratio VIL/VAg = 0.04. The formulation containing 20 vol% Ag was selected to achieve a high electrical conductivity of the resulting yarn and still providing sufficient mechanical durability in typical applications. A higher particle content in the coating would result in a higher conductivity but would at the same time reduce adhesion and compromise long-term stability. Formulations with lower Ag content are expected to have at least similar, if not superior, mechanical reliability but, of course, yield a lower electrical conductivity.

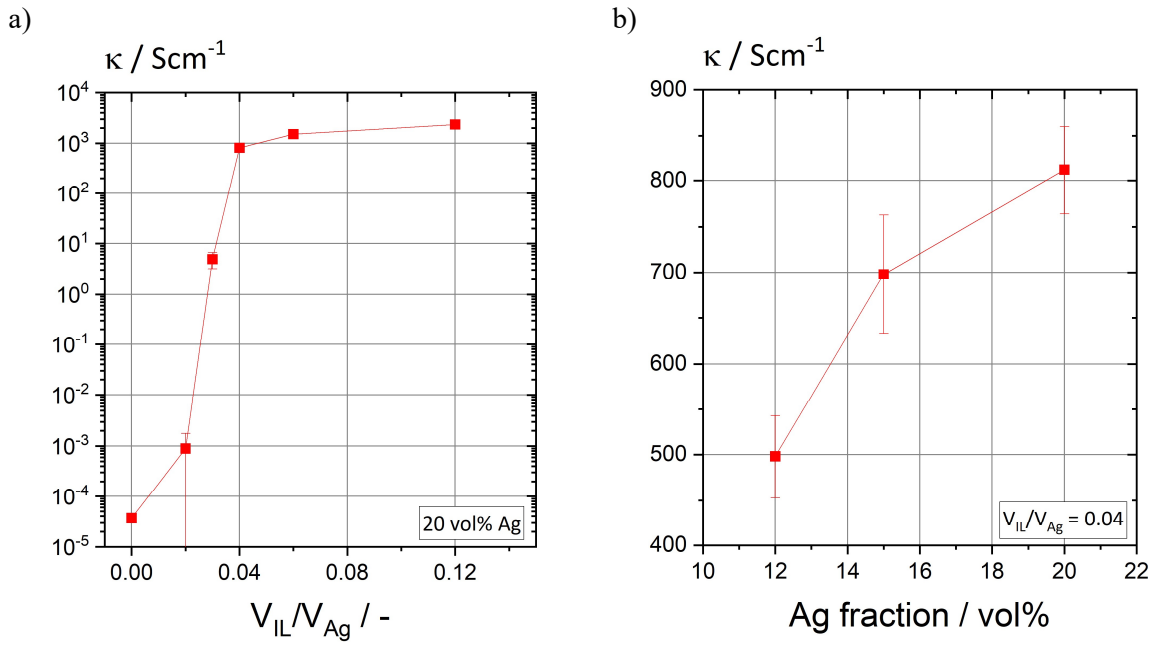

Figure 21 a) Electrical conductivity κ of solvent-free coatings with a constant Ag fraction of 20 vol%, plotted against the IL-Ag volume ratio. b) Electrical conductivity κ of solvent-free coatings with a constant IL-Ag volume ratio of 0.04, plotted against the Ag volume fraction.

5.3.3 Viscosity adjustment of the polymer solution

After adjusting the dry content ratio (Ag, IL) in the polymer solution, it is also necessary to optimize the solvent concentration and, consequently, the viscosity of the polymer solution to achieve high surface quality. Initially, the impact of adding Ag and IL on the viscosity of a base polymer solution with a polymer concentration of 15 wt% was investigated, as depicted in Figure 22a). The polymer solution exhibits purely Newtonian behavior, with a viscosity of approximately 0.1 Pa·s within the observed shear rate range of 1 to 100 s^{-1}. Introducing particles results in a slight viscosity increase. Additionally, the silver-filled formulation exhibits weak shear-thinning behavior within the observed shear rate range. Notably, the flow curve of the formulation containing IL alongside the particles exhibits similar behavior to that containing only particles. Furthermore, the formulation containing the same amount of IL but without particles shows only a slight increase in viscosity, from 0.1 Pa·s for the polymer solution alone to 0.108 Pa·s with the addition of IL. This increase is due to the IL's inherently higher viscosity of approximately 0.39 Pa·s. The flow curve for IL is provided in Figure 59 of the supplementary information. This suggests that while the addition of IL induces microphase separation and particle network formation during the drying process in this system (see supplementary information, Figure 58), it just slightly affects the viscosity of the initial polymer solution when using a V_{IL}/V_{Ag} ratio of 0.04.

Figure 22b) displays the flow curves of formulations with an Ag fraction of 20 vol% with respect to the nonvolatile components and a V_{IL}/V_{Ag} ratio of 0.04 but different polymer concentrations of the base solution. As expected, the viscosity increases with increasing polymer concentration and at a shear rate of 10 s^{-1}, viscosity values of 0.2, 0.1 and 0.06 Pa·s, respectively, are found for base solutions with 15, 13 and 12 wt% polymer content. To facilitate the utilization of these formulations in traditional wire coating machines and thus achieve high-throughput production of conductive yarn, the viscosity of the polymer solutions should be higher than 0.03 Pa·s, a criterion met in all three instances [155].

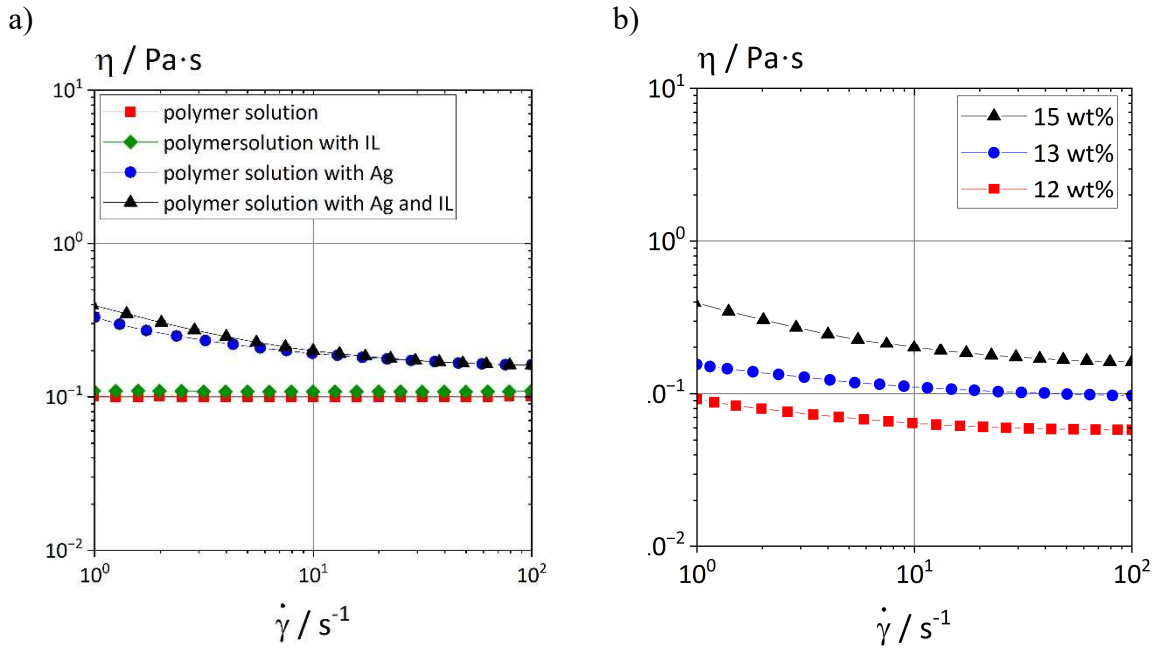

Figure 22a) Viscosity η as a function of shear rate $\dot{\gamma}$ for various polymer solutions: the pure polymer solution at a concentration of 15 wt% (red squares), the polymer solution with silver particles comprising 20 vol% of the nonvolatile components (blue circles), the polymer solution with the same silver concentration as well as added IL with a V_{IL}/V_{Ag} ratio of 0.04 (black triangles), and the polymer solution containing the same volume of IL but no silver particles (green diamonds). b) Viscosity η as a function of shear rate $\dot{\gamma}$ for formulations including 20 vol% Ag (with respect to the nonvolatile components), maintaining a V_{IL}/V_{Ag} ratio of 0.04 but with different polymer concentrations in the base solution: 12 wt% (red squares), 13 wt% (blue circles), and 15 wt% (black triangles).

5.3.4 Yarn coating trials

Yarn coating trials were conducted using solutions with 12, 13, and 15 wt% polymer concentration. The coating process employed the coating machine illustrated in Figure 20. The coating speed was set to 2.8 m/min, while the oven temperature was maintained at 280 °C. It is important to note that the oven temperature could not be increased further without risking damage to the nylon yarn.

Figure 23a), b) and c) display the quality of yarn coatings for formulations containing 15, 13, and 12 wt% polymer in the base solution after four, four, and five coating cycles, respectively. Noticeable differences in surface quality are observed. Figure 23a) shows numerous craters and bubbles along the Nylon yarn, resulting in a generally poor surface quality. However, as the polymer concentration decreases (as seen in Figure 23b), the surface quality improves, although occasional bubbles and craters persist. Given the unsatisfactory coating qualities observed with both 15 and 13 wt% polymer solutions, the process was halted after four coating cycles. Further reduction in polymer concentration to 12 wt% resulted in sufficient surface quality without defects, even after the fifth coating cycle (Figure 23c). It is likely that bubbles and craters form during the coating process because a solid polymer layer develops on the surface before all the solvent has evaporated. The trapped solvent beneath this layer continues to evaporate, building pressure until it deforms the polymer surface, resulting in bubble formation. As more solvent escapes, these bubbles can burst, leaving behind craters. This phenomenon is also observed in conventional wire coating processes [154].

The corresponding coating thicknesses in relation to the number of coatings are depicted in Figure 23d). The maximum measured coating thicknesses were approximately 22 µm and 16 µm for Nylon yarn coated with polymer solutions containing 15 and 13 wt%, respectively. In contrast, the coating thickness of Nylon yarn coated with a formulation containing 12 wt% was approximately 17 µm after five coating

cycles. After each coating cycle, the electrical resistance of the yarn was measured, as illustrated in Figure 23e). As can be expected, for all three formulation types, resistance decreased with an increasing number of coatings, and hence thicker layers of conductive material on the yarn. The minimum resistance recorded for formulations containing 15 and 12 wt% polymer after four coating cycles was approximately 21 and 17 Ω/cm, respectively. Notably, the formulation with 12 wt% polymer exhibited a resistance of approximately 7.5 Ω/cm after five coating cycles, similar to results reported in other publications, with values between 0.2 and 20 Ω/cm for nano-wire coated yarns [69, 71]. Further reduction in resistance could likely be achieved by either increasing the number of coatings or by increasing the silver concentration. Consequently, the process offers adaptability to adjust yarn resistance to the level required for different applications.

Additionally, Figure 23f) presents the cross-section of the Nylon yarn after five coating cycles with the formulation containing 12 wt% polymer and Figure 23g) and h) scanning electron microscopy (SEM) images of the coated yarn surface and the cross section. The results show that it is possible to apply thin layers of an electrically conductive polymer film with sufficient surface quality at relatively high speed of 2.8 m/min which could potentially be increased up to 800 m/min by using an industrial coating machine, as depicted in Figure 57 of the supplementary information. This scale has previously been demonstrated for electrically conductive polymer films coated onto copper wires [6].

Moreover, an additional critical aspect is the solids content of the initial coating ink. In processes where silver and silver-coated copper nano-wires suspended in solvents were applied to yarn through dip-coating, substantial amounts of solvent were required, due to the limited dispersibility of nano-wires in solvents. In these cases particle concentrations ranging from 1.25 to 8 mg/mL were used [69, 71, 153]. In contrast, the formulations employed in this study feature orders of magnitude higher solids concentrations, totaling 345 mg/mL, with 250 mg/mL attributed to silver and 95 mg/mL to the polymer component. Thus, the solvent consumption and hence the required drying energy is much lower, which makes this approach much more feasible for industrial application. The cost associated with the material itself is primarily determined by the cost of the Ag particles, resulting in an approximate price of 0.04 $\$/m_{yarn}$, slightly higher than that reported for Ag nano-wire coated yarn ranging between 0.008 and 0.035 $\$/m_{yarn}$ [69]. While the costs for polymers filled with pure silver particles are slightly higher than for the metal nano-wire systems mentioned above, this approach offers the advantage of substituting silver particles with less expensive alternatives such as silver-coated copper or glass particles as suggested previously [6]. Additionally, carbon black (CB) or Carbon Nanotubes (CNT) could serve as alternative options, further reducing material expenses. As the polymer matrix provides both mechanical strength and adhesion to the yarn, the system does not rely on good adhesion between the conductive material and the yarn surface, as pointed out in previous studies focusing on metal nano-wire systems [69, 71]. This characteristic opens up new possibilities, such as employing microparticles instead of nano-sized materials, thereby simplifying the production process since micron-sized particles are easier to handle and to incorporate into formulations. Furthermore, applying coating layers containing different kinds of particles on top of each other could also be an option to attain specialized properties, such as conductivity gradients. Another option is to incorporate small amounts of micro or nano-sized pigments to color the yarn. This allows for tailoring the yarn's appearance according to customer preferences with minimal changes to the standard formulation.

Given that the best coating quality was attained utilizing a base solution comprising 12 wt% polymer, this specific yarn serves as the focus for subsequent investigations.

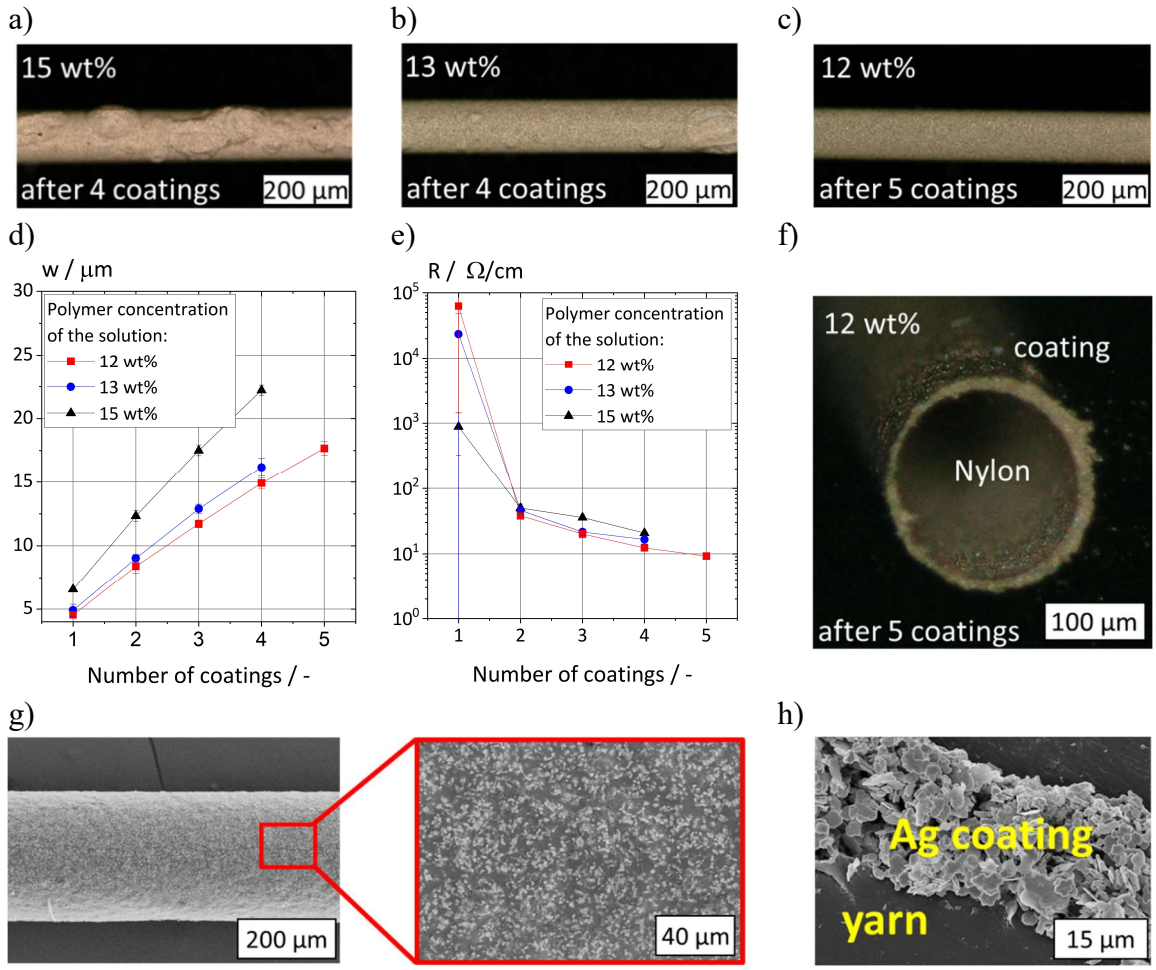

Figure 23. Light microscopy images of the surface of Nylon yarn coated with formulations containing 20 vol% Ag in the final dry film, a V_{IL}/V_{Ag} ratio of 0.04, and a polymer concentrations of a) 15 wt%, b) 13 wt%, and c) 12 wt% in the base solution. Images were taken after four or five coating cycles, as depicted in the images. d) The coating thickness and e) the electrical resistance for Nylon yarn coated with Ag- and IL-filled formulations with 15 wt% (black triangles), 13 wt% (blue circles), and 12 wt% (red squares) polymer in the base solution, plotted against the number of coatings. f) light microscopy image of the cross-section, g) SEM image of the surface, including a magnification (surrounded by a red rectangle) and h) SEM image of the cross-section of Nylon yarn coated with the formulation containing 20 vol% Ag in the final dry film, a ratio $V_{IL}/V_{Ag} = 0.04$, and a polymer concentration of 12 wt% in the base solution. The images were taken after five coating cycles.

5.3.5 Washing and bending tests

Materials suitable for manufacturing flexible sensors and e-textiles must be able to withstand repeated washing and also bending. Accordingly, initial stability tests regarding these properties were conducted. Figure 24a) shows the material resistance as a function of the number of washing cycles. Although the resistance slightly increases after the first washing cycling, from 7.5 Ω/cm ± 0.5 Ω/cm to approximately 10 Ω/cm ± 1.6 Ω/cm, it remains constant for the next four washing cycles, indicating a good washing resistance for this prototype material. Figure 24b) presents the results of the bending tests. The resistance slightly increases from 7.5 Ω/cm ± 0.5 Ω/cm to 8.3 Ω/cm ± 1.7 Ω/cm after more than 3,000 bends, this is still within experimental uncertainty thus demonstrating the very good mechanical durability of our conductive yarn. To further improve its performance, the yarn could be coated more than five times to improve the toughness of the conductive network or an additional protective layer could be added.

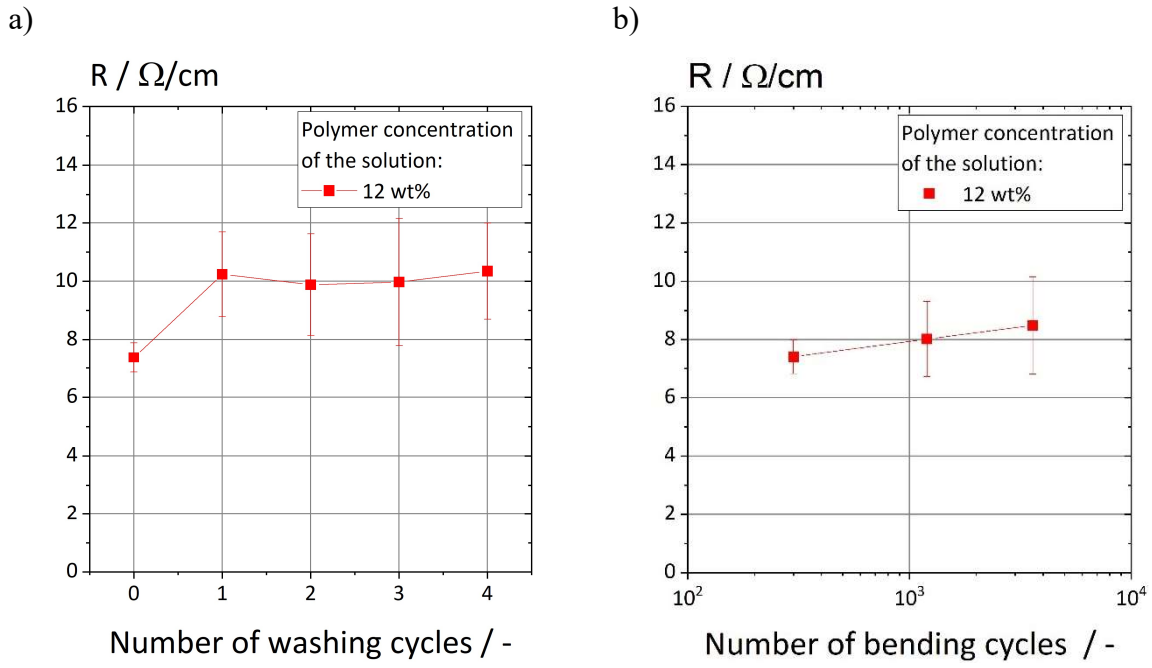

Figure 24 The electrical resistance of Nylon yarn coated with five layers of a formulation containing 20 vol% Ag in the final dry film, a ratio $V_{IL}/V_{Ag} = 0.04$, and a polymer concentration of 12 wt% in the base solution, plotted against the number of a) washing and b) bending cycles.

5.3.6 Application for flexible pressure sensor

The simplest possible design was used to illustrate the applicability of the conductive yarn for flexible pressure sensors. The capacitive sensor consists of two pieces of conductive yarn (coating thickness = 20 µm, φ_{Ag} = 20 vol%, κ = 812 S/cm) separated by a layer of Ecoflex. Additional layers of polydimethylsiloxane (PDMS) are applied on the top and bottom to provide further protection, as shown in Figure 25a). By applying pressure to the surface of the sensor, the distance between the opposing yarn filaments decreases which leads to an increase in capacitance, as shown in Figure 25b).

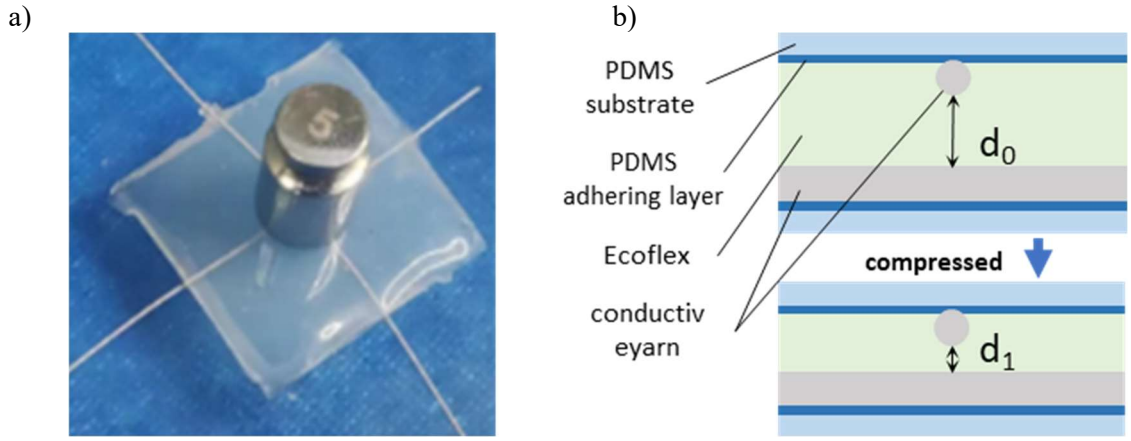

Figure 25 a) The flexible pressure sensor b) Working principle of the flexible pressure sensor.

Figure 26a) to e) illustrate the pressure-sensing functionality of the simple device. The conducted tests characterize the sensor specifications in terms of the changes in capacitance $\Delta C/C_0$ in response to a) increasing loading pressure, b) stepwise increasing increments in loading pressure, c) cyclic changes in loading pressure, d) duration of pressure application over time, and e) extended periods of pressure cycling. The results demonstrate that the sensor is capable of capturing the pressure range of 1 to 20 kPa (Figure 26a) which is adequate for capturing everyday activities such as handshakes, holding a mug, or

conducting medical diagnoses [117]. With a sensitivity in the linear regime of 10^{-3} kPa^{-1} (Figure 26a) and a response time of 224 ms (Figure 26d), this sensor is in a similar specification range as other products, however it is not among the best performing ones with sensitivities of up to 217.5 kPa^{-1} and response times of sometimes less than 10 ms [117, 156, 157]. These preliminary tests show that the conductive yarn can be used for manufacturing sensors for integration into textiles, but further improvement is required for widespread technical application.

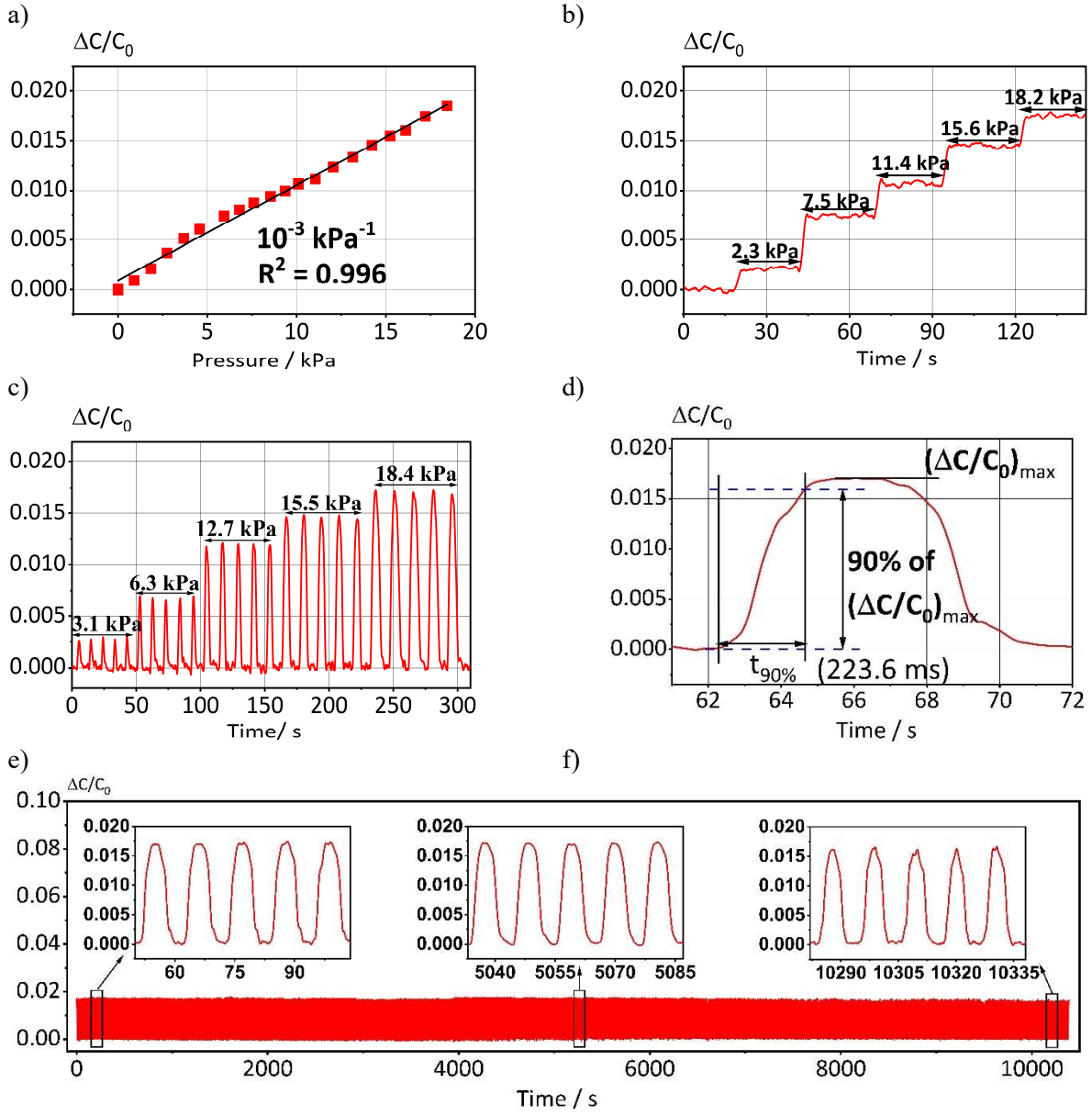

Figure 26 Sensing capability of the flexible pressure sensor: The relationship between $\Delta C/C_0$ and a) increasing loading pressure, b) stepwise increasing increments in loading pressure, c) cycling changes in loading pressure with peak loads of 3,100 Pa, 6,300 Pa, 12,700 Pa, 15,500 Pa, and 18,400 Pa, d) duration of pressure application over time at a pressure of 18,400 Pa, and e) extended periods of pressure cycling with 1,000 loading-unloading cycles at a peak pressure of 18,400 Pa.

When more than two pieces of yarn are used, an array can be formed, as shown in Figure 27. This 5 x 5 yarn arrangement allows for the detection of the spatial distribution of small input pressure signals, enabling the sensor to distinguish not only the weight but also the shape of objects placed on it. This capability is demonstrated using two wooden blocks: a small one weighing 0.65 g (Figure 27a) and a larger one weighing 3.92 g (Figure 27b). The shape of the contact area between the block and the sensor

layer can be retrieved from the spatial variation of the ΔC/C0 signal in the 5 x 5 matrix as shown in Figure 27 on the right. Of course, due to the simple layout, the spatial resolution is limited here, but further enhancement of the spatial resolution is straightforward by using more yarn at a smaller distance and also by using thinner yarn pieces.

a)

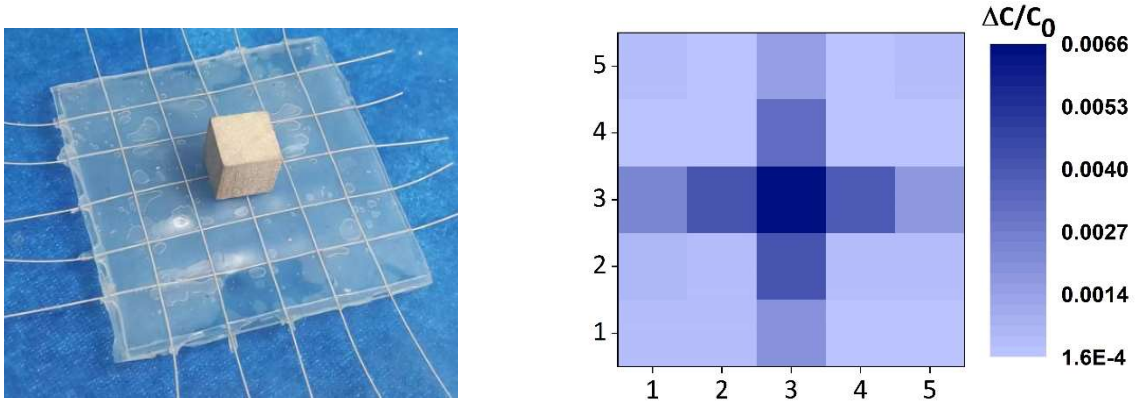

b)

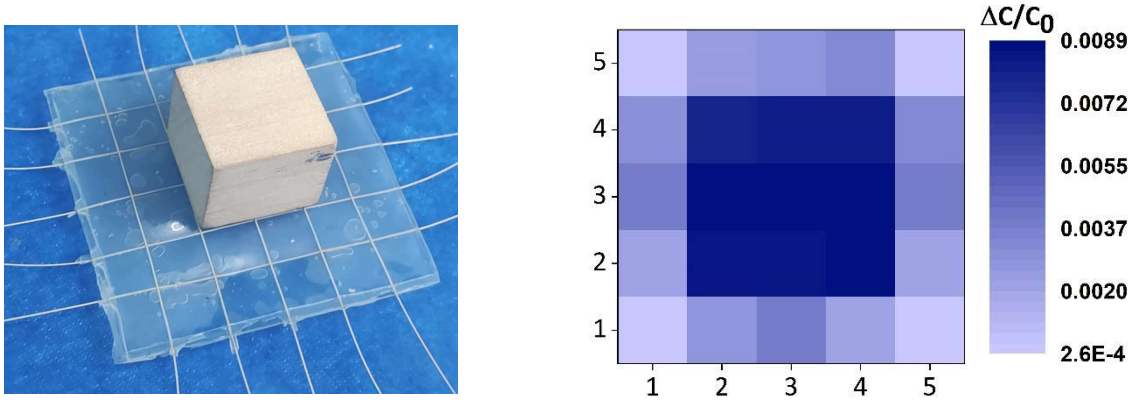

Figure 27 Spatial distribution of input pressure signals on a 5 x 5 yarn sensor array. Images and 2D intensity (ΔC/C0) map of the sensor with a) a small (0.62 g) and b) a large wooden block (3.92 g) placed at the center of the sensor array.

Figure 28 illustrates the changes in capacitance when sensing a finger or just the fingertip under no pressure loading. Compared with the fingertip, the finger has larger contact area on the surface of the sensor, which results in more capacitance drop. Therefore, the sensor can detect changes effectively as long as the finger or fingertip is near the electrode, which could be used in touch panels.

The change in capacitance during touch detection arises from the alteration in the edge electric field rather than from a change in the dielectric's size (Figure 28a). In this context, C_{total}, C_p, C_f, and Cd represent the total sensor capacitance, electrode plate capacitance, edge capacitance of the Ecoflex dielectric layer, and edge capacitance of the medium directly above the sensor, respectively. When no pressure is applied, the sensor remains physically undeformed, meaning C_p and C_f stay constant while C_{total} varies as C_d varies when the fingertip approaches the sensor surface. As depicted in Figure 28b) when an object, e.g., the fingertip approaches the sensor, the edge electric field (the medium directly above the sensor) is redirected to the ground through the finger, causing a decrease in capacitance. Compared with the fingertip, the finger has larger contact area on the surface of the sensor, which results

in more capacitance drop. Therefore, the sensor can detect changes effectively as long as the finger or fingertip is near the electrode, which could be used in application of touch panels.

a)

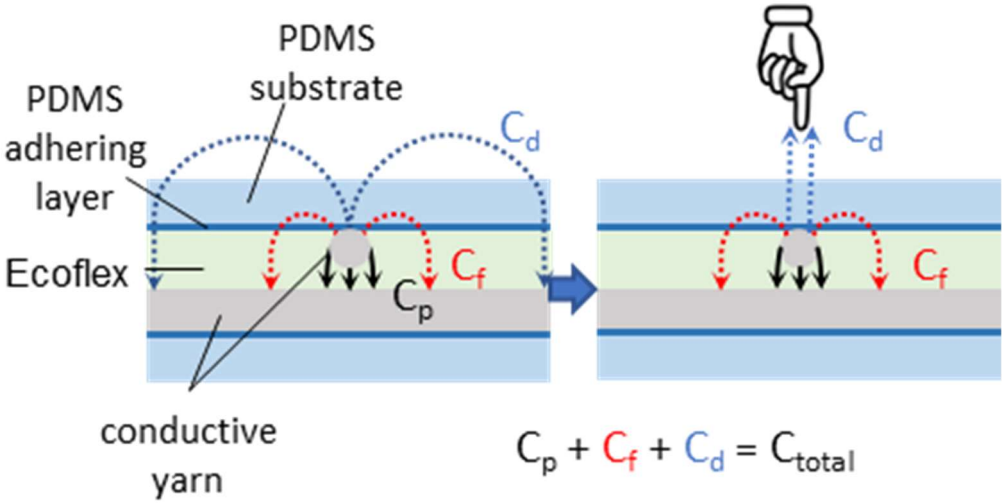

b)

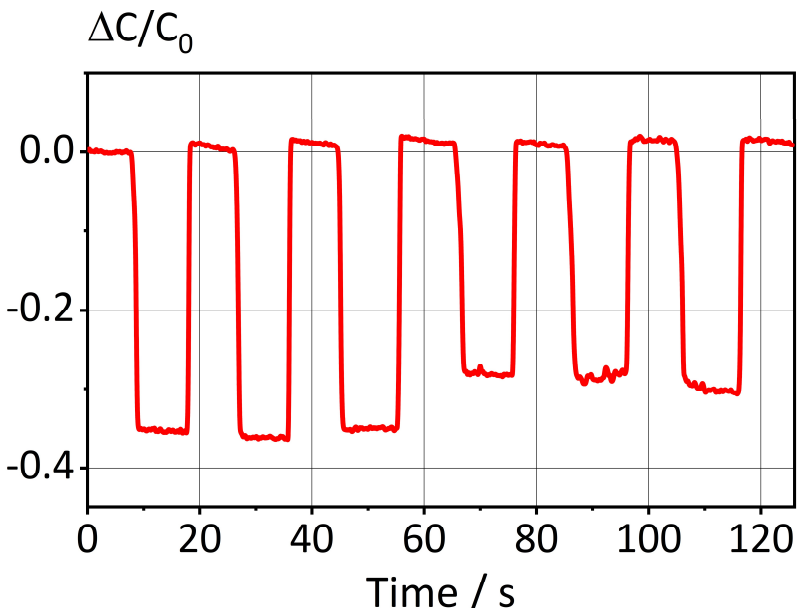

Figure 28 a) Working principle of capacitance changes caused by an approaching finger (large area) or fingertip (small area). C_{total}, C_p, C_f, and C_d represent the total sensor capacitance, plate electrode capacitance, edge capacitance in the Ecoflex overlay, and edge capacitance of the medium directly above the sensor (finger or fingertip). b) Capacitance changes over time due to an approaching finger or fingertip without applying pressure to the sensor.

5.4 Conclusion

This study presents an alternative production route for electrically conductive Nylon yarn immediately suited for upscaling to commercial-scale production capacities adequate for the textile industry, since it is based on a process similar to the industrial fabrication of insulated copper wires used in large quantities in the electrical industry [154].

To demonstrate feasibility, a laboratory-scale coating machine was constructed to apply coating layers at a speed of 2.8 m/min. The coating ink used here is based on a solution of the thermoplastic polyamide Platamid M1276 F (T_M = 110 – 120 °C) in ethanol. Silver flakes (D_{50} = 2.5 µm) are suspended in this

solution to provide electrical conductivity. Furthermore, 1-Butyl-3-Methyl-imidazoliumiodide, an ionic liquid, is added to further enhance conductivity [3, 6]. After solvent removal, the final dry coating layer included 20 vol% silver, a V_{IL}/V_{Ag} ratio of 0.04, and provided a conductivity of 812 S/cm. Reducing the silver content to 16 vol% or 12 vol% resulted in conductivity values of 689 and 498 S/cm, respectively.

The viscosity of the coating ink is in the range of 50 mPa·s, and careful adjustment of the viscosity depending on coating speed and drying conditions is necessary to ensure high surface quality [6]. Here, a polymer concentration of 12 wt% in the base solution yielded the best results, producing a coating thickness of 17 µm after five coating cycles, with a resistance of 7.5 Ω/cm. Washing and bending tests were performed to assess the yarn stability in textile applications. Following several washing cycles and more than 3000 bending cycles, resistance marginally increased to 10 and 8.3 Ω/cm, respectively, indicating sufficient stability for textile applications considering the prototype level of development.

Initial tests were conducted using the conductive yarn in flexible, capacitive pressure-sensing applications. Based on the simplest design of two perpendicularly crossing filaments, we could show that the capacitance change ΔC/C0 is sufficient to detect pressures ranging from 1 to 20 kPa sufficient for typical everyday pressure scenarios. The sensitivity of the sensor is approximately 10^{-3} kPa^{-1} with a response time of roughly 223.6 ms. Even after 1,000 loading-unloading cycles at a pressure of 18.4 kPa, the sensor remained sensitive enough to accurately measure pressure differences. Additionally, a simple sensor layout with a rectangular 5 x 5 filament array could be used to demonstrate that spatial differences in capacitance change can be detected and may be used to detect pressure variations or the shape of objects in contact with the sensor. Further enhancement of the spatial resolution is straightforward, using more filaments at smaller distance and/or also by using thinner filaments.

The research presented here offers a versatile formulation platform for manufacturing textile yarns coated with an electrically conductive surface layer. It may serve as a foundation for further research and development activities enabling industrial-scale coating at even speeds up to 800 m/min desired for mass production. The cost of the material, mainly due to the silver particles, is slightly higher than for yarn types that used silver coated or silver nano-wires. However, the far lower consumption of solvent and the corresponding reduction in drying efforts outweighs this downside, and beyond that silver may be replaced by less valuable materials such as silver-coated glass or copper particles, without substantial loss of conductivity [6]. Additionally, the yarn's appearance may be customized to match customers preferences, simply by incorporating small amounts of pigment to color the yarn. Here, we have used a Nylon filament as model system but a transfer of the concept to other yarn materials, such as cotton or silk, may also be explored in future research. Moreover, the thermoplastic properties of the conductive coating layer may be leveraged to interconnect different sensor components without need for solder or additional electrically conductive adhesives. Investigating this additional benefit was beyond the scope of this work. In summary, the work outlined here may set the starting point for the development of a versatile process and material platform enabling mass production of low-cost conductive yarns enabling widespread wiring and sensing applications in smart textiles.

5.5 Acknowledgement

Basic funding of the Institute for Mechanical Process Engineering and Mechanics at Karlsruhe Institute of Technology provided by the State of Baden-Württemberg. The National Nature Science Foundation of China (No. 51861135105), and Fund of Robot Technology Used for Special Environment Key Laboratory of Sichuan Province (22kftk02). The manuscript was written through contributions of all authors. All authors have given approval to the final version of the manuscript.

Chapter 6 TECC-Wire for interconnecting solar cells

Full title: *Highly Conductive Coated Wires for Interconnection of Solar Cells with TECC-Wire Technology*

Authors: *Jonas Marten, Mona Schnaiter, Yonas Zemen, Lars Podlowski, Stefan Ricken, Norbert Willenbacher*

Status: *published* [6]

Bibliographic data: *Solar Energy Materials and Solar Cells 273 (2024): 112966*; DOI: https://doi.org/10.1016/j.solmat.2024.112966.

Abstract

TECC-Wire (thermoplastic and electrically conductive coated wire) represents a promising interconnection technology for temperature sensitive solar cells. TECC-Wire uses round copper wires (160 – 300 µm) coated with a thermoplastic polymer layer (10 – 20 µm), filled with electrically conductive particles. This study presents a new wire coating formulation based on a polyamide-type wire enamel (Voltatex® 8609 ECO, melting temperature 180 °C), filled with 12 vol.% silver resulting in a conductivity of 480 S/cm. Single half-cut M6 heterojunction (SHJ) solar cells were contacted with the manufactured wires using a laboratory scale stringing machine.

Peel tests were performed to characterize the adhesion of the wires to the cell surface, module performance was evaluated using electroluminescence (EL) imaging and current-voltage (IV) measurements, damp heat (DH) tests were used to evaluate the long-term stability of the modules. The wires adhere well to the cells with a peel force of more than 1.5 N/mm, and the highly conductive coating has proven to be robust when contacted with different pressure, which might be beneficial for a reliable high throughput solar module production. The obtained fill factor FF = 81.25 ± 0,12% is similar to those achieved for solar modules connected via standard soldering techniques IEC standard DH tests confirmed that, the modules exhibiting a power loss of less than 5 % after 1000 hours of storage at +85 °C and 85 % relative humidity. These results are very encouraging for further development of the technology towards a low temperature, solder-free, low cost and robust cell interconnection technology.

6.1 Introduction

Recent solar cell types, like silicon heterojunction cells, are expected to significantly increase their market share from less than 10 % in 2022 to up to 25 % by 2033 [158]. While these advanced cells offer improved efficiency, silver consumption for metallization is about twice as high as for conventional PERC (passivated emitter rear contact cell), and the high silver consumption could lead to a bottleneck in the further expansion of PV installation, urgently needed for the aimed transition to a sustainable energy supply. Consequently, busbarless interconnection designs, which reduce silver consumption for metallization, are expected to experience substantial market growth, exceeding 30 % of the world market share by 2033 [158, 159].

Moreover, the temperature sensitivity of heterojunction cells demands interconnection methods that can be applied at temperatures below 200 °C. Conventional soldering techniques typically require temperatures above 230 °C [90, 160]. However, the Smart-Wire concept developed by Meyer Burger [102], which combines low-temperature soldering using a bismuth-tin alloy (melting temperature < 150 °C) with the multi-wire design, has already been successfully implemented on the market. This approach not only reduces silver usage, but also offers enhanced reliability against defects, minimized shading, and lower interconnection temperatures [102]. Nevertheless, the scalability of Smart-Wire for terawatt production may be hindered due to the high consumption of bismuth, so far [79].

TECC-Wire developed by Solyco Technology GmbH [103], presents a promising alternative multi-wire concept for interconnecting temperature-sensitive solar cells. This innovative approach utilizes round wires (diameter = 160 – 300 µm) coated with a thermoplastic and electrically conductive coating, enabling bonding to the transparent conductive oxide (TCO) layer on the wafer surface at temperatures well below 200 °C [103, 112]. TECC-Wire provides adhesion to both the metallization fingers as well as to TCO, eliminating the need for a busbar print [113]. The mechanical bonding between the copper wire and the wafer is provided by the thermoplastic matrix of the wire coating, whereas the electrical connection between the wire and the wafer is provided by the embedded electrically conductive particles. The use of a thermoplastic coating and the freedom to choose the electrically conductive filler material provide distinct advantages. The polymer matrix can be adjusted to meet the requirements of a given wafer substrate with respect to wettability and adhesion. Moreover, polymer glass transition or melting temperature can be adjusted in a broad range to meet temperature specifications of the process. Another advantage of TECC-Wire is that the wire coated with a thermoplastic material can be stored at room temperature for at least several months, i.e. its production is decoupled from the module manufacturing process. Furthermore, the electrical conductivity can be adjusted in a wide range through the appropriate choice of filler material and variation of the filler content. Solyco has demonstrated the high potential of TECC-Wire [103, 112, 113]. Initial tests connecting different types of solar cells using TECC-Wire technology have shown similar performance as interconnections with soldered flat wires, as confirmed by EL- and IV-measurements [103]. However, challenges arose during preliminary thermal cycling tests (TC). A notable degradation of up to 10 % after 100 hours of thermal cycling was observed for manually contacted cells. Cells that were contacted using a semi-automated stringing machine, however, demonstrated a significantly lower degradation rate of approximately 2 % in these tests [103]. These first trials were performed using a Cu-wire coated with a thermoplastic highly filled with carbon black. The electrical conductivity using this type of filler is limited to around 1 S/cm, and the inherent light absorption of the black wire also reduces the efficiency of the modules.

These results underscore that this promising cell interconnection concept requires substantial improvement based on a deeper understanding of the cell interconnection process and the required specifications for the thermoplastic and conductive wire coating [103]. Several aspects have to be considered working towards a robust cell interconnection process resulting in long-lasting modules with

high efficiency. The melting temperature of the thermoplastic matrix sets the processing temperature, while its chemical composition and layer thickness control the adhesion between the cell surface and the copper (Cu) wire. Not only the filler content, also the shape and surface properties of the conductive particles determine the microstructure of the polymer/filler composite and hence the electrical conductivity of the coating layer. So far, it is not even clear what minimum electrical conductivity is sufficient for a reliable cell interconnection. The long-term durability of the cell interconnection is not only determined by the properties of the polymer matrix, but also by the compatibility between matrix and filler, i.e. the particles surface properties, potentially appropriate compatibilizer agents have to be added. All these factors need to be thoroughly investigated in order to fully exploit the potential of the TECC-Wire technology.

In order to develop a TECC-Wire based interconnection method capable of competing with industry-standard approaches [90, 160] in terms of efficiency, reliability, and ultimately costs, this study focuses on design and manufacturing of a highly conductive (Ag) filled thermoplastic Cu-Wire coating for the TECC-Wire technology. While this approach may not offer a more cost-effective solution or leads to lower silver consumptions than the previously evaluated carbon black filled system [103], it provides insights into a crucial property of electrically conductive coatings: their conductivity and its impact on the interconnection quality. Highly conductive filler particles such as silver allow for a much higher intrinsic conductivity of the coating layer compared e.g. to carbon black fillers. Moreover, a lower degree of filling content enabled by such highly conductive particles is supposed to yield higher mechanical strength and durability of the interconnection. A deeper understanding of these effects will allow for tailoring wire coating formulations yielding higher efficiency as well as durability, and finally then also lower cost. First, the formulation of the wire enamel, which serves as the precursor for the wire coating, is discussed. The conductive enamel is designed such that it can be applied in a conventional wire coating process, well established e.g. for producing insulating thin wires for electrical coils [154]. The wire coating process involves several crucial steps, as illustrated in Figure 29. The wire enamel consists of three main components: polymer, solvent, and silver particles. This enamel is applied to the wire, and upon heating, the solvent evaporates, leaving a thin thermoplastic coating layer, as shown in Figure 29a). This layer is composed of the non-volatile components of the enamel, primarily the polymer and silver particles. Figure 29b) depicts the wire coating process in detail. The wire, moving at a high speed of up to 800 m/min, passes through a coating nozzle that determines the initial enamel layer's thickness. After application, the wire enters an oven where the solvent evaporates. Following this, a second layer of enamel is applied on top of the first. To achieve the desired coating thickness for the second layer, a coating nozzle with a slightly larger diameter than the first one is used before the wire enters the drying oven again. This method allows for precise control of the total coating thickness by varying the nozzle diameter and the number of coating cycles. An industrial wire coating machine is depicted in Figure 57 of the supplementary information.

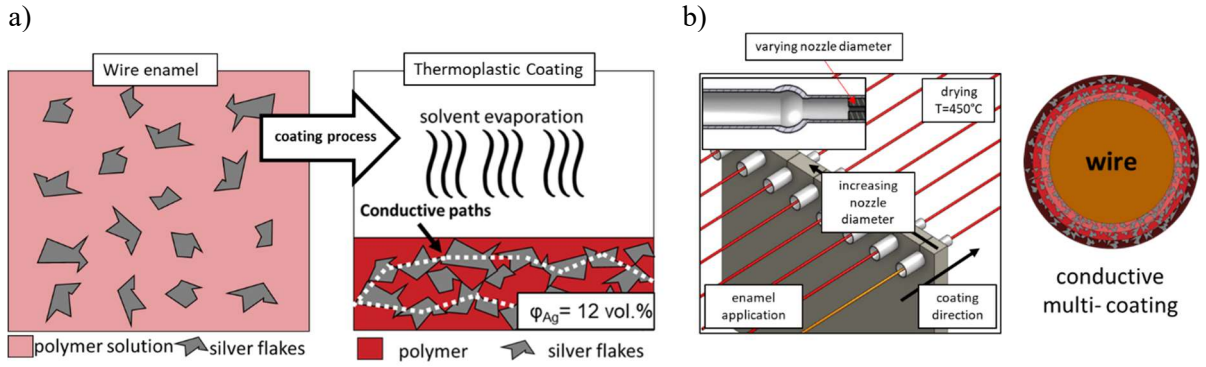

Figure 29 a) The solvent evaporation step during the wire coating process, b) the wire enamel application with layer build-up and an illustration of a copper wire after it passed through multiple coating cycles.

Using wires coated with an Ag-filled thermoplastic polymer through this wire coating method, heterojunction cells were interconnected on a laboratory-scale stringing machine. The study investigated the electrical properties, efficiency, and durability of these modules in damp heat tests. Additionally, the research explored the impact of processing parameters on the overall performance of the modules.

6.2 Experimental section

6.2.1 Formulation of the wire enamel

The Ag-filled wire enamel comprises plate-shaped silver particles Ag Flake Powder Fa-S-12 (DOWA Electronic Materials CO., LTD., Tokyo, Japan) with an average particle size of approximately 2.5 µm. Figure 30 displays the particle size distribution and scanning electron microscopy (SEM) images of the Ag particles.

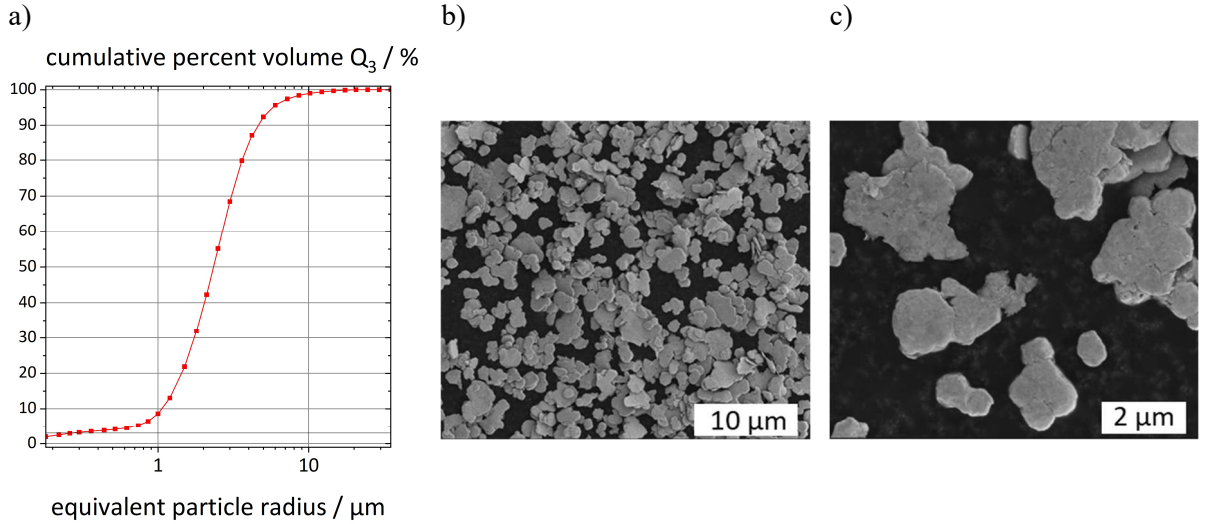

Figure 30 a) cumulative volume distribution as determined by Fraunhofer diffraction. b) and c) scanning electron microscopy (SEM) images of the Ag particles FA-S12.

The Ag particles were suspended in the cresol- and phenol-free Voltatex® 8609 ECO bonding wire enamel (Axalta Coating Systems & Co. KG, Wuppertal, Germany), which contains approximately 10 vol% of a thermoplastic polymer with a melting temperature of approximately 180 °C. The remaining components are a mixture of organic solvents, primarily benzyl alcohol. The ionic liquid (IL) 1-Butyl-3-Methyl-imidazoliumiodide (Carl Roth, Karlsruhe, Germany) is added in varying quantities as conductivity enhancing agent. To facilitate precise dosing, a 25 wt% solution of the IL is prepared using

the organic solvent dimethyl sulphoxide (DMSO) ≥ 99.5 % (Carl Roth, Karlsruhe, Germany). First the required amount of Ag is mixed with the wire enamel. The mixing process involves a three-step mixing and cooling cycle, each lasting 2 minutes at 2000 rpm in a non-contact planetary mixer SpeedMixer™ DAC 150.1FVZ (Hauschild GmbH, Hamm, Germany). The amount of Ag added corresponds to 12 vol% of the total non-volatile components, which includes the polymer, Ag, and IL. Finally, the IL-DMSO mixture is incorporated into the formulation and mixed for an additional 1.5 minutes at 1700 rpm. The precise compositions of the wire enamel and the resulting adhesives after removal of the solvent, are presented in Table 6, 6, and 7 of the supplementary information.

6.2.2 Rheological characterization of the wire enamel

The viscosity of the enamels was determined at 20 °C. The measurements were conducted using a stress-controlled rotational rheometer (Physica, MCR 501, Anton Paar GmBH, Germany) equipped with a concentric cylinder geometry (inner diameter d = 27 mm, gap width w = 1.13 mm) and the viscosity η was determined in the shear rate range $1\ s^{-1} < \dot{\gamma} < 1000\ s^{-1}$.

6.2.3 Electrical conductivity measurement

The Ag filled wire enamel samples were applied to glass slides in thin layers, followed by a solvent evaporation step on a heating plate at 200 °C for 5 minutes in order to remove all the volatile components. Every sample consists of two layers meeting a total coating thickness of approximately 70 µm. The coating was cut into strips with a length of 4 cm and a width of 0.5 cm in order to determine electrical conductivity. The actual geometry (length l, thickness t, width w) of each sample was determined precisely using an outside micrometer. The electrical resistance was determined using a four-point probe (RLC 200, Grundig, Germany). From the electrical and geometrical data, the electrical conductivity was calculated according to equation (3).

6.2.4 Wire coating process

In order to apply thin layers of the thermoplastic and electrically conductive coating to the wire (d_{wire} = 300 µm), two different approaches were used. For the first approach, a laboratory scale wire coating machine was customized in order to test the processability of the wire enamel using small sample volumes of approximately 50 milliliters per test run. The coating speed was adjusted to 6.9 m/min, while the coating temperature was set to 600 °C. The initially coating nozzle had a diameter of 370 µm. After every coating cycle, a nozzle with a 5 µm larger diameter was employed. In total, nine coating layers were applied resulting in a final dry layer thickness of about 24 µm. A more detailed description of the coating machine is displayed in Figure 20.

For the second approach, we utilized the industrial wire enameling machine MAG HE 4+5 (MAG machines GmbH, Deutschlandsberg, Austria), provided by Axalta Coating Systems. The Ag-filled Voltatex® 8609 ECO bonding wire enamel was applied to the copper wire (d_{wire} = 300 µm) at coating speeds between 40 and 60 m/min and an oven temperature of approximately 450 °C. In total ten layers were applied to meet an average coating thickness of approximately 18 µm. The required volume for one test run is approximately 2 liters. A more detailed description of the wire coating process is displayed in Figure 57 of the supplementary information.

6.2.5 Solar cell interconnection

For the interconnection of cells, a customized laboratory scale semi-automated stringer was used [113]. The stringer enables to contact cells reproducibly with sufficient spatial accuracy, temperature, time and pressure control. The contacting temperature was always kept at 190°C and the contacting time at 4 sec. Contacting pressure was varied from minimum 210 to maximum 910 mbar. Current-Voltage-Measurement (IV) electroluminescence (EL) imaging, and peel tests are used to evaluate the results.

6.2.6 Peel test

The tensile strength testing machine BZ1.0/TH1S (Zwick/Roell, Ulm, Germany) was used for the 180° peel test. The traverse speed was set to 26 mm/min. The recorded data was normalized to the diameter of the round wire (300 µm).

6.2.7 Damp heat test

Before conducting the damp heat test (+85 °C at 85 % r.h.) for 1000 hours (DH1000), the contacted solar cells were encapsulated in glass/glass configuration using the polyolefin TR02BA-50T (Mitsui Chemicals, Tokyo, Japan) as encapsulant foil. The samples were laminated using an industrial laminator type S1815 (3S Swiss Solar Solutions AG, Tun, Switzerland). The lamination temperature was 155 °C for 20 min. The test procedure for the DH test is described in international electrotechnical commission (IEC) 61215-2 for terrestrial photovoltaic (PV) modules [161].

6.3 Results and discussion

6.3.1 Electrical conductivity of the wire coating

In order to reach a high electrical conductivity of the wire coating an Ag based formulation was developed. The addition of the iodine salt 1-Butyl-3-Methyl-imidazolium iodide (IL) was employed to decrease the percolation threshold from 20-30 vol% typical for commercial electrically conductive adhesives (ECA) [18] to 12 vol%, thus enhancing the adhesive's conductivity at low filler content [35, 107]. Corresponding results are presented in Figure 31a), where the conductivity κ is plotted against the IL-Ag volume ratio at a constant Ag volume fraction of 12 vol%. Based on the IL concentration, the formulations can be categorized into three regimes. The first regime, with an IL-Ag volume ratio of 0.00 and 0.02, yielded a dry film conductivity ranging from 10^{-4} to 10^{-5} S/cm. The second regime, with a ratio between 0.03 and 0.04, demonstrated a conductivity of approximately 480 ± 100 S/cm. The third regime, with IL-Ag volume ratios exceeding 0.06, showed a conductivity of around 3 ± 1 S/cm. Figure 31b) illustrates the impact of adding an iodine salt to silver particles coated with a fatty acid surface layer. The iodine anion replaces the fatty acids on the Ag particles, lowering their dispersibility in the organic composite and causing aggregation of the silver particles. The different microstructures (degree of aggregation) corresponding to the three regimes with different iodine concentration are directly visible in the SEM images shown in Figure 31c). In the first regime, where no or low amounts of iodine were present, the particles were uniformly distributed due to the fatty acid coating, resulting in only few particle-particle contacts and low conductivity. In the second regime, with intermediate iodine concentration, the partial replacement of fatty acids by iodine induced microphase separation, leading to the formation of a network of electrically conductive paths. With further increases in iodine concentration, more fatty acids were replaced by iodine, resulting in the formation of larger, more compact Ag agglomerates, which reduced the total number of percolating conductive paths and consequently decreased the overall sample conductivity. Infrared spectroscopy (IR) and a thermogravimetric analysis (TGA) were employed to confirm that IL changes the Ag particle surface. Corresponding results are displayed in Figure 12. Based on these findings, the formulation with an IL-Ag-volume ratio of 0.04 was selected for further testing due to its high conductivity of approximately 480 S/cm.

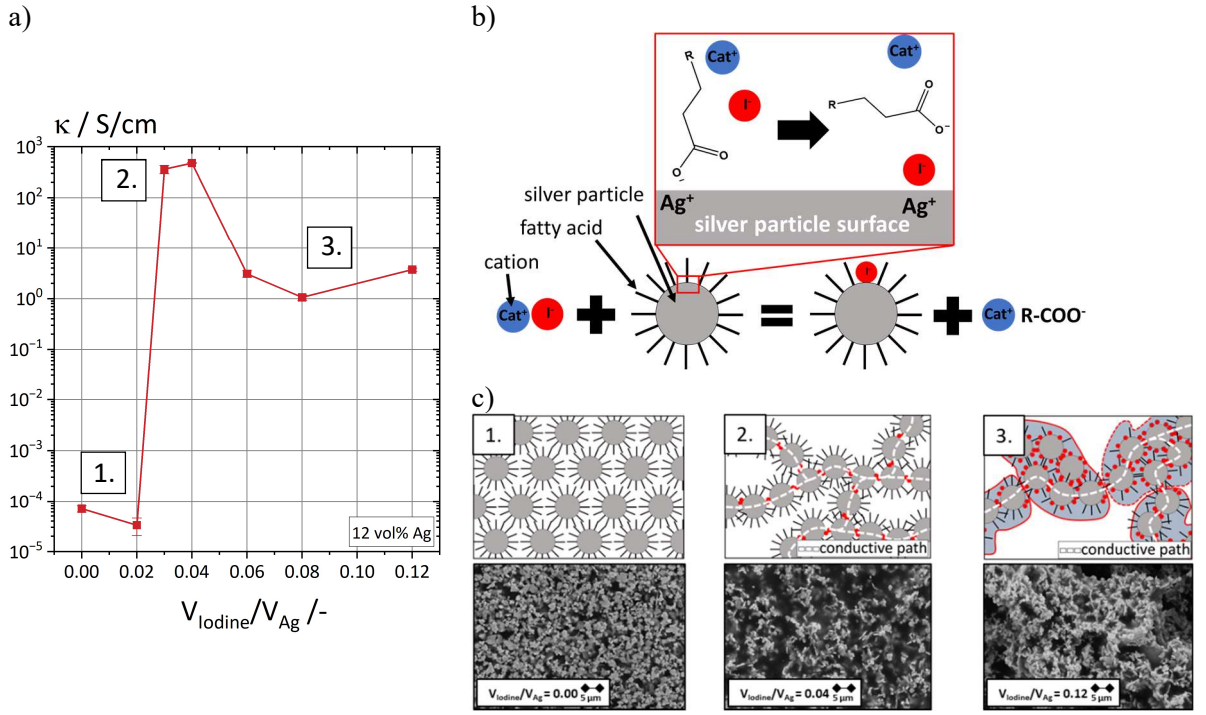

Figure 31 a) Electrical conductivity κ in S/cm plotted against the IL-Ag-volume ratio (V_{IL}/V_{Ag}) of the coating. All samples contain 12 vol% Ag. b) The chemical reaction of an iodine salt with a fatty acid coated Ag particle. c) The proposed change in microstructure of an Ag filled adhesive after adding different amounts of an iodine salt including SEM images of the surface of coatings with 12 vol% Ag and an IL-Ag-volume ratio of 0.00, 0.04 and 0.12.

6.3.2 Wire enamel viscosity and coating quality

To ensure high-quality wire coating, it is crucial to optimize the rheological properties of the wire enamel. To achieve this, multiple wire enamel samples with different polymer concentration were prepared. All samples contained 12 vol% Ag, referring to the non-volatile components of the formulation, and had an IL-Ag volume ratio of 0.04. Viscosity measurements were conducted for samples with polymer fractions of 10, 13, 14, 16, and 18 vol%. Simultaneously, wire coating trials were performed using the laboratory-scale coating machine (see supplementary information, Figure 20), and the coating surface quality was evaluated using light microscopy. Figure 32a) shows that all formulations exhibit Newtonian behavior at shear rates above 10 s^{-1} and the viscosity at a shear rate of 100 s^{-1} was considered to compare the samples, since typically this is the average shear rate during the wire coating process. Figure 32 b) showcases the quality of the wire coatings, indicating that a low-viscosity wire enamel yields significantly higher surface quality compared to a high-viscosity one. The wire coated with the 10 vol% polymer enamel exhibits excellent surface quality with almost no defects along the wire. In contrast, the wire coated with the 18 vol% enamel displays an uneven surface structure with numerous air inclusions throughout the coating.

a)

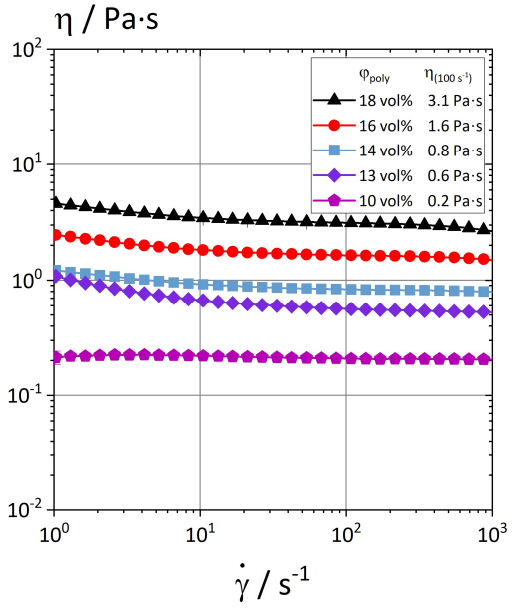

b)

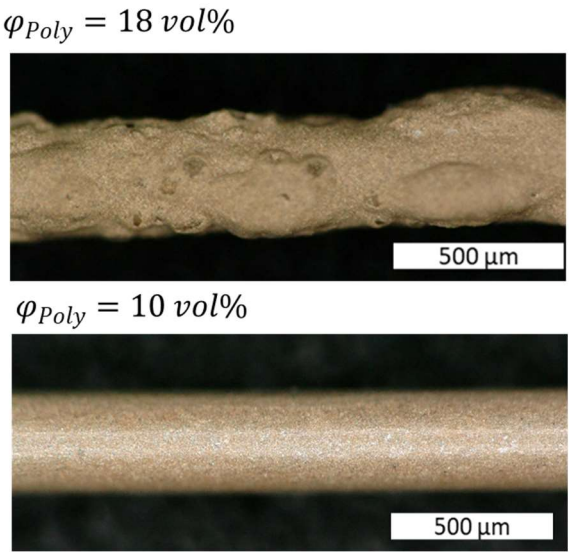

Figure 32 a) Viscosity η in Pa·s plotted against the shear rate $\dot{\gamma}$ in s^{-1} for Ag filled wire enamels with different polymer concentrations. All samples contain 12 vol% Ag regarding all the non-volatile components and an IL-Ag-volume-ratio of 0.04. b) Magnified images of coated wires: the top one coated with a high viscosity wire enamel (18 vol%) and the bottom one coated with a low viscosity enamel (10 vol%).

The enamel with a polymer fraction of 10 vol% was selected for performing a multi-layer coating trial using the same laboratory-scale device to evaluate the enamel's suitability for precisely adjusting the coating thickness while maintaining high surface quality. Figure 33a) illustrates the results of a nine-cycle coating trial. The coating nozzle was increased by 5 µm after each cycle starting with a diameter of 370 µm. The data reveals that the coating thickness increases by approximately 2.5 µm with each step until it reaches a final thickness of approximately 24 ± 2 µm after nine cycles. Figure 33b) presents images of the coated wires after zero, six, and nine coating cycles. The results demonstrate good surface quality, even after a significant number of coating cycles. However, some minor air inclusions and craters may occur occasionally (see supplementary information, Figure 62). To mitigate these issues, it is suggested to use an even smaller nozzle diameter increase than 5 µm after each cycle or conducting multiple coating steps with a nozzle with the same diameter, which could potentially yield a smoother coating quality.

After adjusting the electrical conductivity (Ag content and added IL) and viscosity (polymer content) of the wire enamel, an industrial coating trial was carried out to assess the processing capabilities of the system.

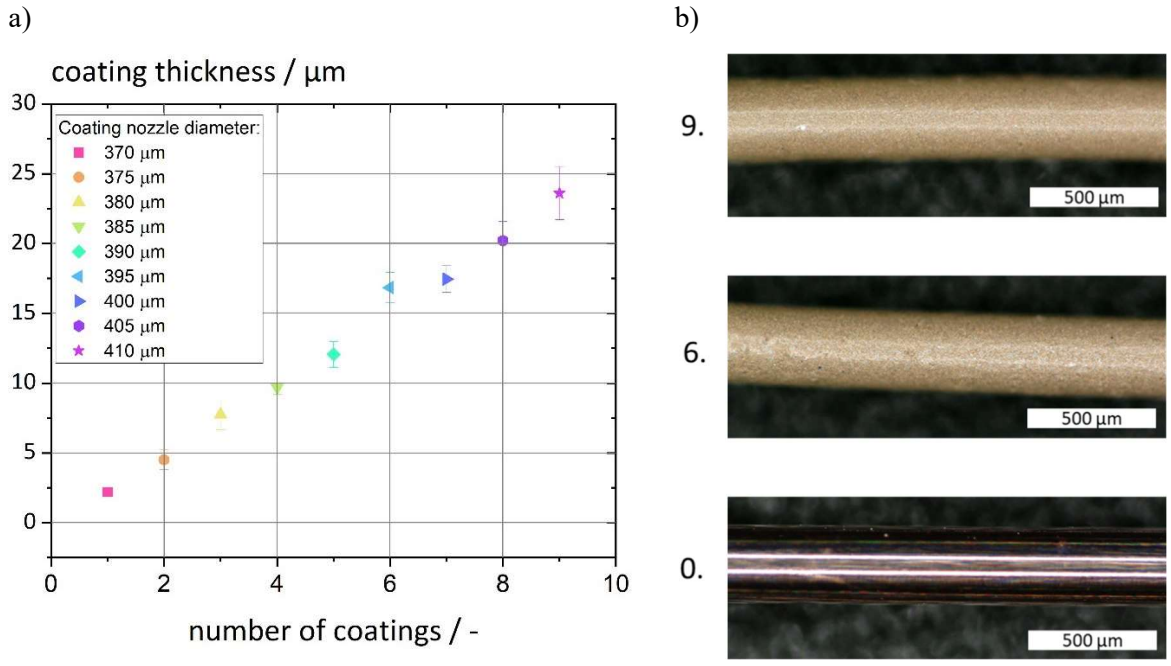

Figure 33 a) The dry coating thickness on the wire plotted against the number of coatings. After each coating cycle the nozzle diameter is increased by 5 µm. b) Images of the copper wire with a diameter of 300 µm after zero, six and nine coating cycles. The enamel with 10 vol% polymer, 12 vol% Ag regarding the non-volatile components and an IL-Ag-volume ratio of 0.04 was used in these trails.

These capabilities are essential to meet the high throughput demands of solar module production. Initial tests involved a 10-cycle multi-coating process at coating speeds ranging from 40 to 60 m/min. Further details are provided in Figure 63 of the supplementary information. It should be noted that since this was an initial trial without optimized coating nozzle selection, the standard deviation in this coating trial is higher compared to the laboratory-scale trials. To address this issue in the future, a more appropriate selection of coating nozzles should be implemented. As indicated in the appendix, the coating trial conducted at a wire speed of 60 m/min demonstrated the best coating quality. Therefore, wires obtained from this specific trial were selected for the subsequent step of contacting and interconnecting solar cells.

6.3.3 IV and EL characterization of TECC-Wire interconnected half-cut M6 SHJ solar cells

To assess the performance of the Ag-based wire coating, half cut M6 SHJ solar cells were contacted using the semi-automated stringing machine developed by Solyco Technology GmbH [103]. Contacting was carried out at both low (210 mbar) and high pressure (910 mbar). The contacting temperature was set to 190°C and contacting time to four seconds. The procedure was followed by an IV and EL characterization. Table 2 summarizes the properties of the Ag-filled coating.

Table 2 Properties of the Ag-filled wire coating.

	Ag-filled system
Electrical conductivity / S/cm	480 ± 100
Coating thickness / µm	18 ± 5
Particle volume fraction / vol%	12

Figure 34 shows the EL images of cells contacted with the Ag-based coated wires at a) low and b) high contacting pressure. All other parameters were kept the same. It is worth mentioning that the semi-automated stringing machine still requires enhancements to apply the wires with an industrially relevant

accuracy. Nonetheless, the obtained results suffice for conducting comprehensive comparisons between cells contacted using different process parameters. Additionally, the cells utilized in this study are intended for a 12-wire interconnection due to the presence of 12 busbar prints. However, the TECC-Wire technology obviates the necessity for busbars, thereby eliminating constraints imposed by the number of busbar prints. In both cases, the EL images reveal a consistently bright illumination, indicating a high-quality contacting process.

a) b)

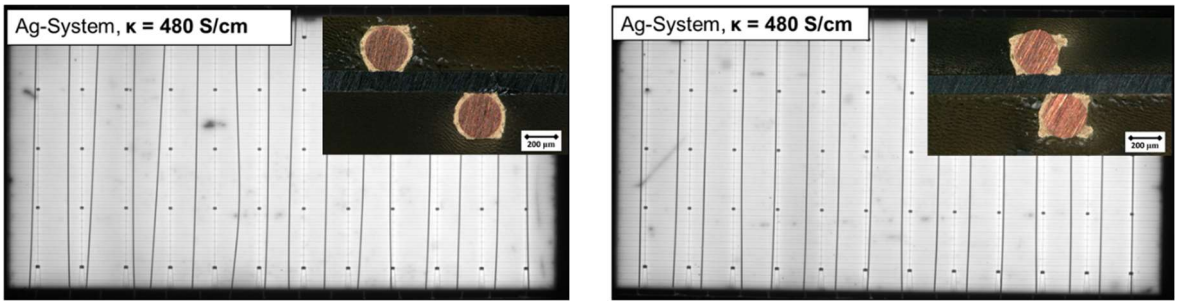

Figure 34 EL image of half-cut M6 SHJ solar cells contacted at a) low pressure and b) high pressure with the highly conductive Ag-filled coating. Both images include a magnified microscopy image of the cross-section of the wire-cell-interconnection.

Table 3 supports this indication. When examining the power output and fill factor closely, the differences between low and high contacting pressure prove to be negligible. This indicates that the TECC-Wire technology using Cu-wires with a silver filled thermoplastic coating is a reliable interconnection process, which does not yield fluctuating product properties when crucial process parameters like the contacting pressure vary. This is a crucial aspect for rapid industrial-scale contacting in the future.

Table 3 Corresponding IV-data of half-cut M6 SHJ solar cells contacted with Ag-filled coated wires at high and low contacting pressure.

Contacting Type	V_{OC} / V	I_{SC} / A	P_{mpp} / W_p	FF / %	V_{mpp} / V	I_{mpp} / A
low pressure	0.74 ± 0.26 %	5.05 ± 0.23 %	3.03 ± 0.38 %	81.25 ± 0.12 %	0.61 ± 0.12 %	4.98± 0.35 %
high pressure	0.74 ± 0.16 %	5.03 ± 0.23 %	3.00 ± 0.74 %	80.61 ± 0.56 %	0.61 ± 0.56 %	4.93 ± 0.49 %

6.3.4 Peel test

In addition to EL and IV measurements the peel strength is another crucial factor to determine the quality of the cell interconnection. Therefore, peel tests of cells contacted with wires coated with the Ag-filled thermoplastic layer were carried out. The results are shown in Figure 35. Both, the systems contacted at low and high pressure display an average peel strength of 1.8 N/mm or higher. The relatively high variation is probably attributed to the limitations of using a customized semi-automated laboratory scale stringer and also by the relatively high variation in coating thickness of the industrial scale coating trial (see supplementary information, Figure 63). Nevertheless, the system remains competitive with other adhesive-based interconnection methods. For instance, ECA-ribbon connections report peel strength values ranging between 0.4 and 1.3 N/mm [33, 34]. Even when compared to soldering, which typically yields a peel strength of approximately 1.5 N/mm [33], the system demonstrates similar performance. It is likely that, in future developments, the coating thickness of approximately 18 µm can be further reduced to minimize material consumption without compromising the mechanical integrity of the cell interconnection. Additionally, the pressure reduction has only a minor impact on the final peel strength, which further supports the hypothesis that the Ag-filled thermoplastic coating layer is a sufficiently effective cell-wire-interconnector for a rapid module production.

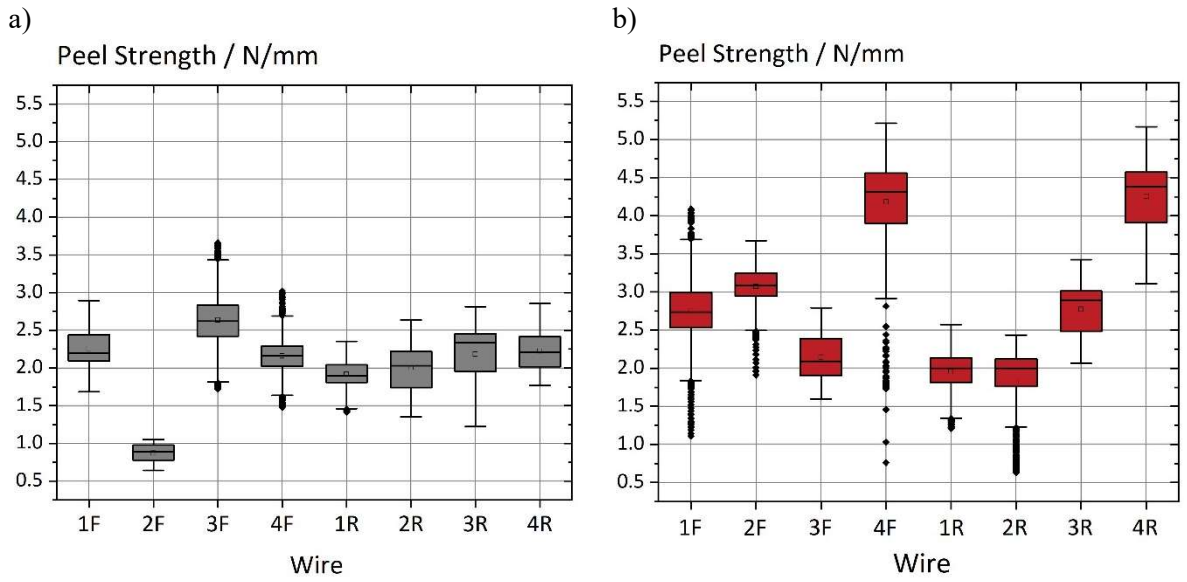

Figure 35 Summary of the peel forces needed to remove the wires from the front (F) and rear side (R) of cells contacted with wires coated with the Ag-filled thermoplastic coating under a) low and b) high contacting pressure.

6.3.5 Damp heat (DH)

The long-term stability of the contacted cells was assessed based on damp heat tests. Figure 36 a) shows the relative IV losses after DH1000 of cells contacted with wires coated with the Ag coating under low and high pressure, b) displays the corresponding EL images before and after DH1000. The data reveals an average power output reduction of less than 5% for all contacted cells, meeting the IEC standards. However, this value seems to be relatively high in comparison to prior experiments where TECC-Wire connected cells endured DH3000 tests with only a 5% degradation [113]. We assume that challenges during the lamination process may have contributed to the higher degradation observed. Unlike earlier tests [113], the glass/glass configured module shown in Figure 64 of the supplementary information did not include a butyl edge sealant. Further experiments with an improved manufacturing process including thermal cycling tests are necessary to gain a more comprehensive understanding of this issue in the future and to determine the specifications for Ag/thermoplastic composites suitable for the production of long-lasting solar modules.

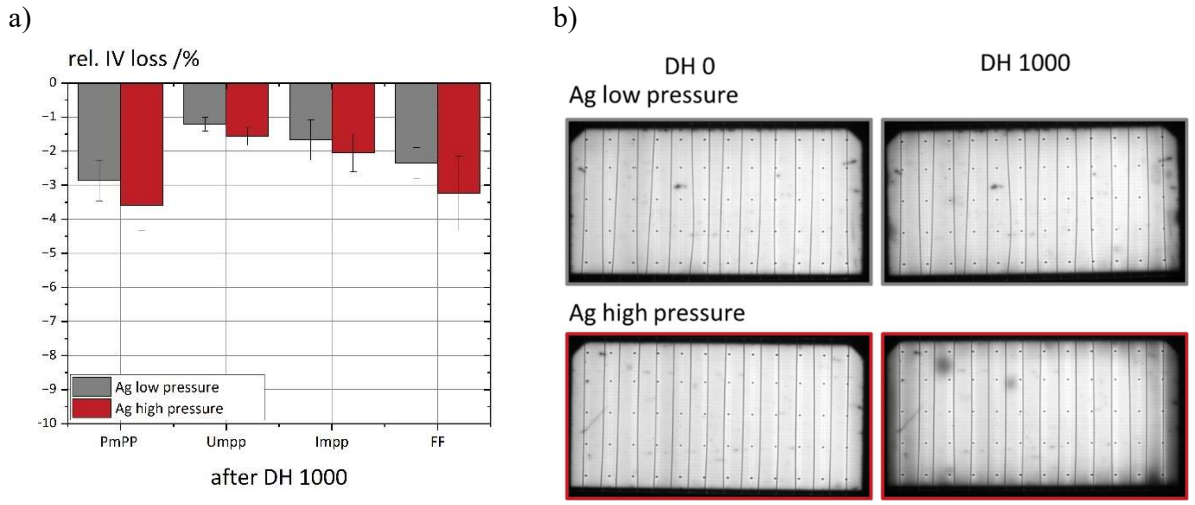

Figure 36 a) IV losses after DH 1000 of cells contacted with wires coated with the Ag-based coating contacted at high and low pressure. b) EL images of low (top) and high (bottom) pressure contacted cells before and after DH 1000.

6.3.6 Silver substitution

To reduce solar cell production costs, Ag should be replaced at least partly in future TECC-Wire developments. Conductivity data obtained in preliminary tests reducing Ag content in the coating by using silver-coated copper and glass particles that today cost approximately 30% less than the pure silver particles are shown in Figure 37a). The graph compares the electrical conductivity κ of different formulations: 12 and 10 vol% Ag flakes, 14 vol% Ag-coated copper flakes (20 wt% of the particles is Ag), 24 vol% Ag-coated glass flakes (40 wt% of the particles is Ag), b) illustrates the corresponding Ag savings compared to the 12 vol% Ag formulation used in the solar cell contacting experiments discussed above. Using Ag-coated materials instead of pure Ag allows for significant Ag savings while maintaining high conductivity. Figure 37c) demonstrates promising wire coating experiments using Ag-coated glass and copper flakes in wire enamels. These results highlight the potential of the TECC-Wire approach. The wire enamel provides a versatile platform for adjusting conductivity and costs according to specific requirements of the interconnection method by selecting the suitable filling material and polymer matrix. Future research will determine whether other, not pure silver particles offer additional benefits.

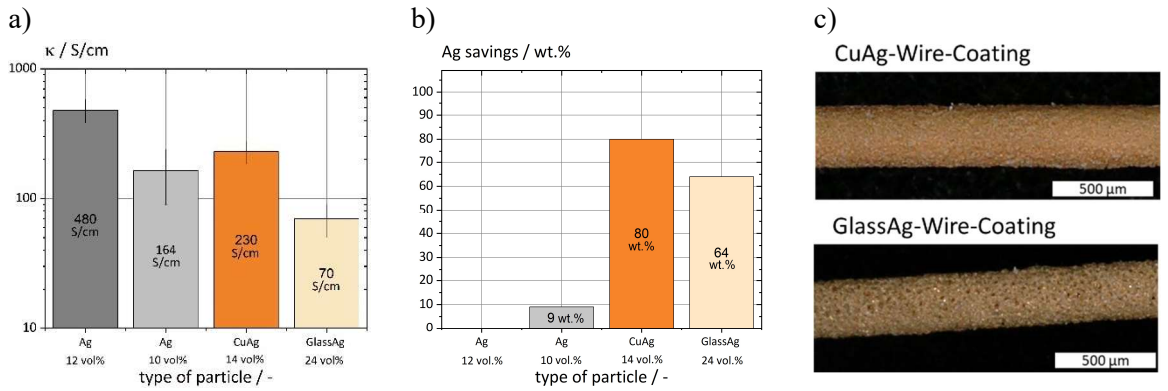

Figure 37 a) Electrical conductivity κ of formulations filled with 12 and 10 vol% Ag, 14 vol% Ag coated copper particles (with an Ag fraction of 20 wt%), 24 vol% Ag coated glass particles (with an Ag fraction of 40 wt%) b) Ag savings in wt% of the different systems in comparison to the formulation wit 12 vol%

Ag. c) First wire coating trials with the wire enamels containing Ag coated copper particles (CuAg) and the Ag coated glass particles (GlassAg).

6.4 Conclusion

The TECC-Wire technology has already shown its potential as a solder-free interconnection method for solar cells [103, 112, 162]. In this study, thermoplastic wire coating formulations with low Ag volume fractions were developed. With these coating layers cell interconnection was demonstrated to be independent of the pressure applied during the cell contacting process in a wide range. Furthermore, preliminary data indicating the high durability and lifetime of modules manufactured utilizing the TECC-Wire concept were obtained.

Using a polyamide-type bonding wire enamel (Voltatex® 8609 ECO) a thermoplastic and electrically conductive wire coating was developed with a melting temperature of T_M = 180 °C and an electrical conductivity of κ = 480 S/cm, at an Ag consumption far lower than that of a conventional electrically conductive adhesive. Adding small amounts of an iodine salt ($V_{Iodine}/V_{Ag} = 0.04$) to the precursor enamel resulted in a percolated Ag particle network in the final coating layer at an Ag fraction of 12 vol% in the dry thermoplastic composite. The viscosity of the enamel was carefully fine-tuned to achieve the desired surface quality of the coating. Subsequently, an initial industrial coating trial was conducted, employing a drying temperature of 450 °C, a coating speed of 60 m/min, and ten coating cycles. This trial successfully yielded a satisfactory surface quality, enabling solar cell interconnection experiments. The resulting layer thickness of the Ag-filled system on the copper wire (d_{wire}= 300 µm) was about 18 µm. Round wires coated with the Ag-based conductive thermoplastic composite were bonded to half-cut M6 SHJ solar cells, applying two different pressures (210, 910mbar) while keeping temperature (190°C) and contacting time (4 s) constant using a lab scale stringing machine. The performance of the resulting single cell modules was evaluated by means of IV and EL characterization, damp heat and peel tests.

The electrical and mechanical properties of the contacted cells turned out to be pressure independent. Power output and EL-images remained unchanged with varying contacting pressure, indicating that this kind of wire is a promising candidate for establishing a robust industrial scale cell interconnection process based on the TECC-Wire technology.

Since silver is a precious resource, first experiments were conducted further reducing the Ag content in the coating layer by replacing the Ag particles with Ag-coated copper and glass flakes. These systems reduce the Ag consumption by 80 wt% and 64 wt%, respectively, in comparison to the system with 12 vol% pure Ag. With these formulations an electrical conductivity of approximately 230 and 70 S/cm could be achieved, respectively. Both systems also showed good results in first wire coating trials. The suitability of these new formulations for the TECC-Wire design will be determined through solar cell contacting trials and long-term stability tests in the future.

The research presented here delivered valuable new insights into the formulation of electrically conductive wire coatings for the TECC-Wire interconnection concept. It can be used as a baseline for future research addressing the relevance of filler type and content, but also polymer type, melt viscosity and wettability. The great versatility of the TECC-Wire concept combined with a well-established high throughput wire coating process shows high potential of becoming a relevant interconnection technology for solar cells in the future.

6.5 Acknowledgements

This work was partly funded by the German Federal Ministry of Economics and Climate Action (BMWK) within the framework of the Zentrales Innovationsprogramm für den Mittelstand (ZIM) under grant number KK5015204BS1. We thank Stefan Ricken, Dirk Böhme and Quoc Anh Nguyen for the

support with material and for conducting the industrial scale coating trials at Axalta Coating Systems (Wuppertal, Germany).

Chapter 7 Summary

As advancements in the photovoltaic and smart technology sectors accelerate, the demand for more sophisticated components continues to grow. Electrically conductive polymer composites, which can be tailored to various application requirements - including process temperature, flexibility, durability, and wettability - are increasingly being explored. Simultaneously, the consumption of rare elements like silver is becoming a significant concern. This thesis explores strategies to reduce silver consumption in polymer-based components and proposes new application methods for interconnecting solar cells and enhancing smart technologies.

Chapter 4 explores the impact of iodine salts on the microstructure and functional characteristics of dry silver-filled polymer films, as well as the flow behavior of their precursor suspensions containing silver particles in TPU/DMSO solutions. Additionally, it introduces a more efficient production method for these materials. The iodine salts IL, KI, and NaI effectively removed surface lubricants from the silver particles. Thermogravimetric analysis showed that treated particles exhibited lower mass loss compared to untreated ones, while infrared spectroscopy confirmed the elimination of carboxylate groups. Adding IL, KI, and NaI to the silver-filled TPU/DMSO solutions led to a significant transformation in flow properties, shifting from a predominantly viscous nature to a strongly viscoelastic, gel-like, or pasty consistency. This change was marked by the emergence of a yield stress (σ_y) and pronounced shear-thinning behavior at stress levels exceeding σ_y. Notably, this alteration in flow behavior was independent of the specific iodine salt used, with no systematic differences observed between IL, KI, and NaI.

The electrical conductivity of the dry Ag/TPU composite films derived from these suspensions also depended strongly on the normalized iodine concentration, yet no consistent variation was found based on the type of iodine salt used. Scanning electron microscopy images of Ag/TPU composites with 20 vol% silver and different IL, KI, and NaI concentrations showed enhanced particle aggregation and the formation of microheterogeneities. At intermediate iodine concentrations, the aggregates were smaller - approximately 10 µm - promoting the formation of numerous conductive pathways and significantly improving electrical conductivity. Beyond the known advantages of iodine treatment - such as removing insulating lubricant layers, reducing silver oxides, enabling UV-induced silver nanoparticle formation, and enhancing oxidation stability via Ag/AgI nanoparticle formation - the findings presented here provide new insights into the critical role of iodine salts in Ag-filled TPU/DMSO solutions and their corresponding dry polymer composites. Specifically, iodine salts play a key role in influencing microstructure and particle network formation, allowing precise control over the flow properties of polymer solutions and the electrical conductivity of dry films.

In summary, Chapter 4 offers valuable knowledge on using iodine salts to fine-tune the microstructure and electrical performance of Ag-filled polymer films while also optimizing their wet-processing properties for numerous applications. Some examples of using this technique are presented in Chapter 5 and Chapter 6.

Chapter 5 presents an alternative method for the production of electrically conductive nylon yarn that is designed for upscaling to commercial production capacities. The approach is inspired by the industrial production of insulated copper wire. To demonstrate feasibility, a laboratory-scale coating machine was built, applying coatings at a coating speed of 2.8 m/min. The conductive ink consists of Platamid M1276

F dissolved in ethanol with suspended silver flakes (D_{50} = 2.5 µm). To improve the electrical conductivity, the ionic liquid (1-butyl-3-methyl-imidazolium iodide) was added to modify the microstructure of the silver particles as described in Chapter 4.

After drying, the coating achieved a conductivity of 812 S/cm. The ink viscosity required careful adjustment to ensure smooth coatings. A 12 wt% polymer concentration gave optimal results, with a coating thickness of approximately 17 µm after five coating cycles and a resistivity of 7.5 Ω/cm. Durability tests showed small increases in resistance after four washing and after 3000 bending cycles, confirming stability for textile applications. Initial tests explored the yarn's potential for capacitive pressure sensing. A simple two-yarn sensor detected pressures from 1 to 20 kPa with a sensitivity of approximately 10^{-3} kPa^{-1} and a response time of 223.6 ms. It maintained accuracy even after 1,000 sensing cycles. A 5 × 5 yarn array successfully detected spatial pressure variations, and further resolution improvements are possible with finer spacing and/or thinner yarn diameters.

This research provides the basis for industrial-scale production of conductive yarns, potentially reaching speeds of around 800 m/min for mass production. The findings pave the way for low-cost conductive yarns, enabling broad applications in smart textiles for wiring and sensing.

In addition, in Chapter 6, iodide-induced microphase separation was used to develop a thermoplastic, electrically conductive wire coating with a low Ag content, enabling low temperature (< 200°C) solar cell interconnection. Initial tests also indicated high durability and good long-term performance of single cell PV modules using the TECC wire concept.

A thermoplastic wire coating was formulated using Voltatex® 8609 ECO, (T_M = 180 °C) and a conductivity of 480 S/cm, with significantly lower Ag consumption than conventional adhesives. The addition of a small amount of the ionic liquid (1-butyl-3-methyl-imidazolium iodide, V_{IL} /V_{Ag} = 0.04) facilitated Ag network formation with only 12 vol% Ag. The viscosity of the enamel was fine-tuned for optimal surface quality, and industrial coating trials successfully produced uniform coatings that enabled solar cell interconnection experiments. Coated wires were bonded to half-cut M6 SHJ solar cells, and IV, EL, damp/heat, and peel tests confirmed stable electrical and mechanical performance over varying contacting pressures. To further reduce Ag usage, Ag-coated copper and glass flakes replaced pure Ag, reducing silver content by 80 wt% and 64 wt%, respectively, while achieving conductivities of approximately 230 and 70 S/cm. Both formulations performed well in initial coating trials and further testing is planned for their long-term viability in TECC wire applications.

This research provides valuable insights into electrically conductive wire coatings and lays the groundwork for future studies on filler type, polymer selection, melt viscosity and wettability. The TECC-Wire concept, combined with scalable wire coating processes, has great potential as an industrial interconnecting technology for solar cells.

In summary, this dissertation provides valuable insights into the mechanisms of incorporating various iodine-based salts into silver-filled electrically conductive polymer composites. This approach is demonstrated in two use cases, where it enhances electrical conductivity by simultaneously reducing the percolation threshold and, consequently, lowering the required silver content. The production of electrically conductive yarn for smart textiles introduces a straightforward, high-throughput method for creating fundamental building blocks to integrate smart capabilities into fabrics. Additionally, the development of electrically conductive coated wires (TECC-Wires) utilizing the iodine-induced silver particle network presents an alternative adhesive-based approach for interconnecting temperature-sensitive solar cells. This method offers a viable substitute for traditional soldering with bismuth, indium, or epoxy-based silver-filled electrically conductive adhesives for interconnecting temperature sensitive solar cells like SHJ cells.

Chapter 8 Outlook

This work not only provides insights into iodine-induced silver particle structure formation but also explores its application in polymer-based electrically conductive composites for smart electronics and as an interconnection method for temperature sensitive solar cells. In both cases, the developed formulations serve as a foundation for further investigations.

The development of electrically conductive yarn can be further explored using more cost-effective materials such as silver-coated copper, glass particles, and carbon-based materials like carbon black or carbon nanotubes. Additionally, by incorporating pigments into the formulation, the yarn could be colored, making it particularly beneficial for textile applications. Moreover, the coating technique presented here enables the stacking of thin layers with different properties, potentially allowing the creation of a capacitive sensor at the yarn scale - thereby increasing the level of integration. Future research should also investigate whether this coating technique, which has proven effective for Nylon yarn, can be applied to other textile materials such as cotton, silk, or polyester, broadening its range of applications.

Regarding the TECC-Wire interconnection method, reducing silver usage is crucial for lowering costs and making it a more affordable alternative for solar cell interconnections. As discussed in Chapter 6, alternative materials should be explored to replace the expensive and relatively rare silver. A promising candidate is cheap and abundant carbon black and graphite. Figure 38 shows the cross-section of a copper wire (d_{wire} = 300 µm) coated with a thin layer (≈ 20 µm) of Voltatex 8609, filled with 11.25 vol% carbon black and 11.25 vol% graphite. The carbon black agglomerates and graphite flakes are clearly distinguishable.

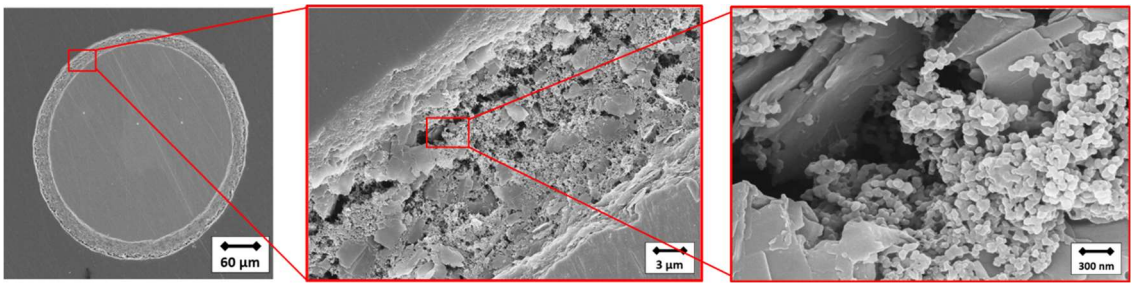

Figure 38 SEM images of the cross-section of a copper wire (d_{wire} = 300 µm) coated with a Voltatex 8609 layer, filled with 11.25 vol% carbon black and 11.25 vol% graphite.

Half-cut heterojunction cells interconnected with these wires exhibited promising performance. This is evidenced by the comparison of the EL images of both the carbon black/graphite and silver-filled systems shown in Figure 39. In both cases, the uniform light distribution indicates good and consistent contact quality. Additionally, IV measurements revealed a fill factor of approximately 80%, comparable to that of solder-based systems [112]. Despite these encouraging results, further testing on full-size PV modules is required, and commercial stringers must be adapted to integrate this new technology.

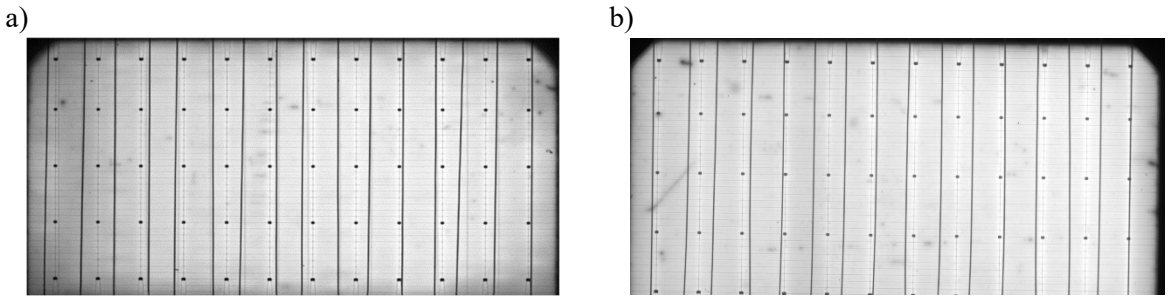

Figure 39 EL images of TECC wire interconnected half-cut SHJ cells using wires coated with different coatings: a) Voltatex 8609 filled with 11.25 vol% Carbon Black and 11.25 vol% graphite (FF = 80.02 %), and b) Voltatex 8609 filled with 12 vol% Ag and a V_{IL}/V_{AG} ratio of 0.04 (FF = 80.6 %).

One potential drawback of substituting silver with carbon black and graphite is their high light absorption, which might slightly reduce cell efficiency. In contrast, a bright wire can reflect light in a way that the light eventually hits the cell's surface [159]. To mitigate this, the carbon black/graphite system can serve as a base layer on the wire, ensuring both mechanically stable and electrically conductive contact. A subsequent thin layer of a brighter, conductive material can then be applied. The wire coating process is perfectly suited for such a multi-coating without making the process more complicated or slowing it down.

Figure 40 shows the coating thickness as a function of the number of coatings. For the first seven coatings - resulting in a total thickness of approximately 17 µm - the carbon black and graphite-based system was used to ensure that enough adhesive is applied to ensure a robust and conductive wire-cell interconnection. The final two coating layers, totaling approximately 8 µm, are silver-filled primarily to achieve a lighter color tone while maintaining electrical conductivity. Although this approach drastically reduces the amount of silver used, it still involves too much silver for commercial applications. Therefore, the pure silver system could be replaced with silver-coated glass or copper particles to further minimize silver usage. Unfortunately, solar cells have not been contacted using the multi-material coated TECC-wire yet.

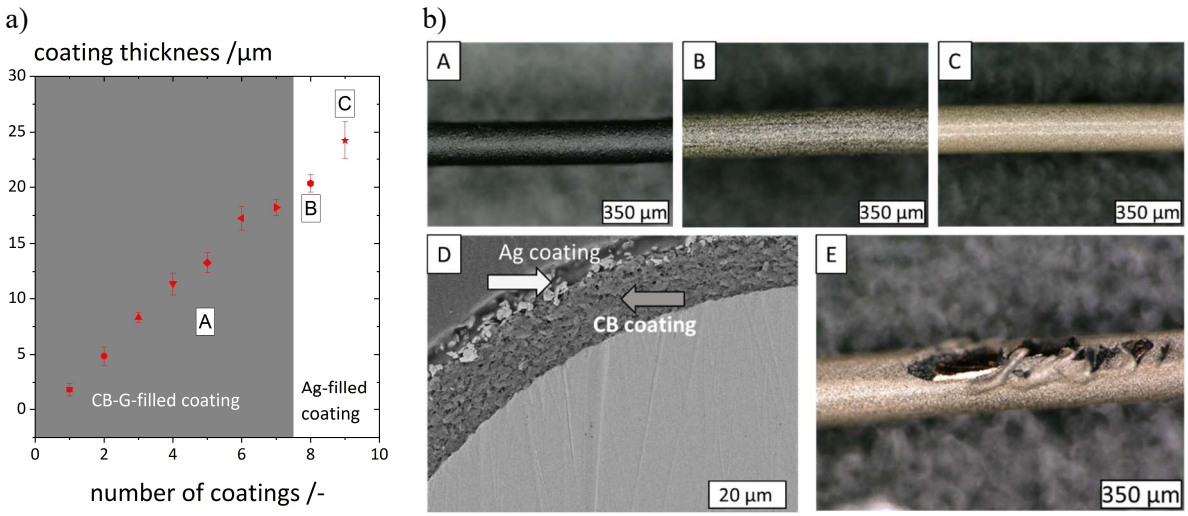

Figure 40 a) Coating thickness (µm) plotted against the number of coating layers. b) Light microscopy and SEM images of the coated wire surface and cross-section after 10 coating cycles.

Initial attempts to contact solar cells using Voltatex8609 filled with 24 vol% silver-coated glass particles have been conducted. The particles themselves contain 40 wt% silver. Figure 41 displays an

electroluminescence (EL) image of the results. Although the light distribution is inhomogeneous, the overall fill factor is approximately 77 %. Increasing the particle fraction slightly might alleviate this issue. In the future, this formulation could serve as a bright top layer (Figure 40) to enhance the wire's reflectivity and thereby increase efficiency but simultaneously decreasing costs in comparison to the silver top layer.

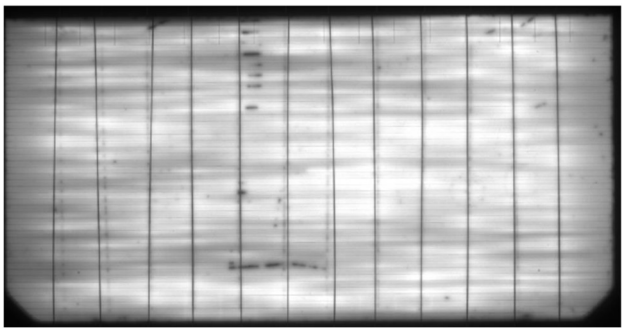

Figure 41 EL image of a half-cut SHJ cell contacted with TECC-wires, using a Voltatex 8609 coating filled with 24 vol% silver-coated glass particles, where the particles contain 40 wt% Ag (FF = 77.3 %).

The TECC-Wire has a notable drawback in terms of material consumption. While the use of carbon black can significantly reduce material costs, a substantial amount of unnecessary material is still used for the wire coating. To ensure a good mechanical and electrical connection between the copper wire and the solar cell, the coating material is likely only required at the interface between the wire and the cell. Therefore, much of the coating is redundant and unnecessarily increases costs. To address this issue, an electrically conductive paste based on a thermoplastic polymer could be applied directly to the solar cell instead of the wire coating, using common PV industry application methods such as screen printing and dispensing. The rheological properties of these formulations can be adjusted to match those of ECAs and metallization pastes typically used in these processes [115, 163].

Another advantage of this approach is that no modifications would be required to existing equipment, such as stringers or cell production machines. Once the paste is applied and the solvent removed, a solid, mechanically stable adhesive line will remain on the cell surface until the temperature is raised above the adhesive's melting point during the interconnection process. Since the adhesive is applied precisely where it is needed, a bare copper wire can be pressed directly into the adhesive without requiring additional ECA or solder paste. Based on this concept, our group has filed a patent (Deutsche Patentanmeldung 10 2024 134 365.6).

The next step is to identify a suitable polymer, solvent, and particle system for application via screen printing and dispensing in thin lines onto the solar cell. This paste should demonstrate adequate conductivity, a melting temperature between 100 °C and 200 °C, and strong adhesion to both the copper wire and the solar cell surface. Figure 42 shows a preliminary test trial as a proof of concept, using a polyamide-based paste filled with silver (Ag).

a) b)

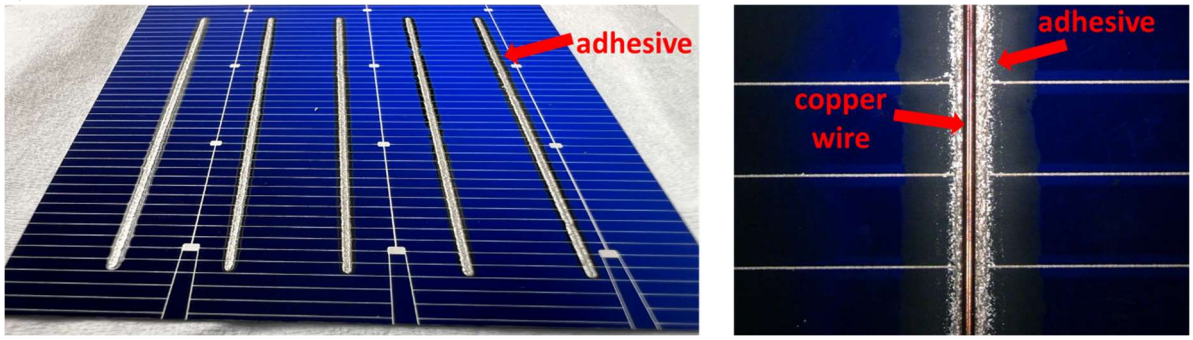

Figure 42 a) A 60x60 mm SHJ cell with five thermoplastic busbar adhesive lines. b) A close-up view of the same SHJ cell, showing the thermoplastic busbar adhesive, with a 300 µm round copper wire pressed into the adhesive.

Chapter 9 Supplementary Information

Table 4 TGA data for the iodide-treated particles at 450 °C.

Particle treatment	Weight loss/%
Untreated	0,98
IL	0,85
KI	0,84
NaI	0,85

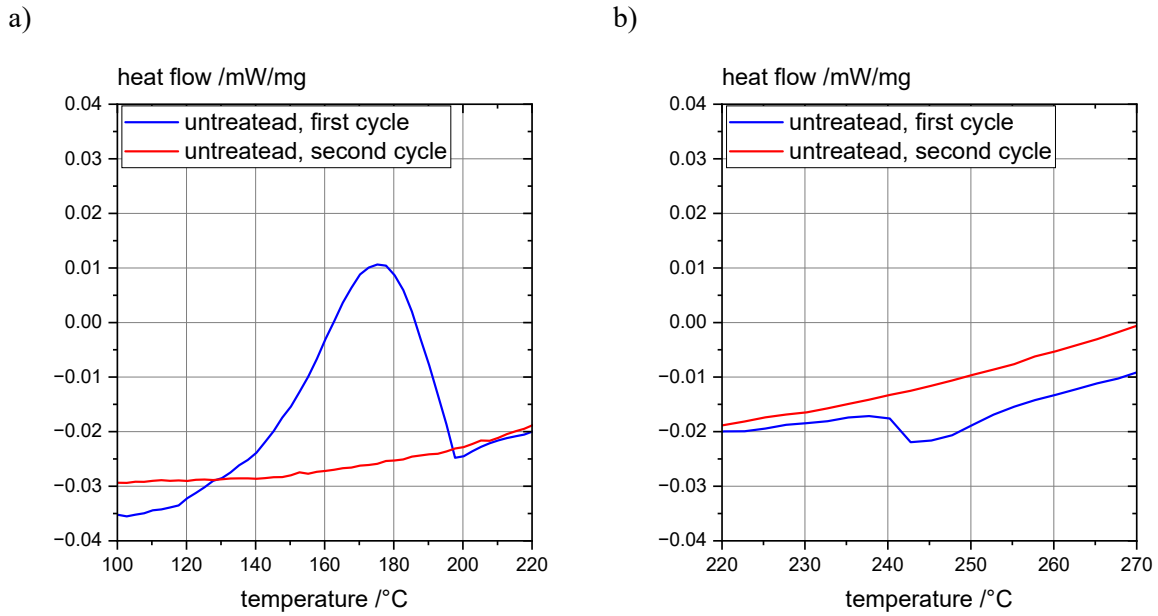

Figure 43 DSC analysis of Ag particles solely washed with ethanol. a) Temperature range between 100 and 220 °C. b) Temperature range between 220 and 270 °C. The blue curve represents the first heating cycle, while the red curve corresponds to the second heating cycle.

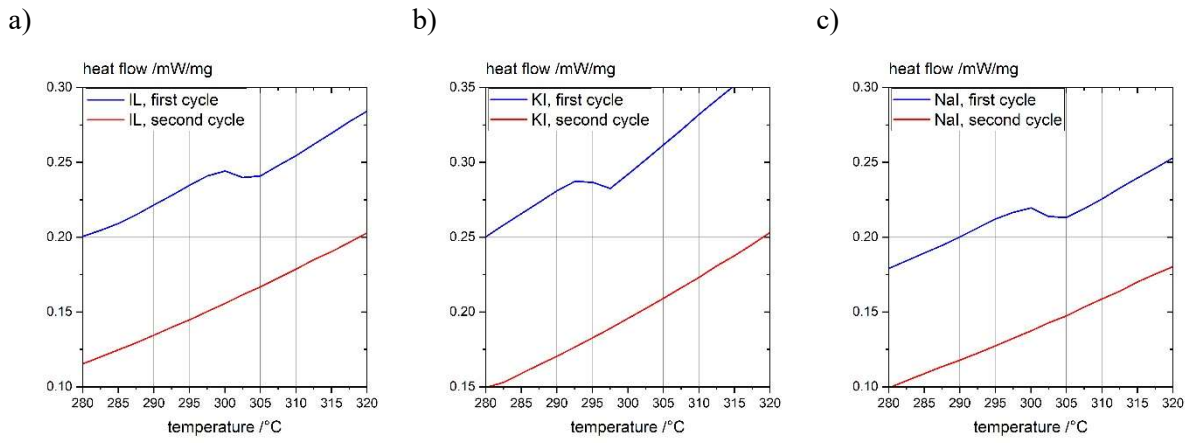

Figure 44 DSC analysis of a) IL, b) KI and c) NaI treated particles for the temperature range between 280 and 320 °C. The blue curve represents the first heating cycle, while the red curve corresponds to the second heating cycle.

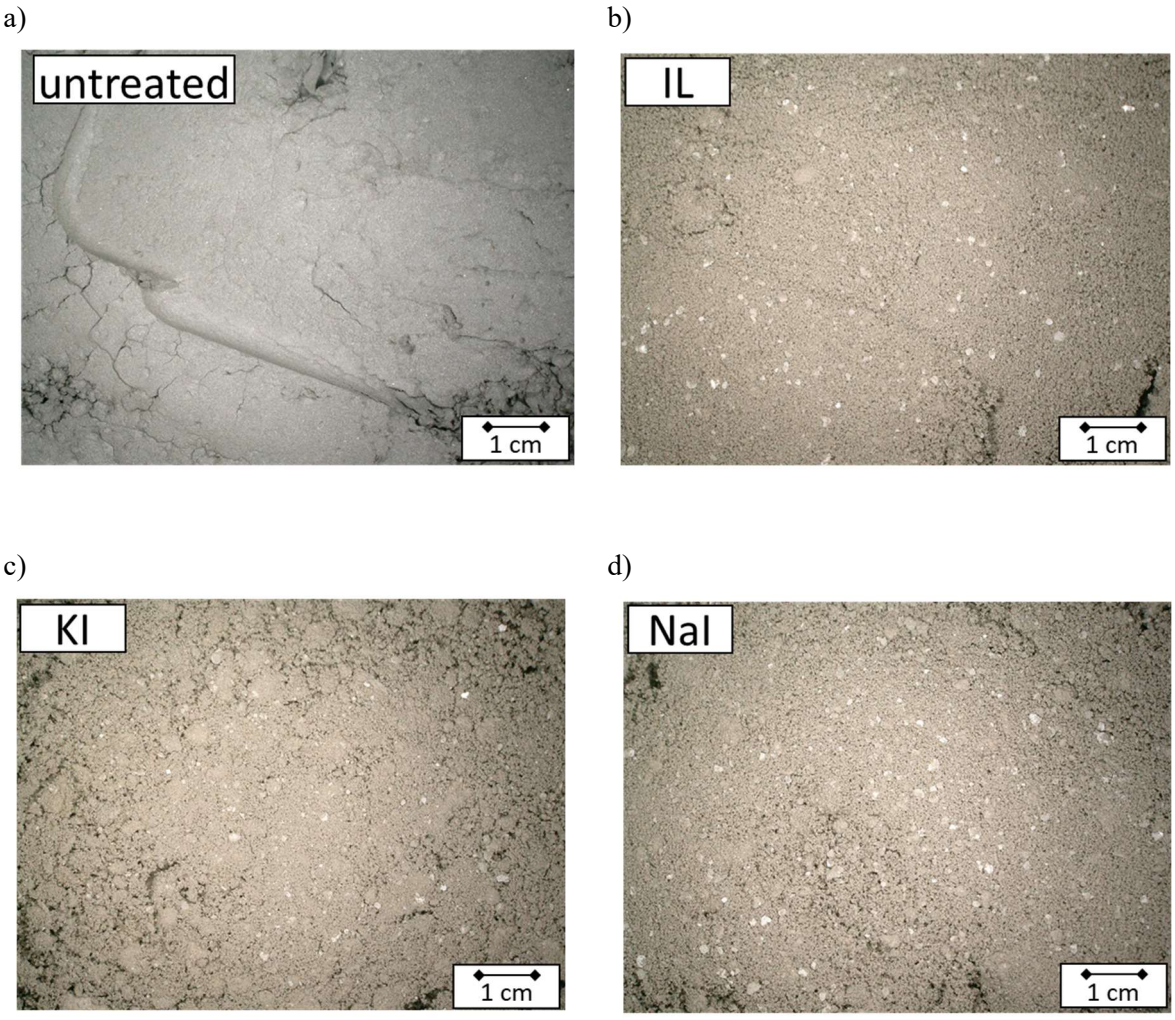

Figure 45 Images of silver particle powder washed with: a) ethanol, and ethanol containing 2.0 mmol of b) IL, c) KI and d) NaI per cm^3 of Ag.

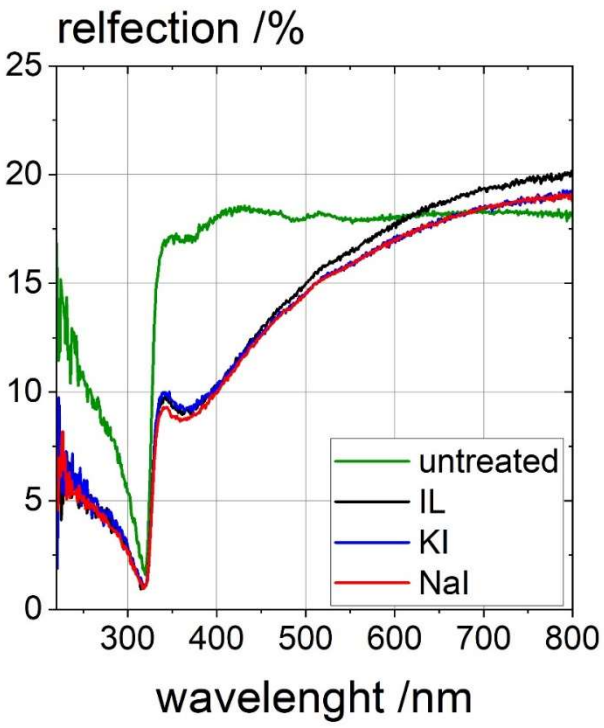

Figure 46 UV-Vis spectra of Ag particles treated with IL (black), KI (blue) and NaI (red) in comparison to untreated particles (green).

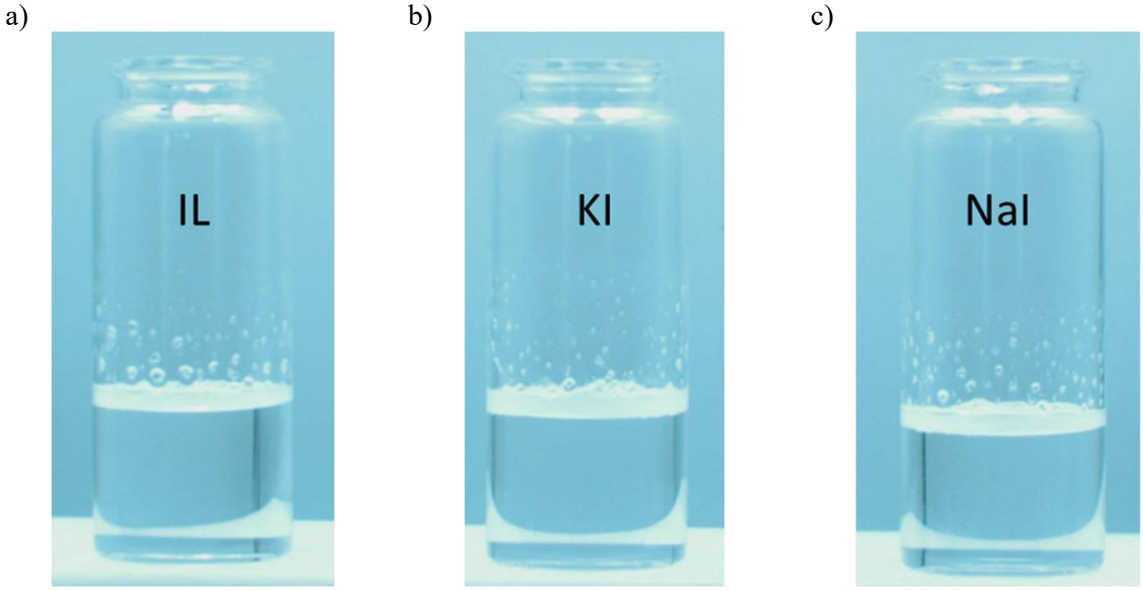

Figure 47 Miscibility trials of 2 g DMSO solutions with additives: (a) ionic liquid (IL), (b) potassium iodide (KI), and (c) sodium iodide (NaI), each mixed into 10 g of the standard TPU/DMSO polymer solution. In all cases, the iodine-containing mixtures exhibited full miscibility with the polymer solution.

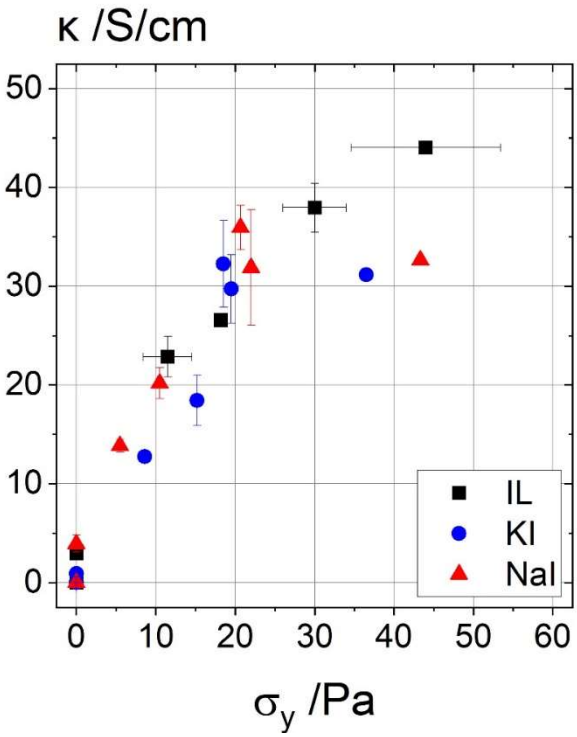

Figure 48 The electrical conductivity κ plotted against the yield stress σy of TPU/DMSO solutions filled with 5.7 vol% Ag and different amounts of IL (black), KI (blue) and NaI (red).

a) b)

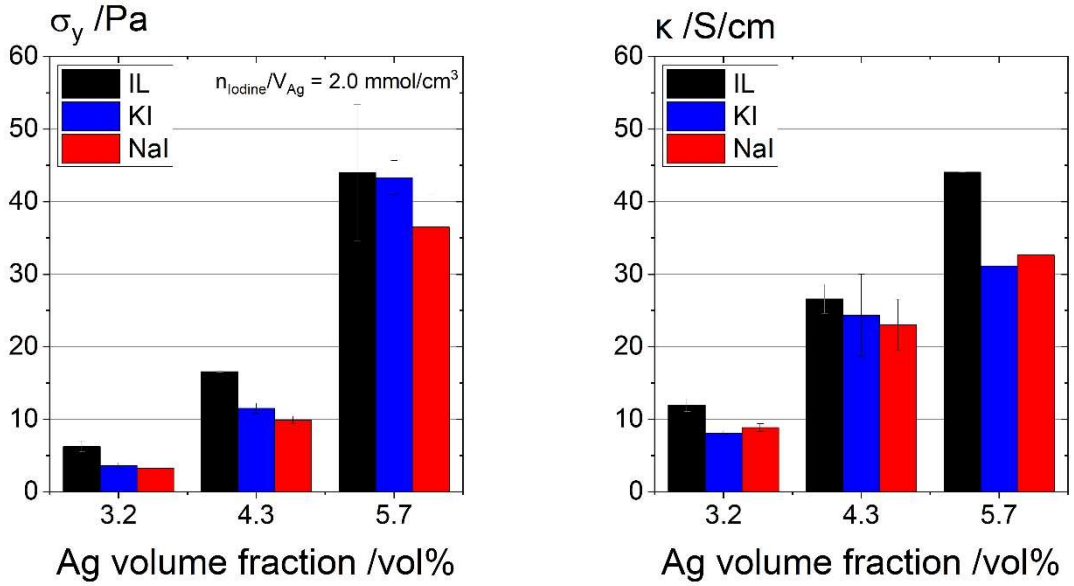

Figure 49 a) yield stress σ_y and b) electrical conductivity κ for TPU/DMSO solutions containing 2.00 $mmol_{Iodine}/cm^3_{Ag}$ of IL (black), KI (blue) and NaI (red) for different Ag concentrations

a) b)

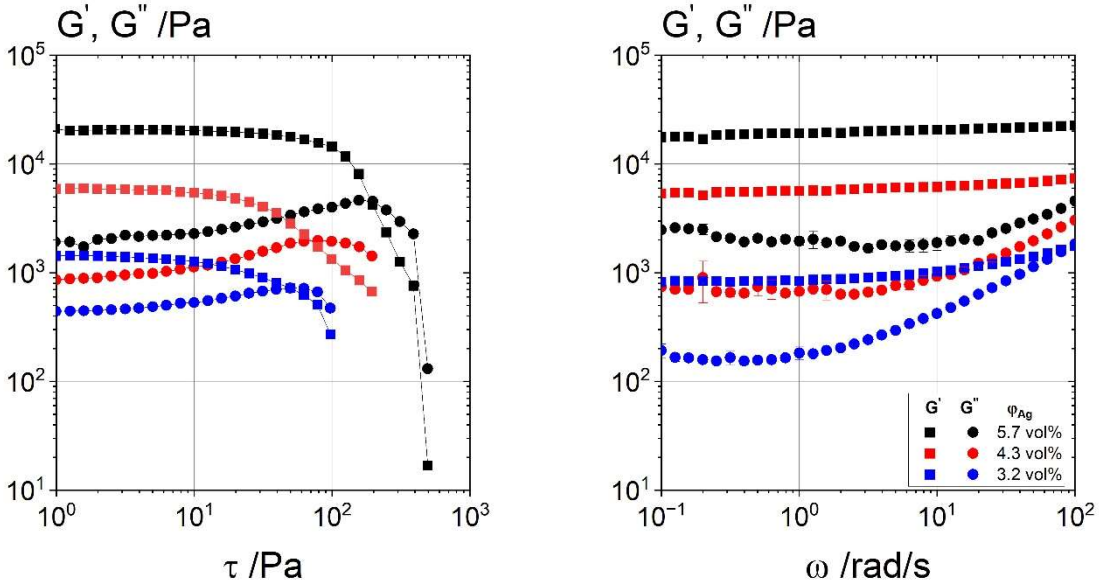

Figure 50 a) Amplitude sweeps at an angular frequency of 10 rad/s and b) frequency sweeps at a stress amplitude of 2 Pa for TPU/DMSO solutions with an IL concentration of 2.00 $mmol_{Iodine}/cm^3_{Ag}$ and an Ag concentration of 5.7 (black), 4.3 (red) and 3.2 vol% (blue).

a) b)

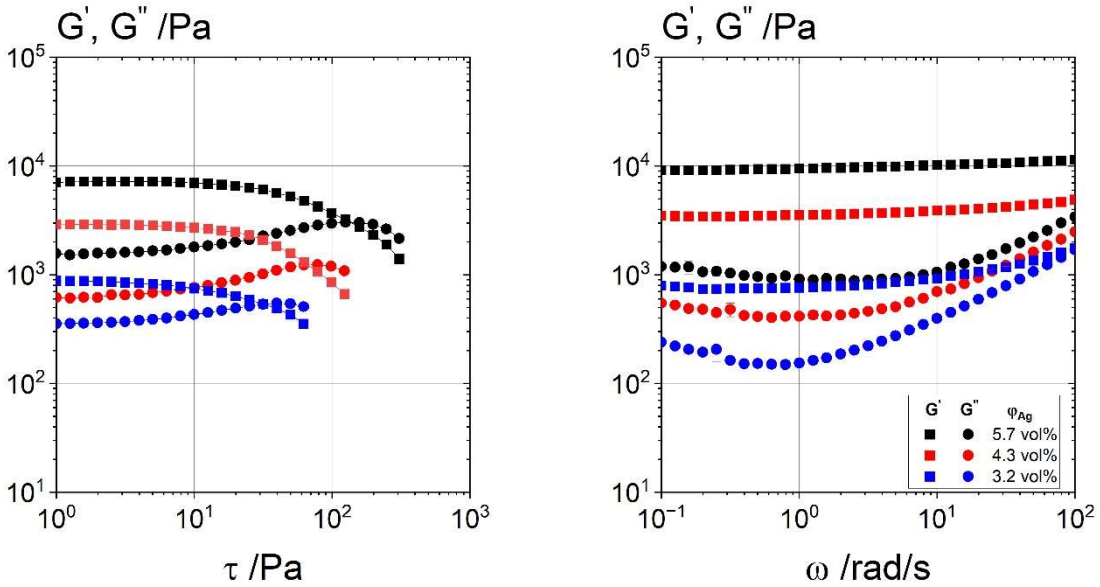

Figure 51 a) Amplitude sweeps at an angular frequency of 10 rad/s and b) frequency sweeps at a stress amplitude of 2 Pa for TPU/DMSO solutions with a KI concentration of 2.00 $mmol_{Iodine}/cm^3_{Ag}$ and an Ag concentration of 5.7 (black), 4.3 (red) and 3.2 vol% (blue).

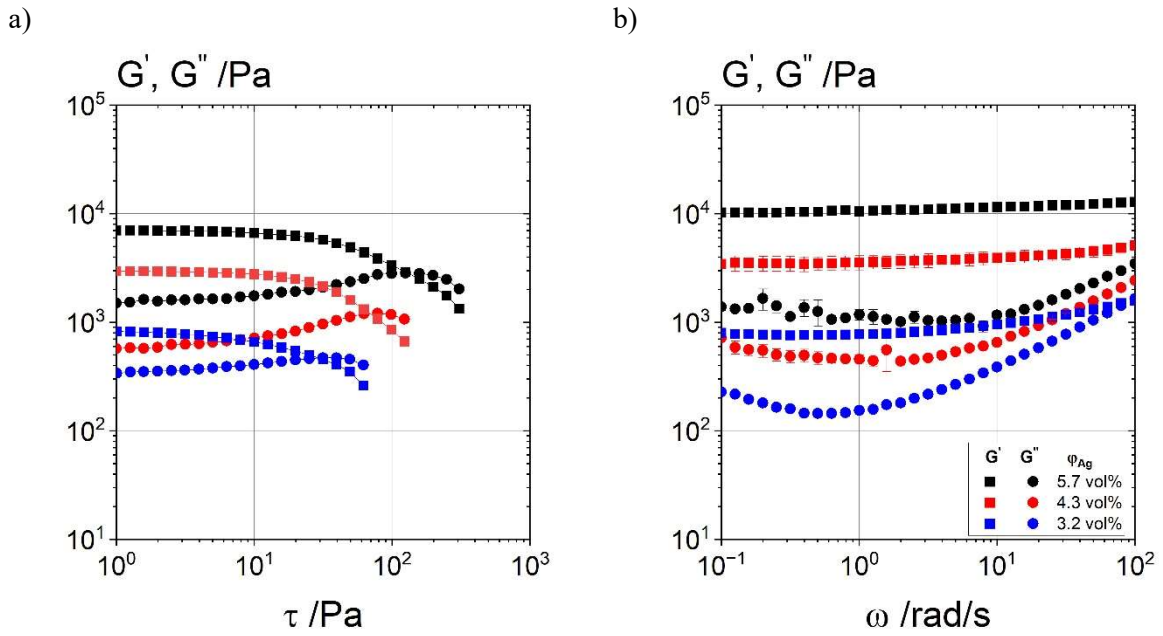

Figure 52 a) Amplitude sweeps at an angular frequency of 10 rad/s and b) frequency sweeps at a stress amplitude of 2 Pa for TPU/DMSO solutions with a NaI concentration of 2.00 $mmol_{Iodine}/cm^3_{Ag}$ and an Ag concentration of 5.7 (black), 4.3 (red) and 3.2 vol% (blue).

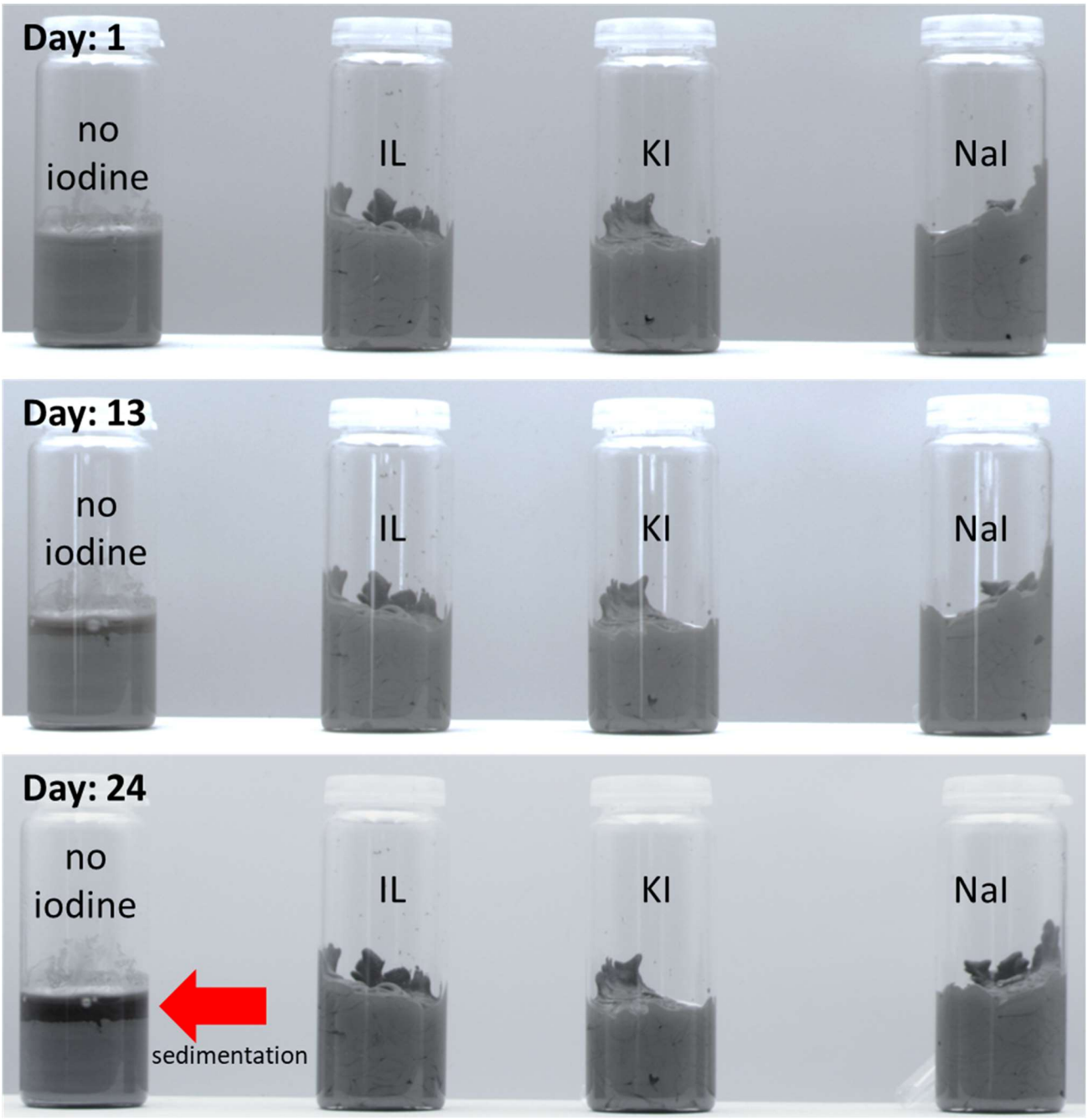

Figure 53 Long-term sedimentation experiment using TPU/DMSO solutions containing 5.7 vol% Ag and 2.00 $mmol_{Iodine}/cm^3_{Ag}$, with various iodide compounds (IL, KI, NaI), compared to a control sample without iodine. The red arrow indicates the sedimentation line of the iodine-free sample. No visible sedimentation was observed in the iodine-containing formulations after 24 days.

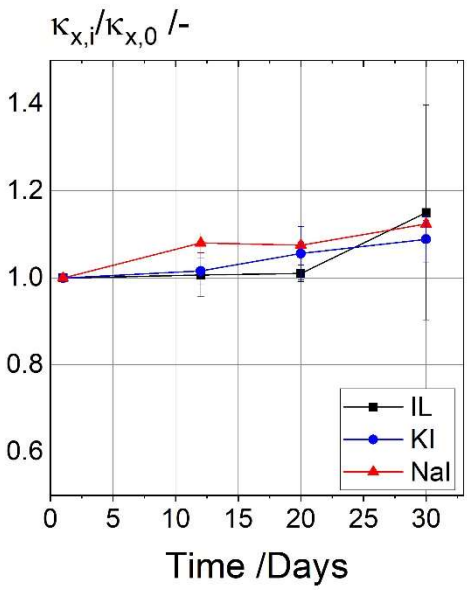

Figure 54 Relative electrical conductivity ($\kappa_{x,i}/\kappa_{x,0}$) of dry TPU formulations containing 20 vol% Ag and 0.056 $mmol_{iodine}/cm^3_{Ag}$ of iodine component x, measured at day i. Conductivity values are normalized to the initial conductivity at day 1 ($\kappa_{x,0}$). All samples were stored at 60 °C throughout the testing period.

Image analysis

The commercial software ImageJ [41] was used for image analysis. Hysteresis thresholding was applied for the SEM images shown in Figure 18 of the main text using identical parameters. The ImageJ Hysteresis plugin was used with a high threshold of 155 and a low threshold of 90. Subsequently, the particle analysis tool was applied with the pixel size range set from 0 to infinity and circularity from 0.00 to 1.00. The 'Include holes' option was also enabled. The results are shown in Figure *55*a). The detected interconnected regions are randomly colored to enhance visual differentiation. In Figure *55*b), the original SEM images from Figure 18 main text are overlaid with the corresponding processed results from a), illustrating a strong agreement between the processed and original data. Among the regimes, regime 2 exhibits the largest interconnected areas (aggregates).

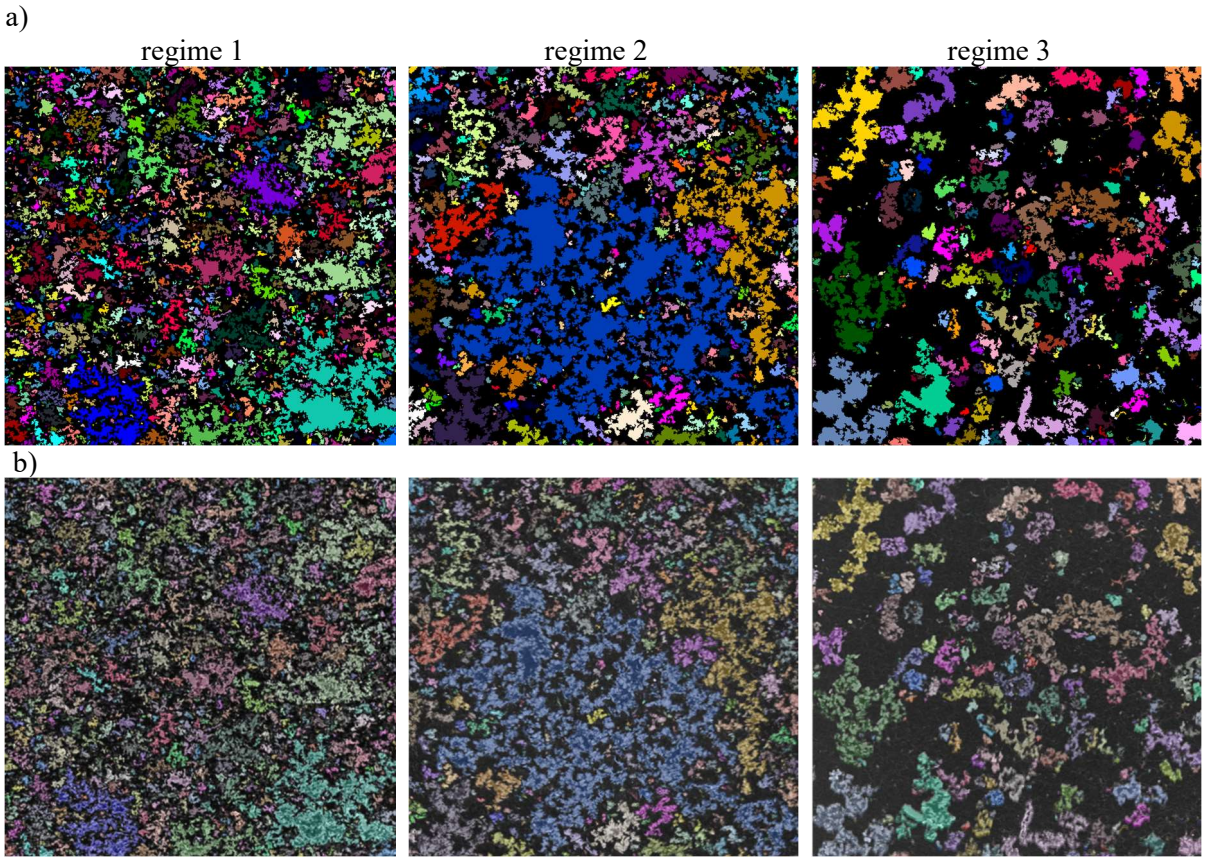

Figure 55 a) SEM images after hysteresis thresholding for regime 1, 2 and 3. The coloring of the areas random and presents interconnected areas. b) An overlay from SEM images and the images after thresholding.

This is further confirmed by the calculation of the area fraction of the different aggregate size classes shown in Figure *55*, which provides a clearer perspective on the microstructural changes induced by increasing iodine concentration. Figure 57 presents the area fraction distribution occupied by Ag agglomerates of different size ranges, given in terms of occupied pixel.

The data clearly shows that most of the space occupied by Ag particles (≈ 30 %) corresponds to regions smaller than 0.25 k pixel for regime 1. In regime 2, almost 35 % of the area is occupied by regions larger than 20 k pixel, whereas in regime 3, slightly more than 30 % of the area is occupied by agglomerates between 2 k and 5 k pixel.

These results demonstrate that with increasing iodine concentration, the microstructure undergoes a distinct transition - from relatively small, well-dispersed silver particles and small agglomerates, to a structure dominated by large aggregates of Ag particles able to form a network with many conductive pathways, and finally a structure comprising medium-sized agglomerates which create fewer conductive pathways.

This aligns well with the observed evolution of electrical conductivity (Figure 16) and is schematically depicted in Figure 18.

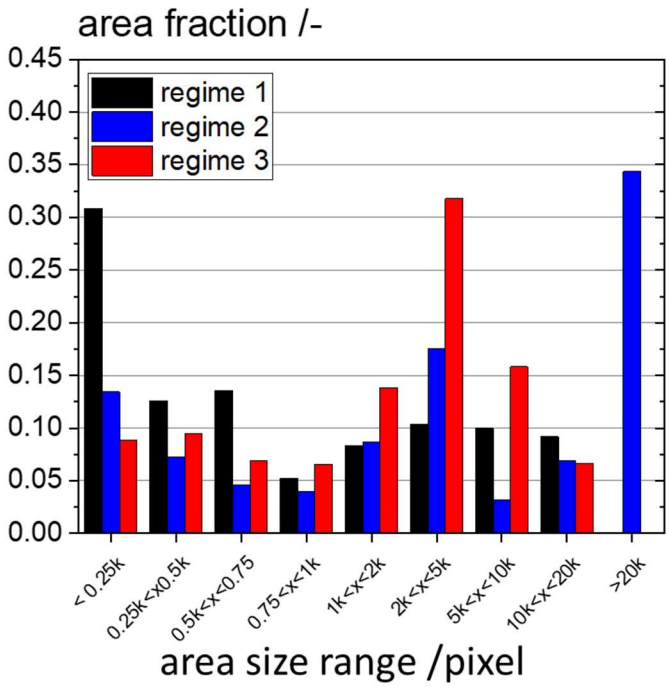

Figure 56 Area fraction distribution of the total occupied area by Ag-particle agglomerates of different size ranges, based on image analysis from Figure 55a).

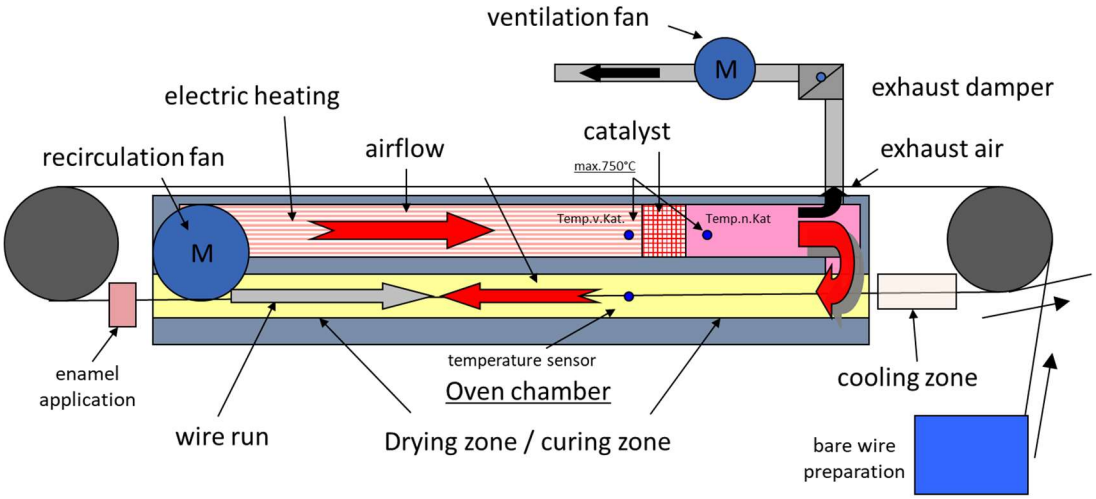

Figure 57 The setup of an industrial scale wire coating machine.

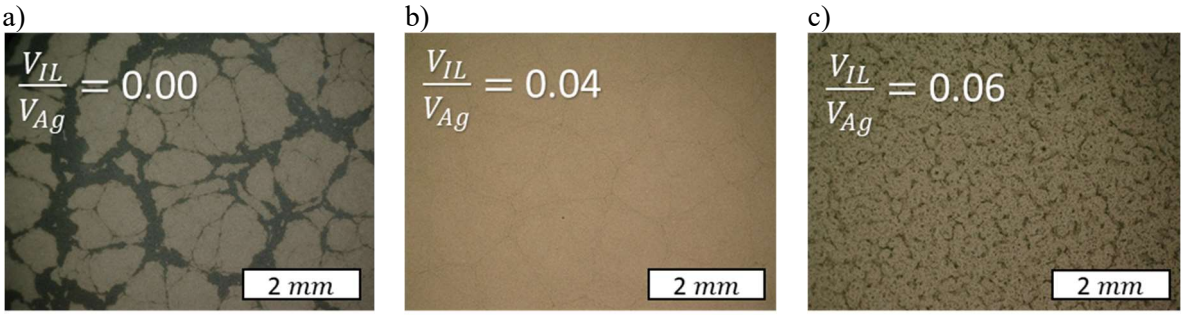

Figure 58 Light microscopic images of Ag-filled polymer solutions with an VIL/VAg ratio of a) 0.00, b) 0.04, c) 0.06.

Figure 58 reveals the structural changes within the Ag-filled polymer solution as the IL concentration rises. In a), the particles appear to have imperfect compatibility with the polymer solution, as evidenced by a relatively uneven distribution of silver particles. Dark areas exhibit higher concentrations compared to lighter regions. As IL concentration increases in b), the solution seems more homogeneous. However, further increasing the IL concentration in c) leads to the formation of large agglomerates.

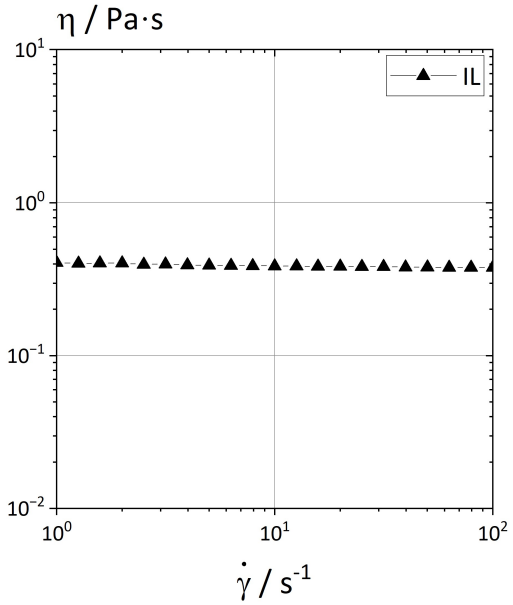

Figure 59 Viscosity η as a function of shear rate $\dot{\gamma}$ for the ionic liquid (IL) 1-Butyl-3-Methyl-imidazolium iodide.

Figure 60 The electrical resistance measurement of the coated yarn.

a)

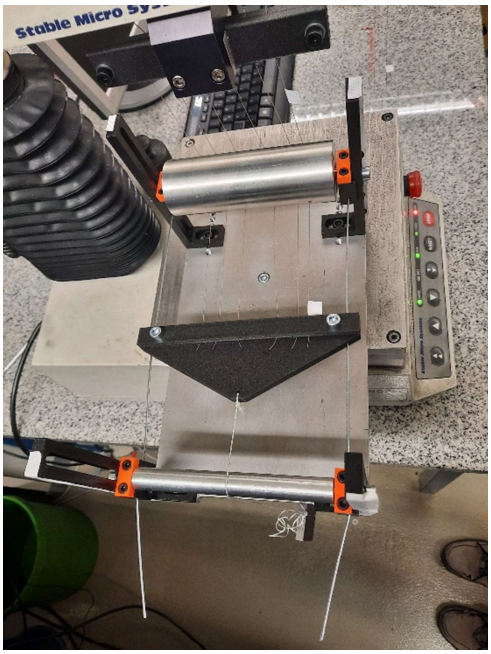

b)

Figure 61 The bending test of the yarn.

a) b)

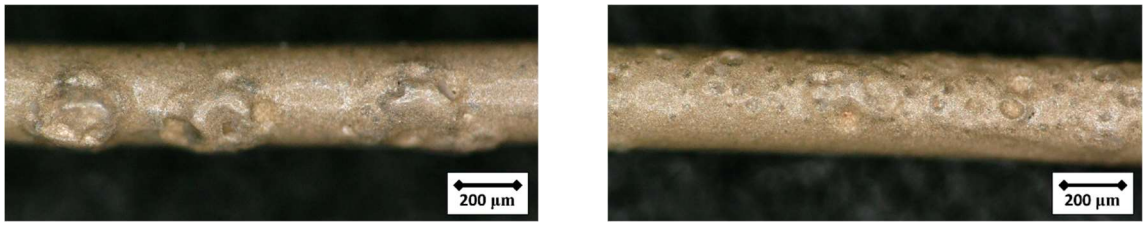

Figure 62 Examples for occasionally occurring defects during the wire coating process. Typically, a combination of air inclusions and craters caused by inhomogeneously evaporating solvent.

a)

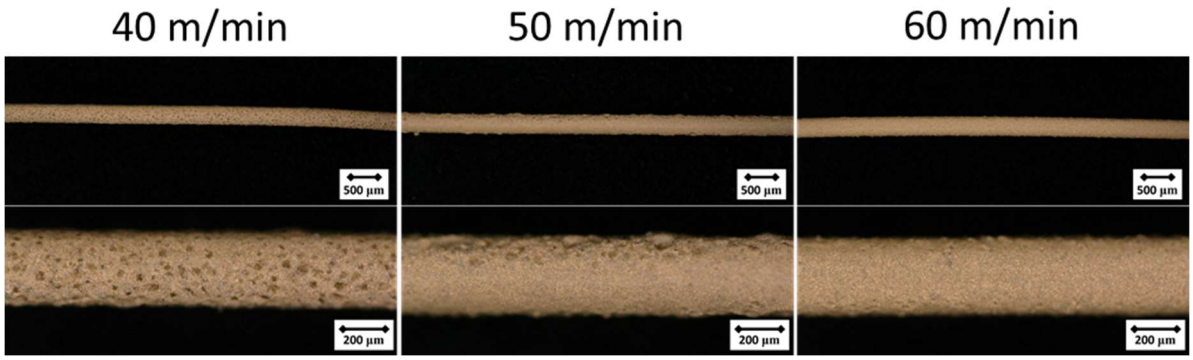

b)

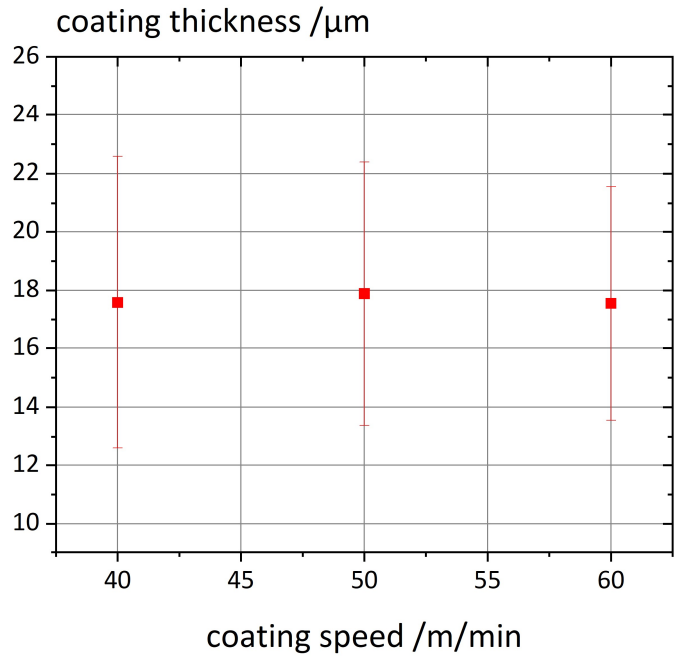

c)

coating cycle:	nozzle diameter:
1.	390 µm
2.	400 µm
3.	400 µm
4.	410 µm
5.	410 µm
6.	420 µm
7.	420 µm
8.	430 µm
9.	440 µm
10.	445 µm

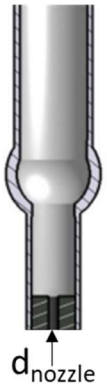

Figure 63 The results of the industrial-scale coating trial conducted at a temperature of 450 °C with different coating speeds (40 ,50 and 60 m/min). The coating contains 12 vol% Ag regarding all ne non-volatile components and an IL-Ag-volume ratio of 0.04. a) Microscopic images of the coated wire surface after ten coating cycles for the different coating speeds (40, 50 and 60 m/min). b) the total coating thickness on the wire after ten coating cycles for wires coated at speeds of 40, 50 and 60 m/min. c) The number and diameter of the coating nozzles that were used.

In Figure 63a) the coated wire surfaces for the different coating speeds after 10 coating cycles are displayed. The wire coated with the highest coating speed (60 m/min) appears to have the highest surface quality. However, the sequence of coating nozzle diameters (shown in c)) is still not optimized which explains the high standard deviation of the coating thickness in b).

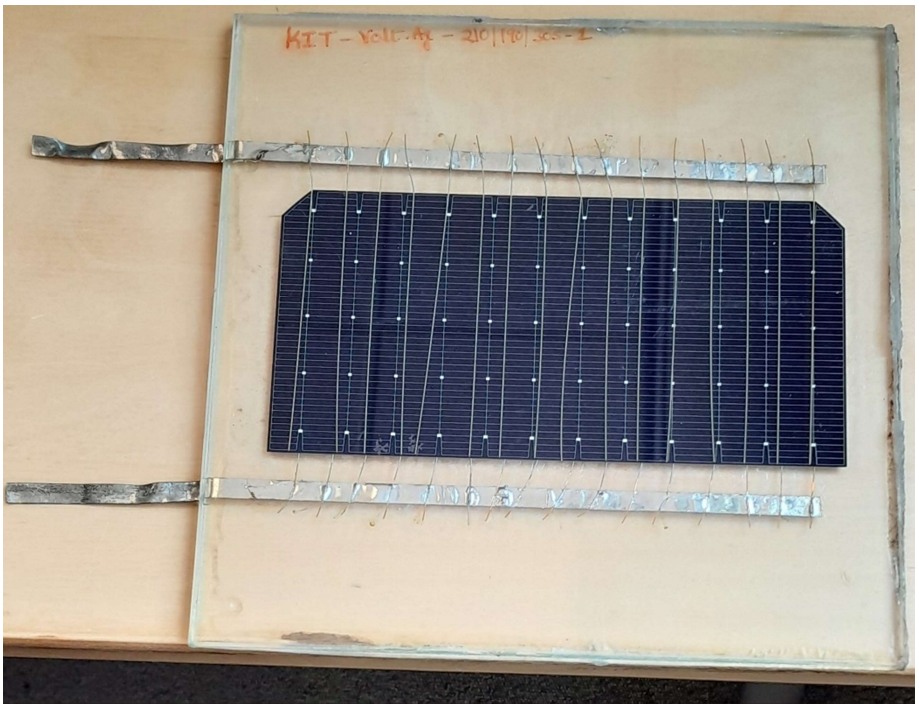

Figure 64 Single-cell (half cut M6 SHJ solar cell) glass/glass module connected using Ag-filled thermoplastic-coated TECC wires without butyl edge sealant.

Table 5 The yarn coating parameters

Number of Coatings	Temperature	Coating Speed	Guiding Nozzle	Coating Nozzle
1.	280 °C	2.8 m/min	315 µm	320 µm
2.	280 °C	2.8 m/min	315 µm	320 µm
3.	280 °C	2.8 m/min	325 µm	320 µm
4.	280 °C	2.8 m/min	330 µm	325 µm
5.	280 °C	2.8 m/min	330 µm	325 µm

Table 6 The composition of wire enamels and resulting adhesives for the adjustments of the electrical conductivity (section 3.1) by varying the Il concentration.

	wire enamel				adhesive		
V_{IL}/V_{Ag} / -	$\varphi_{Voltatex\ 8609}$ / -	φ_{Ag} / -	φ_{IL} / -	φ_{DMSO} / -	$\varphi_{Voltatex\ 8609,dry}$ / -	φ_{Ag} / -	φ_{IL} / -
0	0.9865	0.0135	0.0000	0.0000	0.88	0.12	0
0.02	0.9851	0.0135	0.0003	0.0014	0.8776	0.12	0.0024
0.03	0.9845	0.0135	0.0004	0.0020	0.8764	0.12	0.0036
0.04	0.9838	0.0135	0.0005	0.0027	0.8752	0.12	0.0048
0.06	0.9824	0.0135	0.0008	0.0041	0.8728	0.12	0.0072
0.08	0.9810	0.0135	0.0011	0.0055	0.8704	0.12	0.0096
0.12	0.9782	0.0136	0.0016	0.0082	0.8656	0.12	0.0144

Table 7 The composition of the wire enamels and resulting adhesives for the adjustment of the polymer concentration in the wire enamel and its viscosity (section 3.2). The Il-Ag-volume ratio was maintained at a constant value of 0.04.

	wire enamel				adhesive		
polymer concetration in Voltatex 8609 / vol%	$\varphi_{Voltatex\ 8609}$ / -	φ_{Ag} / -	φ_{IL} / -	φ_{DMSO} / -	$\varphi_{Voltatex\ 8609,dry}$ / -	φ_{Ag} / -	φ_{IL} / -
10	0.9838	0.0135	0.0005	0.0027	0.8752	0.1200	0.0048
13	0.9790	0.0175	0.0007	0.0035	0.8752	0.1200	0.0048
14	0.9773	0.0189	0.0008	0.0038	0.8752	0.1200	0.0048
16	0.9743	0.0214	0.0009	0.0043	0.8752	0.1200	0.0048
18	0.9711	0.0240	0.0010	0.0048	0.8752	0.1200	0.0048

Table 8 The composition of the wire enamel and resulting adhesive for the industrial coating trial and cell contacting (section 3.2). The Il-Ag-volume ratio was maintained at a constant value of 0.04.

	wire enamel				adhesive		
polymer concetration in Voltatex 8609 / vol%	$\varphi_{Voltatex\ 8609}$ / -	φ_{Ag} / -	φ_{IL} / -	φ_{DMSO} / -	$\varphi_{Voltatex8609.dry}$ / -	φ_{Ag} / -	φ_{IL} / -
10	0.9838	0.0135	0.0005	0.0027	0.8752	0.1200	0.0048

Chapter 10 References

[1] R. Aradhana, S. Mohanty, S. K. Nayak, *International Journal of Adhesion and Adhesives*. **2020**, *99*, 102596. DOI: https://doi.org/10.1016/j.ijadhadh.2020.102596.

[2] H. Sun, Z. Han, N. Willenbacher, *ACS Appl Mater Interfaces*. **2019**, *11* (*41*), 38092–38102. DOI: https://doi.org/10.1021/acsami.9b11071.

[3] H. Sun, J. Zettl, N. Willenbacher, *Additive Manufacturing*. **2023**, *78*, 103872. DOI: https://doi.org/10.1016/j.addma.2023.103872.

[4] Y. Guan, X. Chen, F. Li, H. Gao, *International Journal of Adhesion and Adhesives*. **2010**, *30* (*2*), 80–88. DOI: https://doi.org/10.1016/j.ijadhadh.2009.09.003.

[5] A. Lund, Y. Wu, B. Fenech-Salerno, F. Torrisi, T. B. Carmichael, C. Müller, *MRS Bull*. **2021**, *46* (*6*), 491–501. DOI: https://doi.org/10.1557/s43577-021-00117-0.

[6] J. Marten, M. Schnaiter, Y. Zemen, L. Podlowski, S. Ricken, N. Willenbacher, *Solar Energy Materials and Solar Cells*. **2024**, *273*, 112966. DOI: https://doi.org/10.1016/j.solmat.2024.112966.

[7] T. Geipel, L. C. Rendler, M. Stompe, U. Eitner, L. Rissing, *Energy Procedia*. **2015**, *77*, 346–355. DOI: https://doi.org/10.1016/j.egypro.2015.07.049.

[8] Michael Rubinstein, *Polymer Physics*, Oxford University Press **2003,** S2-10.

[9] W. Kaiser, *Kunststoffchemie Für Ingenieure*, Hanser, München **2006,** S31-34.

[10] R. Surace, C. Pagano, V. Bellantone, S. Gatti, L. Castellani, M. Vighi, G. Stoclet, S. Sechi, I. Fassi, F. Baldi, *Polymer*. **2021**, *230*, 124035. DOI: https://doi.org/10.1016/j.polymer.2021.124035.

[11] U. A. Dar, Y. J. Xu, S. M. Zakir, M.-U. Saeed, *Journal of Applied Polymer Science*. **2017**, *134* (*7*). DOI: https://doi.org/10.1002/app.44474.

[12] F. Grønborg, D. B. Pedersen, J. Spangenberg, A. E. Daugaard, M. L. Susoff, *Journal of Applied Polymer Science*. **2024**, *141* (*25*), e55521. DOI: https://doi.org/10.1002/app.55521.

[13] P. Latko-Durałek, J. Macutkevic, C. Kay, A. Boczkowska, T. McNally, *Journal of Applied Polymer Science*. **2018**, *135* (*11*), 45999. DOI: https://doi.org/10.1002/app.45999.

[14] S. Sathyanarayana, C. Hübner, in *Structural Nanocomposites: Perspectives for Future Applications* (Ed: J. Njuguna), Springer, Berlin, Heidelberg **2013**.

[15] C. Wongsamut, R. Suwanpreedee, H. Manuspiya, *International Journal of Adhesion and Adhesives*. **2020**, *102*, 102677. DOI: https://doi.org/10.1016/j.ijadhadh.2020.102677.

[16] Richard J. Spontak, Nikunj P Patel, *Interface Science*. **2000**, *5* (*5–6*), 333–340.

[17] G. V. Malysheva, N. V. Bodrykh, *Polym. Sci. Ser. D*. **2011**, *4* (*4*), 301–303. DOI: https://doi.org/10.1134/S1995421211040095.

[18] G. Habenicht, in *Kleben*, Springer, Berlin, Heidelberg **2009,** S224-232.

[19] M. J. Yim, Y. Li, K. Moon, K. W. Paik, C. P. Wong, *Journal of Adhesion Science and Technology*. **2008**, *22* (*14*), 1593–1630. DOI: https://doi.org/10.1163/156856108X320519.

[20] P. Ossowicz-Rupniewska, P. Bednarczyk, M. Nowak, A. Nowak, W. Duchnik, Ł. Kucharski, J. Rokicka, A. Klimowicz, Z. Czech, *IJMS*. **2021**, *22* (*21*), 11840. DOI: https://doi.org/10.3390/ijms222111840.

[21] I- Hinz, S.-H. Schulze, F. Brache, M. Schak, F. Wenger, *27th EU-PVSEC*. **2012**.

[22] H. Cherdron, F. Herold, A. Schneller, *Chemie in unserer Zeit*. **1989**, *23* (*6*), 181–192. DOI: https://doi.org/10.1002/ciuz.19890230602.

[23] S. H. S. Boddu, P. Bhagav, P. K. Karla, S. Jacob, M. D. Adatiya, T. M. Dhameliya, K. M. Ranch, A. K. Tiwari, *JFB*. **2021**, *12* (*4*), 58. DOI: https://doi.org/10.3390/jfb12040058.

[24] F. C. Toy, J. B. Speakman, A. K. Saville, *Journal of the Textile Institute Proceedings*. **1946**, *37* (*7*), P271–P294. DOI: https://doi.org/10.1080/19447014608662058.

[25] D. K. Chattopadhyay, K. V. S. N. Raju, *Progress in Polymer Science*. **2007**, *32* (*3*), 352–418. DOI: https://doi.org/10.1016/j.progpolymsci.2006.05.003.

[26] K. Kojio, M. Furukawa, Y. Nonaka, S. Nakamura, *Materials*. **2010**, *3* (*12*), 5097–5110. DOI: https://doi.org/10.3390/ma3125097.

[27] J. Tan, Y. Mei Ding, X. Tao He, Y. Liu, Y. An, W. Min Yang, *Journal of Applied Polymer Science*. **2008**, *110* (*3*), 1851–1857. DOI: https://doi.org/10.1002/app.28756.

[28] H.-Y. Mi, M. R. Salick, X. Jing, B. R. Jacques, W. C. Crone, X.-F. Peng, L.-S. Turng, *Materials Science and Engineering: C*. **2013**, *33* (*8*), 4767–4776. DOI: https://doi.org/10.1016/j.msec.2013.07.037.

[29] H.-Y. Mi, X. Jing, B. N. Napiwocki, B. S. Hagerty, G. Chen, L.-S. Turng, *Journal of Materials Chemistry B*. **2017**, *5* (*22*), 4137–4151. DOI: https://doi.org/10.1039/c7tb00419b.

[30] S. M. Desai, R. Y. Sonawane, A. P. More, *Polymers for Advanced Technologies*. **2023**, *34* (*7*), 2061–2082. DOI: https://doi.org/10.1002/pat.6041.

[31] H. Zhang, F. Zhang, Y. Wu, *Ind. Eng. Chem. Res.* **2020**, *59* (*10*), 4483–4492. DOI: https://doi.org/10.1021/acs.iecr.9b06107.

[32] T. Geipel, *Electrically Conductive Adhesives for Photovoltaic Modules*, Fraunhofer Verlag, Stuttgart **2018**.

[33] T. Geipel, V. Nikitina, L.P. Bauermann, E. Fokuhl, E. Schnabel, D. Erath, ... & D. Breitenbücher, *36th EU PV Solar Energy Conference and Exhibition*. **2019**.

[34] C. Kaiser, V. Nikitina, T. Geipel, & A. Kraft, *37th European PV Solar Energy Conference and Exhibition*. **2020**.

[35] C. Li, Q. Li, X. Long, T. Li, J. Zhao, K. Zhang, S. E, J. Zhang, Z. Li, Y. Yao, *ACS Appl Mater Interfaces*. **2017**, *9* (*34*), 29047–29054. DOI: https://doi.org/10.1021/acsami.7b07045.

[36] T. Araki, M. Nogi, K. Suganuma, M. Kogure, O. Kirihara, *IEEE Electron Device Letters*. **2011**, *32* (*10*), 1424–1426. DOI: https://doi.org/10.1109/LED.2011.2161663.

[37] Y. Li, K.-S. Moon, H. Li, C. P. Wong, in *2004 Proceedings. 54th Electronic Components and Technology Conference (IEEE Cat. No.04CH37546)*, IEEE **2004**.

[38] J. Nicolics, M. Mündlein, in *Micro- and Opto-Electronic Materials and Structures: Physics, Mechanics, Design, Reliability, Packaging* (Eds: E. Suhir, Y. C. Lee, C. P. Wong), Springer US, Boston, MA **2007**.

[39] E. Sancaktar, L. Bai, *Polymers*. **2011**, *3* (*1*), 427–466. DOI: https://doi.org/10.3390/polym3010427.

[40] J. E. Morris, J. Liu, *Comprehensive Review*. **1999**, 37–77.

[41] Y. Li, C. P. Wong, *Materials Science and Engineering: R: Reports*. **2006**, *51* (*1–3*), 1–35. DOI: https://doi.org/10.1016/j.mser.2006.01.001.

[42] A. Pajor-Świerzy, R. Socha, R. Pawłowski, P. Warszyński, K. Szczepanowicz, *Nanotechnology*. **2019**, *30* (*22*), 225301. DOI: https://doi.org/10.1088/1361-6528/ab0467.

[43] S. Qi, R. Litchfield, D. A. Hutt, B. Vaidhyanathan, C. Liu, P. Webb, S. Ebbens, in *2012 IEEE 62nd Electronic Components and Technology Conference* **2012**.

[44] S. R. Pettersen, H. Kristiansen, S. Nagao, S. Helland, J. Njagi, K. Suganuma, Z. Zhang, J. He, *Journal of Elec Materi*. **2016**, *45* (*7*), 3734–3743. DOI: https://doi.org/10.1007/s11664-016-4498-1.

[45] S. Chen, K. Liu, Y. Luo, D. Jia, H. Gao, G. Hu, L. Liu, *International Journal of Adhesion and Adhesives*. **2013**, *45*, 138–143. DOI: https://doi.org/10.1016/j.ijadhadh.2013.04.004.

[46] M. Kanzaki, Y. Kawaguchi, H. Kawasaki, *ACS Appl Mater Interfaces*. **2017**, *9* (*24*), 20852–20858. DOI: https://doi.org/10.1021/acsami.7b04641.

[47] Z. Czech, A. Kowalczyk, R. Pełech, R. J. Wróbel, L. Shao, Y. Bai, J. Świderska, *International Journal of Adhesion and Adhesives*. **2012**, *36*, 20–24. DOI: https://doi.org/10.1016/j.ijadhadh.2012.04.004.

[48] E. Vessally, R. M. Rzayev, A. A. Niyazova, T. Aggarwal, K. E. Rahimova, *RSC Adv.* **2024**, *14* (*54*), 40141–40159. DOI: https://doi.org/10.1039/D4RA08446B.

[49] H. E. Suess, H. C. Urey, *Rev. Mod. Phys.* **1956**, *28* (*1*), 53–74. DOI: https://doi.org/10.1103/RevModPhys.28.53.

[50] K. Ashton, *RFID journal*. **2009**, *22* (*7*), 97–114.

[51] D. Mishra, A. Gunasekaran, S. J. Childe, T. Papadopoulos, R. Dubey, S. Wamba, *Industrial Management & Data Systems*. **2016**, *116* (*7*), 1331–1355. DOI: https://doi.org/10.1108/IMDS-11-2015-0478.

[52] W. H. Dutton, **2013**. DOI: https://doi.org/10.2139/ssrn.2324902.

[53] N. M. Cusack, P. D. Venkatraman, U. Raza, A. Faisal, *ECS Sens. Plus*. **2024**, *3* (*1*), 017001. DOI: https://doi.org/10.1149/2754-2726/ad3561.

[54] J. W. Cheng, H. Mitomo, *Telematics and Informatics*. **2017**, *34* (*2*), 528–539. DOI: https://doi.org/10.1016/j.tele.2016.09.010.

[55] M. Stoppa, A. Chiolerio, *Sensors*. **2014**, *14* (*7*), 11957–11992. DOI: https://doi.org/10.3390/s140711957.

[56] N. Niknejad, W. B. Ismail, A. Mardani, H. Liao, I. Ghani, *Engineering Applications of Artificial Intelligence*. **2020**, *90*, 103529. DOI: https://doi.org/10.1016/j.engappai.2020.103529.

[57] J. Qin, L.-J. Yin, Y.-N. Hao, S.-L. Zhong, D.-L. Zhang, K. Bi, Y.-X. Zhang, Y. Zhao, Z.-M. Dang, *Advanced Materials*. **2021**, *33* (*34*), 2008267. DOI: https://doi.org/10.1002/adma.202008267.

[58] Z. Ma, Y. Zhang, K. Zhang, H. Deng, Q. Fu, *Nano Materials Science*. **2023**, *5* (*3*), 265–277. DOI: https://doi.org/10.1016/j.nanoms.2021.11.002.

[59] M. Ma, Z. Zhang, Q. Liao, F. Yi, L. Han, G. Zhang, S. Liu, X. Liao, Y. Zhang, *Nano Energy*. **2017**, *32*, 389–396. DOI: https://doi.org/10.1016/j.nanoen.2017.01.004.

[60] R. Qin, M. Hu, X. Li, T. Liang, H. Tan, J. Liu, G. Shan, *Microsyst Nanoeng*. **2021**, *7* (*1*), 100. DOI: https://doi.org/10.1038/s41378-021-00327-1.

[61] M. Su, P. Li, X. Liu, D. Wei, J. Yang, *Nanomaterials*. **2022**, *12* (*9*), 1495. DOI: https://doi.org/10.3390/nano12091495.

[62] N. Yusof, A. F. Ismail, *Journal of Analytical and Applied Pyrolysis*. **2012**, *93*, 1–13. DOI: https://doi.org/10.1016/j.jaap.2011.10.001.

[63] J. W. Cho, J. S. Choi, *Journal of Applied Polymer Science*. **2000**, *77* (*9*), 2082–2087. DOI: https://doi.org/10.1002/1097-4628(20000829)77:9<2082::AID-APP26>3.0.CO;2-W.

[64] J. W. Cho, J. S. Choi, Y. S. Yoon, *Journal of Applied Polymer Science*. **2002**, *83* (*11*), 2447–2453. DOI: https://doi.org/10.1002/app.10226.

[65] T. B. Freiberg, T. B. Freiberg, S. Glas, *Composites Science and Technology*. **2001**.

[66] Mei Zhang, Ken R. Atkinson, Ray H. Baughman, *SCIENCE*. **2004**, *306* (*5700*), 1358–1361.

[67] K. Jiang, Q. Li, S. Fan, *Nature*. **2002**, *419* (*6909*), 801–801. DOI: https://doi.org/10.1038/419801a.

[68] A. E. Aliev, C. Guthy, M. Zhang, S. Fang, A. A. Zakhidov, J. E. Fischer, R. H. Baughman, *Carbon*. **2007**, *45* (*15*), 2880–2888. DOI: https://doi.org/10.1016/j.carbon.2007.10.010.

[69] Y. Atwa, N. Maheshwari, I. A. Goldthorpe, *J. Mater. Chem. C*. **2015**, *3* (*16*), 3908–3912. DOI: https://doi.org/10.1039/C5TC00380F.

[70] P. Mostafalu, M. Akbari, K. A. Alberti, Q. Xu, A. Khademhosseini, S. R. Sonkusale, *Microsyst Nanoeng*. **2016**, *2*, 16039. DOI: https://doi.org/10.1038/micronano.2016.39.

[71] Y. Tang, B. Guo, M. A. Cruz, H. Chen, Q. Zhou, Z. Lin, F. Xu, F. Xu, X. Chen, D. Cai, et al., *Adv Sci (Weinh)*. **2022**, *9* (*24*), 2201111. DOI: https://doi.org/10.1002/advs.202201111.

[72] L. Gan, Z. Zeng, H. Lu, Daiqi Li, K. Wei, G. Cai, Y. Zhang, *SmartMat*. **2023**, *4* (*2*), 1151.

[73] S. Aziz, J. G. Martinez, B. Salahuddin, N. Persson, E. W. H. Jager, *Adv Funct Materials*. **2021**, *31* (*10*). DOI: https://doi.org/10.1002/adfm.202008959.

[74] D. Cottet, J. Grzyb, T. Kirstein, G. Troster, *IEEE Trans. Adv. Packag.* **2003**, *26* (*2*), 182–190. DOI: https://doi.org/10.1109/TADVP.2003.817329.

[75] S. Chen, S. Liu, P. Wang, H. Liu, L. Liu, *J Mater Sci*. **2018**, *53* (*4*), 2995–3005. DOI: https://doi.org/10.1007/s10853-017-1644-y.

[76] T.-G. La, S. Qiu, D. K. Scott, R. Bakhtiari, J. W. P. Kuziek, K. E. Mathewson, J. Rieger, H.-J. Chung, *Adv Healthc Mater*. **2018**, *7* (*22*), 1801033. DOI: https://doi.org/10.1002/adhm.201801033.

[77] G. Paul, R. Torah, S. Beeby, J. Tudor, *Sensors and Actuators A: Physical*. **2014**, *206*, 35–41. DOI: https://doi.org/10.1016/j.sna.2013.11.026.

[78] X. Ji, W. Liu, Y. Yin, C. Wang, F. Torrisi, *J. Mater. Chem. C*. **2020**, *8* (*44*), 15788–15794. DOI: https://doi.org/10.1039/D0TC03144E.

[79] M. Kim, Y. Zhang, P. Verlinden, B. Hallam, *11th International Conference on Crystalline Silicon Photovoltaics, AIP Publishing*. **2021**, 090001-1–8. DOI: https://doi.org/10.1063/5.0090424.

[80] Fischer Markus, Michael Woodhouse, Puzant Baliozian, *VDMA*. **2023**, (*15th Edition*).

[81] M. V. Dambhare, B. Butey, S. V. Moharil, *J. Phys.: Conf. Ser.* **2021**, *1913* (*1*), 012053. DOI: https://doi.org/10.1088/1742-6596/1913/1/012053.

[82] V. Wesselak, S. Voswinckel, *Photovoltaik – Wie Sonne Zu Strom Wird*, Springer Berlin Heidelberg, Berlin, Heidelberg **2016**.

[83] A. Shah, Ed., *Solar Cells and Modules*, Vol. 301, Springer International Publishing, Cham **2020**.

[84] A. Metz, D. Adler, S. Bagus, H. Blanke, M. Bothar, E. Brouwer, S. Dauwe, K. Dressler, R. Droessler, T. Droste, et al., *Solar Energy Materials and Solar Cells*. **2014**, *120*, 417–425. DOI: https://doi.org/10.1016/j.solmat.2013.06.025.

[85] A. Blakers, *IEEE Journal of Photovoltaics*. **2019**, *9* (*3*), 629–635. DOI: https://doi.org/10.1109/JPHOTOV.2019.2899460.

[86] B. Kafle, B. S. Goraya, S. Mack, F. Feldmann, S. Nold, J. Rentsch, *Solar Energy Materials and Solar Cells*. **2021**, *227*, 111100. DOI: https://doi.org/10.1016/j.solmat.2021.111100.

[87] G. M. Wilson, M. Al-Jassim, W. K. Metzger, S. W. Glunz, P. Verlinden, G. Xiong, L. M. Mansfield, B. J. Stanbery, K. Zhu, Y. Yan, et al., *J. Phys. D: Appl. Phys.* **2020**, *53* (*49*), 493001. DOI: https://doi.org/10.1088/1361-6463/ab9c6a.

[88] Xinbo Yang, K. Weber, in *2015 IEEE 42nd Photovoltaic Specialist Conference (PVSC)*, IEEE, New Orleans, LA **2015**.

[89] R. Younas, H. Imran, S. I. H. Shah, T. M. Abdolkader, N. Z. Butt, *IEEE Trans. Electron Devices*. **2019**, *66* (*4*), 1819–1826. DOI: https://doi.org/10.1109/TED.2019.2900691.

[90] S. De Wolf, A. Descoeudres, Z. C. Holman, C. Ballif, *Green*. **2012**, *2* (*1*), 7–24. DOI: https://doi.org/10.1515/green-2011-0018.

[91] J. Haschke, O. Dupré, M. Boccard, C. Ballif, *Solar Energy Materials and Solar Cells*. **2018**, *187*, 140–153. DOI: https://doi.org/10.1016/j.solmat.2018.07.018.

[92] T. G. Allen, J. Bullock, X. Yang, A. Javey, S. De Wolf, *Nat Energy*. **2019**, *4* (*11*), 914–928. DOI: https://doi.org/10.1038/s41560-019-0463-6.

[93] N. Wöhrle, E. Lohmüller, M. Mittag, A. Moldovan, P. Baliozian, T. Fellmeth, A. Kraft, R. Preu, **n.d.**

[94] T. Dullweber, J. Schmidt, *IEEE Journal of Photovoltaics*. **2016**, *6* (*5*), 1366–1381. DOI: https://doi.org/10.1109/JPHOTOV.2016.2571627.

[95] D. K. Ghosh, S. Bose, G. Das, S. Acharyya, A. Nandi, S. Mukhopadhyay, A. Sengupta, *Surfaces and Interfaces*. **2022**, *30*, 101917. DOI: https://doi.org/10.1016/j.surfin.2022.101917.

[96] S. Braun, G. Hahn, R. Nissler, C. Pönisch, D. Habermann, *Energy Procedia*. **2013**, *38*, 334–339. DOI: https://doi.org/10.1016/j.egypro.2013.07.286.

[97] J. Walter, M. Tranitz, M. Volk, C. Ebert, U. Eitner, *Energy Procedia*. **2014**, *55*, 380–388. DOI: https://doi.org/10.1016/j.egypro.2014.08.109.

[98] G. Beaucarne, I. Kuzma-Filipek, F. Campeol, X. Young, J. Wei, Y. Yu, R. Russell, F. Duerinckx, *Energy Procedia*. **2015**, *67*, 185–193. DOI: https://doi.org/10.1016/j.egypro.2015.03.302.

[99] A. Lorenz, J. Schube, V. Nikitina, S. Mack, S. Schweigert, J. Buddgard, J. Albrecht, M. Pospischil, A. Kraft, A. Wolf, et al., *EPJ Photovolt.* **2025**, *16*, 6. DOI: https://doi.org/10.1051/epjpv/2024043.

[100] T. Geipel, M. Meinert, A. Kraft, U. Eitner, *IEEE J. Photovoltaics*. **2018**, *8* (*4*), 1074–1081. DOI: https://doi.org/10.1109/JPHOTOV.2018.2828829.

[101] A. Rose, D. Erath, V. Nikitina, J. Schube, D. Güldali, Ä. Minat, T. Rößler, A. Richter, S. Kirner, A. Kraft, et al., *Solar Energy Materials and Solar Cells*. **2023**, *261*, 112515. DOI: https://doi.org/10.1016/j.solmat.2023.112515.

[102] A. Faes, M. Despeisse, J. Levrat, J. Champliaud, A. Lachowicz, J. Geissbühler, ... & C. Ballif, *6th Workshop on Metallization and Interconnection for Crystalline Silicon Solar Cells*. **2016**.

[103] Y. Zemen, L. Podlowski, S. Wendlandt, J. Stegmann, *IEEE 48th Photovoltaic Specialists Conference (PVSC)*. **n.d.**, 480–485. DOI: https://doi.org/10.1109/PVSC43889.2021.9518596.

[104] J. Hagedorn, F. Sell-Le Blanc, J. Fleischer, **2016**, 129–131. DOI: https://doi.org/10.1007/978-3-662-49210-9.

[105] Daoqiang Lu, Q. K. Tong, C. P. Wong, *IEEE Trans. Comp. Packag. Technol.* **1999**, *22* (*3*), 365–371. DOI: https://doi.org/10.1109/6144.796536.

[106] Y. Li, K.-S. Moon, A. Whitman, C. P. Wong, *IEEE Trans. Comp. Packag. Technol.* **2006**, *29* (*4*), 758–763. DOI: https://doi.org/10.1109/TCAPT.2006.885940.

[107] H. Sun, X. Zhang, M. M. F. Yuen, *Composites Science and Technology*. **2016**, *137*, 109–117. DOI: https://doi.org/10.1016/j.compscitech.2016.10.028.

[108] C. Li, X. Gong, L. Tang, K. Zhang, J. Luo, L. Ling, J. Pu, T. Li, M. Li, Y. Yao, *J. Mater. Chem. C*. **2015**, *3* (*24*), 6178–6184. DOI: https://doi.org/10.1039/C5TC00593K.

[109] H. Wu, S. Chiang, W. Han, Y. Tang, F. Kang, C. Yang, *Composites Science and Technology*. **2014**, *99*, 109–116. DOI: https://doi.org/10.1016/j.compscitech.2014.04.021.

[110] M. Grouchko, A. Kamyshny, C. F. Mihailescu, D. F. Anghel, S. Magdassi, *ACS Nano*. **2011**, *5* (*4*), 3354–9. DOI: https://doi.org/10.1021/nn2005848.

[111] T. Lim, H. J. Kim, H. Zhang, S. Lee, *Smart Mater. Struct.* **2021**, *30* (*7*), 075006. DOI: https://doi.org/10.1088/1361-665X/abfb7f.

[112] Y. Zemen, L. Podlowski, S. Wendlandt, J. Stegmann, *11th International Conference on Crystalline Silicon Photovoltaics*. **2022**, 090002-1–8. DOI: https://doi.org/10.1063/5.0089261.

[113] Y. Zemen, S. Wendlandt, B. Litzenberger, L. Podlowski, *8th World Conference on Photovoltaic Energy Conversion*. **2022**, (*11*), 803–806.

[114] J. Marten, J. S. Urallar, T. M. Duong, P. Théato, N. Willenbacher, *ACS Appl. Mater. Interfaces*. **2025**. DOI: https://doi.org/10.1021/acsami.5c09040.

[115] M. Kronsbein, L. Böck, K. Dyhr, T. Rößler, N. Willenbacher, *Solar Energy Materials and Solar Cells*. **2025**, *287*, 113603. DOI: https://doi.org/10.1016/j.solmat.2025.113603.

[116] P. Tan, H. Wang, F. Xiao, X. Lu, W. Shang, X. Deng, H. Song, Z. Xu, J. Cao, T. Gan, et al., *Nat Commun*. **2022**, *13* (*1*), 358. DOI: https://doi.org/10.1038/s41467-022-28027-y.

[117] Y. Zang, F. Zhang, C. Di, D. Zhu, *Mater. Horiz.* **2015**, *2* (*2*), 140–156. DOI: https://doi.org/10.1039/C4MH00147H.

[118] A. Larmagnac, S. Eggenberger, H. Janossy, J. Vörös, *Sci Rep*. **2014**, *4* (*1*), 7254. DOI: https://doi.org/10.1038/srep07254.

[119] J. Kolbe, A. Arp, F. Calderone, E. M. Meyer, W. Meyer, H. Schaefer, M. Stuve, *Microelectronics Reliability*. **2007**, *47* (*2–3*), 331–334. DOI: https://doi.org/10.1016/j.microrel.2006.02.017.

[120] P. Lall, J. Narangaparambil, K. Schulze, S. Miller, in *2021 20th IEEE Intersociety Conference on Thermal and Thermomechanical Phenomena in Electronic Systems (iTherm)* **2021**.

[121] P. Lall, J. Narangaparambil, V. Soni, S. Miller, in *2023 IEEE 73rd Electronic Components and Technology Conference (ECTC)* **2023**.

[122] S. Cheng, C. M. Huang, M. Pecht, *Microelectronics Reliability*. **2017**, *75*, 77–95. DOI: https://doi.org/10.1016/j.microrel.2017.06.016.

[123] M. A. Butt, N. L. Kazanskiy, S. N. Khonina, *Electronics*. **2022**, *11* (*5*), 716. DOI: https://doi.org/10.3390/electronics11050716.

[124] J. Marten, N. Gaukel, Y. Hu, Y. Wang, G. Yuan, N. Willenbacher, *Advanced Electronic Materials*. **2025**, 2400700. DOI: https://doi.org/10.1002/aelm.202400700.

[125] Erin Koos, Norbert Willenbacher, *SCIENCE*. **2011**, (*331*), 897–899. DOI: https://doi.org/10.1126/science.1199243.

[126] A. J. Lovinger, *The Journal of Adhesion*. **1979**, *10* (*1*), 1–15. DOI: https://doi.org/10.1080/00218467908544607.

[127] C. Li, Q. Li, L. Cheng, T. Li, H. Lu, L. Tang, K. Zhang, S. E, J. Zhang, Z. Li, et al., *Composites Part A: Applied Science and Manufacturing*. **2017**, *100*, 64–70. DOI: https://doi.org/10.1016/j.compositesa.2017.05.007.

[128] D. Lu, C. P. Wong, Q. K. Tong, in *Proceedings. 4th International Symposium on Advanced Packaging Materials Processes, Properties and Interfaces (Cat. No.98EX153)* **1998**.

[129] Ronald G. Larsen, in *The Structure and Rheology of Complex Fluids*, Oxford University Press New York **1999**.

[130] C. Yüce, ce, N. Willenbacher, *JoVE (Journal of Visualized Experiments)*. **2017**, (*122*), e55377. DOI: https://doi.org/10.3791/55377.

[131] D. Toker, D. Azulay, N. Shimoni, I. Balberg, O. Millo, *Phys. Rev. B*. **2003**, *68* (*4*), 041403. DOI: https://doi.org/10.1103/PhysRevB.68.041403.

[132] P. Zheng, H. Zhuo, Y. Zou, W. Guo, H. Wu, Z. Li, in *2018 IEEE 68th Electronic Components and Technology Conference (ECTC)* **2018**.

[133] T. Matsuda, T. Matsuda, M. Kambara, A. Hirose, *Materials & Design*. **2025**, *252*, 113780. DOI: https://doi.org/10.1016/j.matdes.2025.113780.

[134] B. V. L'vov, *Thermochimica Acta*. **1999**, *333* (*1*), 13–19. DOI: https://doi.org/10.1016/S0040-6031(99)00085-4.

[135] J.-J. Max, C. Chapados, *J. Phys. Chem. A*. **2004**, *108* (*16*), 3324–3337. DOI: https://doi.org/10.1021/jp036401t.

[136] Y. Bi, S. Ouyang, J. Cao, J. Ye, *Phys. Chem. Chem. Phys.* **2011**, *13* (*21*), 10071. DOI: https://doi.org/10.1039/c1cp20488b.

[137] Y. Li, K.-S. Moon, C. P. Wong, *IEEE Trans. Comp. Packag. Technol.* **2006**, *29* (*1*), 173–178. DOI: https://doi.org/10.1109/TCAPT.2006.870388.

[138] Jan Mewis, Norman J. Wagner, 1st ed., Cambridge University Press **2012**.

[139] Ronald G. Larsen, in *The Structure and Rheology of Complex Fluids*, Oxford University Press New York **1999**.

[140] C. Yang, Y.-T. Xie, M. M.-F. Yuen, B. Xu, B. Gao, X. Xiong, C. P. Wong, *Adv. Funct. Mater.* **2010**, *20* (*16*), 2580–2587. DOI: https://doi.org/10.1002/adfm.201000673.

[141] D. M. D. Abràmoff, *Biophotonics international*. **2004**, 36–42.

[142] M. Inoue, J. Liu, *Transactions of The Japan Institute of Electronics Packaging*. **2009**, *2* (*1*), 125–133. DOI: https://doi.org/10.5104/jiepeng.2.125.

[143] H. Liu, J. Liu, S. Wang, Z. Jin, S. Zhu, R. Ma, W. Zhang, J. Wang, J. Li, C. Song, et al., *Microelectronics Reliability*. **2022**, *135*, 114571. DOI: https://doi.org/10.1016/j.microrel.2022.114571.

[144] J. Xiong, J. Chen, P. S. Lee, *Adv Mater*. **2021**, *33* (*19*), 2002640. DOI: https://doi.org/10.1002/adma.202002640.

[145] S. Uzun, M. Han, C. J. Strobel, K. Hantanasirisakul, A. Goad, G. Dion, Y. Gogotsi, *Carbon*. **2021**, *174*, 382–389. DOI: https://doi.org/10.1016/j.carbon.2020.12.021.

[146] X. Shi, Y. Zuo, P. Zhai, J. Shen, Y. Yang, Z. Gao, M. Liao, J. Wu, J. Wang, X. Xu, et al., *Nature*. **2021**, *591* (*7849*), 240–245. DOI: https://doi.org/10.1038/s41586-021-03295-8.

[147] Y. Jang, S. M. Kim, G. M. Spinks, S. J. Kim, *Adv Mater*. **2020**, *32* (*5*), 1902670. DOI: https://doi.org/10.1002/adma.201902670.

[148] T. Agcayazi, K. Chatterjee, A. Bozkurt, T. K. Ghosh, *Adv Materials Technologies*. **2018**, *3* (*10*), 1700277.

[149] S. Shang, X. Yang, X. Tao, S. S. Lam, *Polymer International*. **2010**, *59* (*2*), 204–211. DOI: https://doi.org/10.1002/pi.2709.

[150] X. Pu, L. Li, H. Song, C. Du, Z. Zhao, C. Jiang, G. Cao, W. Hu, Z. L. Wang, *Adv Mater*. **2015**, *27* (*15*), 2472–8. DOI: https://doi.org/10.1002/adma.201500311.

[151] Y.-H. Chen, C.-C. Hsu, J.-L. He, *Surface and Coatings Technology*. **2013**, *232*, 868–875. DOI: https://doi.org/10.1016/j.surfcoat.2013.06.115.

[152] S. Zhu, M. Wang, Z. Qiang, J. Song, Y. Wang, Y. Fan, Z. You, Y. Liao, M. Zhu, C. Ye, *Chemical Engineering Journal*. **2021**, *406*, 127140. DOI: https://doi.org/10.1016/j.cej.2020.127140.

[153] B. Hwang, A. Lund, Y. Tian, S. Darabi, C. Müller, *ACS Appl Mater Interfaces*. **2020**, *12* (*24*), 27537–27544. DOI: https://doi.org/10.1021/acsami.0c04316.

[154] J. Hagedorn, F. S.-L. Blanc, J. Fleischer, *Handbuch der Wickeltechnik für hocheffiziente Spulen und Motoren: Ein Beitrag zur Energieeffizienz*, Springer-Verlag **2016**.

[155] Axalta, "What are wire enamels?," https://www.axalta.com/electricalinsulation_global/en_US/wire-enamels/what-are-wire-enamels.html (Accessed on July 3, 2024), **2024**.

[156] H. Zhang, X. Chen, Y. Liu, C. Yang, W. Liu, M. Qi, D. Zhang, *ACS Appl. Mater. Interfaces*. **2024**, *16* (*2*), 2554–2563. DOI: https://doi.org/10.1021/acsami.3c14036.

[157] C. Dong, Y. Bai, J. Zou, J. Cheng, Y. An, Z. Zhang, Z. Li, S. Lin, S. Zhao, N. Li, *Nondestructive Testing and Evaluation*. **2024**, 1–42. DOI: https://doi.org/10.1080/10589759.2024.2327639.

[158] M. Fischer, M. Woodhouse, P. Baliozian, J. Trube, **2023**, 27–30.

[159] S. Braun, G. Micard, G. Hahn, *Energy Procedia*. **2012**, *27*, 227–233. DOI: https://doi.org/10.1016/j.egypro.2012.07.056.

[160] M. T. Zarmai, N. N. Ekere, C. F. Oduoza, E. H. Amalu, *Applied Energy*. **2015**, *154*, 173–182. DOI: https://doi.org/10.1016/j.apenergy.2015.04.120.

[161] NormenBibliothek Online, "IEC 61215-2:2021, Terrestrische Photovoltaik(PV)-Module – Bauarteignung und Bauartzulassung," https://www.normenbibliothek.de/vde-xaveropp/normenbibliothek/start.xav#__normenbibliothek__%2F%2F*%5B%40attr_id%3D%270100671%27%5D__1709026542878 (Accessed on March 3, 2025), **2025**.

[162] *2004 Proceedings. 54th Electronic Components and Technology Conference (IEEE Cat. No.04CH37546)*, IEEE **2004**.

[163] K. Abdel Aal, N. Willenbacher, *Solar Energy Materials and Solar Cells*. **2020**, *217*, 110721. DOI: https://doi.org/10.1016/j.solmat.2020.110721.

Chapter 4: Verification of the contribution from the co-authors

Title: Iodine-Induced Microphase Separation Controls Flow Behavior and Electrical Conductivity of Silver-filled Polymer Composites

Journal: Applied Materials and Interfaces

Authors: Jonas Marten, Jennifer S. Urallar, Thao M. Duong, Patrick Théato, Norbert Willenbacher

Position in the dissertation:

The content of this paper has been included in Chapter 4

Contribution of Jonas Marten

- Designed and conducted the experiments
- Analyzed and interpreted the data
- Conceived and corrected the manuscript

Contribution of Jennifer S. Urallar

- Conducted the experiments
- Corrected the manuscript

Contribution of Thao M. Duong

- Conducted the experiments
- Corrected the manuscript

Contribution of Patrick Théato

- Provided infrastructure
- Corrected the manuscript

Contribution of Norbert Willenbacher

- Supervised the project
- Corrected the manuscript

Chapter 5: Verification of the contribution from the co-authors

Title: High-throughput Production of Electrically Conductive Yarn (E-Yarn) for Smart Textiles

Journal: Advanced Electronic Materials

Authors: Jonas Marten, Nathalie Gaukel, Yunkai Hu, Yiliang Wang, Guangjie Yuan, Norbert Willenbacher

Position in the dissertation:

The content of this paper has been included in Chapter 5

Contribution of Jonas Marten

- Designed and conducted the experiments
- Analyzed and interpreted the data
- Conceived and corrected the manuscript

Contribution of Nathalie Gaukel

- Conducted the experiments
- Corrected the manuscript

Contribution of Yunkai Hu

- Conducted the pressure sensor experiments
- Corrected the manuscript

Contribution of Yiliang Wang

- Corrected the manuscript

Contribution of Guangjie Yuan

- Provided infrastructure
- Analyzed and interpreted the data of the pressure sensor experiments
- Corrected the manuscript

Contribution of Norbert Willenbacher

- Supervised the project
- Corrected the manuscript

Chapter 6: Verification of the contribution from the co-authors

Title: Highly Conductive Coated Wires for Interconnection of Solar Cells with TECC-Wire Technology

Journal: Solar Energy Materials and Solar Cells

Authors: Jonas Marten, Mona Schnaiter, Yonas Zemen, Lars Podlowski, Stefan Ricken, Norbert Willenbacher

Position in the dissertation:

The content of this paper has been included in Chapter 6

Contribution of Jonas Marten

- Designed and conducted the experiments
- Analyzed and interpreted the data
- Conceived and corrected the manuscript

Contribution of Mona Schnaiter

- Conducted the experiments

Contribution of Yonas Zemen

- Conducted the experiments
- Corrected the manuscript

Contribution of Lars Podlowski

- Corrected the manuscript

Contribution of Stefan Ricken

- Corrected the manuscript
- Provided infrastructure and samples

Contribution of Norbert Willenbacher

- Supervised the project
- Corrected the manuscript